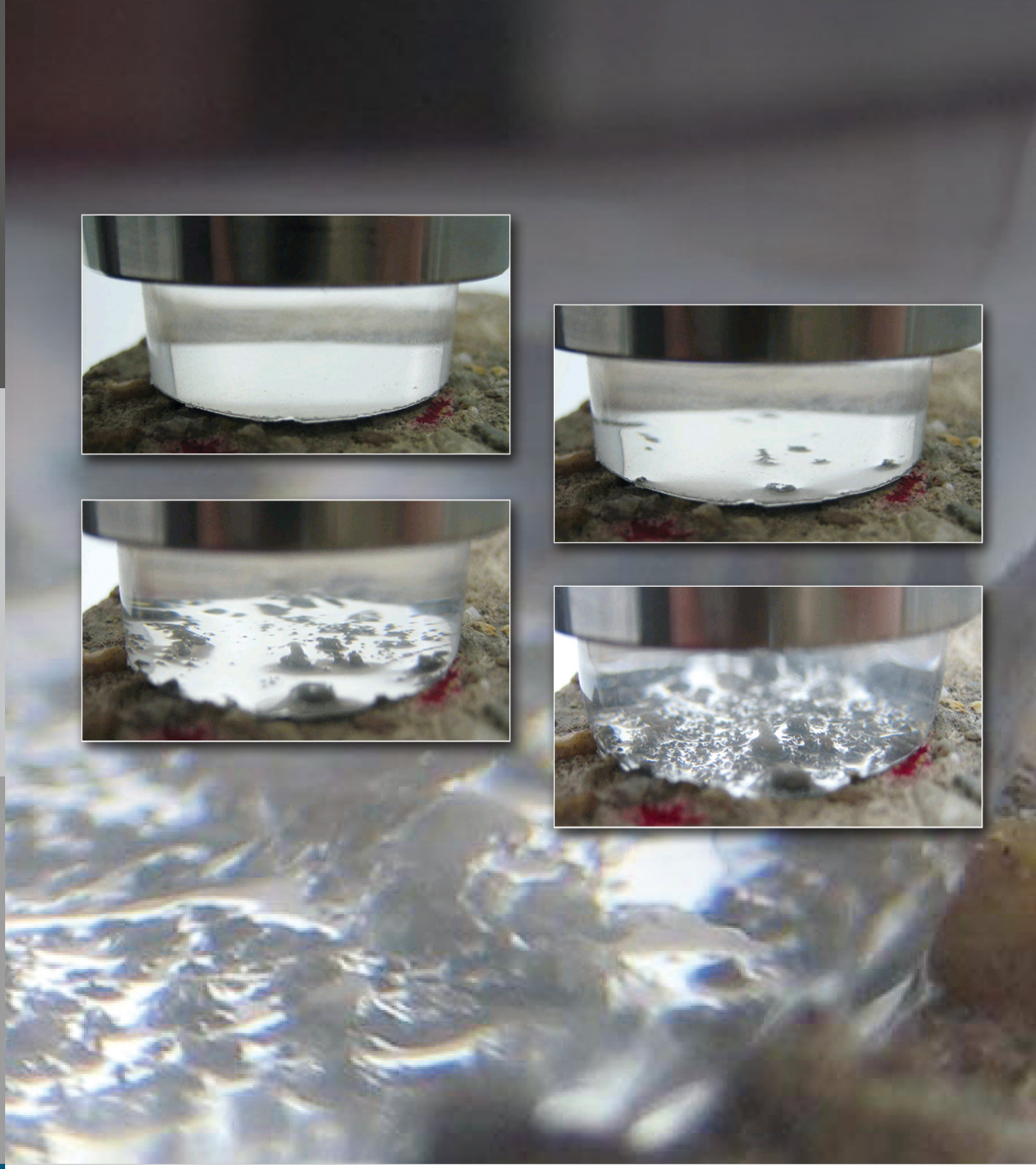

Contact Mechanics and Friction of Elastic Solids on Hard and Rough Substrates

Boris Lorenz

Mitglied der Helmholtz-Gemeinschaft

JÜLICH
FORSCHUNGSZENTRUM

Schriften des Forschungszentrums Jülich
Reihe Schlüsseltechnologien / Key Technologies Band / Volume 37

Forschungszentrum Jülich GmbH
Peter Grünberg Institute (PGI)
Quantum Theory of Materials (PGI-1/IAS-1)

Contact Mechanics and Friction of Elastic Solids on Hard and Rough Substrates

Boris Lorenz

Schriften des Forschungszentrums Jülich
Reihe Schlüsseltechnologien / Key Technologies Band / Volume 37

ISSN 1866-1807 ISBN 978-3-89336-779-5

Bibliographic information published by the Deutsche Nationalbibliothek.
The Deutsche Nationalbibliothek lists this publication in the Deutsche Nationalbibliografie; detailed bibliographic data are available in the Internet at http://dnb.d-nb.de.

Publisher and Distributor:	Forschungszentrum Jülich GmbH Zentralbibliothek 52425 Jülich Phone +49 (0) 24 61 61-53 68 · Fax +49 (0) 24 61 61-61 03 e-mail: zb-publikation@fz-juelich.de Internet: http://www.fz-juelich.de/zb
Cover Design:	Grafische Medien, Forschungszentrum Jülich GmbH
Printer:	Grafische Medien, Forschungszentrum Jülich GmbH
Copyright:	Forschungszentrum Jülich 2012

Schriften des Forschungszentrums Jülich
Reihe Schlüsseltechnologien / Key Technologies Band / Volume 37

D 82 (Diss., RWTH Aachen University, 2012)

ISSN 1866-1807
ISBN 978-3-89336-779-5

The complete volume is freely available on the Internet on the Jülicher Open Access Server (JUWEL) at http://www.fz-juelich.de/zb/juwel

Content

Nomenclature

A	Area of real contact
A_0	Nominal contact area
A_H	Hertzian contact area
$A(\zeta)$	Apparent contact area at magnification ζ
$C(\mathbf{q})$	Surface roughness power spectrum
$C_\mathrm{B}(\mathbf{q})$	Bottom surface roughness power spectrum
$C_\mathrm{T}(\mathbf{q})$	Top surface roughness power spectrum
C_V	Heat capacity
D_f	Fractal dimension
d_T	Thermal length
E	Young's modulus
E'	Effective Young's modulus
$E(\omega)$	Complex elastic modulus
E_el	Elastic energy
F_f	Friction force
F_H	Hertzian load
F_N	Normal force
H	Hurst exponent
h_rms	Root-mean-square roughness
$h(\mathbf{x})$	Surface height profile
$\mathbf{J}$	Fluid flow vector
J_0	Heat current
L	Linear system size
m_n	Moment of the surface roughness power spectrum
m_0	Zero moment of the surface roughness power spectrum
m_2	Second moment of the surface roughness power spectrum
m_4	Fourth moment of the surface roughness power spectrum
N	Number of contacting asperities per unit area
n_0	Number of asperities per unit area
p	Squeezing pressure
P_0	Normal squeezing pressure
P_a	High hydrostatic pressure
P_b	Low hydrostatic pressure
p_c	Percolation treshold
p_cont	Average contact pressure
p_fluid	Average fluid pressure

P_h	Surface height probability distribution
$P(h, r_1, r_2)$	Joint probability distribution
$P(\sigma, \zeta)$	Stress distribution in the contact at magnification ζ
q	Surface roughness wavevector
q_{L}	Smallest possible wavevector
q_0	Long distance roll-off wavevector
q_1	Short distance cut-off wavevector
$\dot{Q}$	Fluid volume flow rate
R_0	Radius of the Hertz contact region
R_{a}	Arithmetic roughness average
R_{q}	Root-mean-square (RMS) roughness
R_{z}	Average maximum height of the profile
S	Shape factor
T	Temperature
u	Interfacial separation
$\bar{u}$	Mean interfacial separation
u_{c}	Critical interfacial separation
z	Surface height
α	Critical pore shape factor
ΔP	Hydrostatic pressure difference
δ	Phase difference
ϵ	Stress
ζ	Magnification
ζ_{crit}	Critical magnification
η	Fluid viscosity
κ	Thermal conductivity
λ	Lateral resolution
μ	Coefficient of friction
ν	Poisson's ratio
ρ	Mass density
σ	Applied squeezing pressure or stress
σ_{f}	Frictional shear stress
$\sigma(r)$	Hertz pressure distribution
$\phi_{\mathrm{p}}(\bar{u})$	Fluid pressure flow factor
ω	Perturbing or excitation frequency

1 Introduction

Contact mechanics and **friction** are topics of huge importance with many applications in Nature and technology. They are closely interconnected, so that understanding friction requires a deep insight into the contact formation between two solids. During university studies, students learn very early that the sliding friction force F_{f} is proportional to the normal force F_{N} and independent of the relative sliding velocity, $F_{\mathrm{f}} = \mu F_{\mathrm{N}}$. The constant of proportionality μ, the coefficient of friction, depends on several parameters, such as the material combination, temperature and surface roughness. Thus one may think that friction is a simple and well understood subject. It is, in fact, one of the oldest topics in physics, and a vast amount of work has been invested in order to gain insight into contact mechanics and friction. Despite all the theoretical and experimental effort, neither topic is well understood.

The importance of contact mechanics and friction cannot be overestimated, as they affect our every day life in countless situations. The reader of this manuscript, for example, would be unable to turn to the next page or walk to the coffee machine in the absence of friction. The complex nature of friction results from its extreme surface sensitivity; a single monolayer of interface atoms or molecules can change the friction by an order of magnitude (or more). In addition, friction usually depends on many decades in length scales, which can be illustrated by two examples. On the nanometer scale, the coefficient of friction between two clean diamond surfaces in ultrahigh vacuum is typically of order 1 or more, because of the strong interaction between the surface dangling bonds. If these bonds are saturated with a hydrogen monolayer, the coefficient of friction decreases rapidly to ≈ 0.05. This shows that even a nanometer thick boundary layer can influence the friction greatly. On the other hand, energy losses due to tidal forces cause the rotation of the earth to slow by the order of $1.6 \cdot 10^{-7}$ seconds per year. This is the reason why during the Cambrian age, approximately 500 Million years ago, the day had only about 21 hours. How to account for all the relevant length scales remains an important and open problem in physics.

Surface interactions are not only of crucial importance in Nature, they also dictate and control the functions of practically every device developed by man to enhance the quality of life. The study of "the science and technology of interacting surfaces in relative motion and the practices related thereto" [44] is called tribology, based upon the Greek word tribo ($T\rho\iota\beta\omega$) meaning "I rub". An early example of the evolution of our knowledge about friction is shown in a painting found in a grotto at El-Bershed (Egypt) dated about 1880 B.C. (see Fig. 1.1) where a large stone statue is moved on a sledge towed by numerous workers/slaves. In order to lower the friction forces at the contacting interface, an officer standing at the front of the pedestal pours a

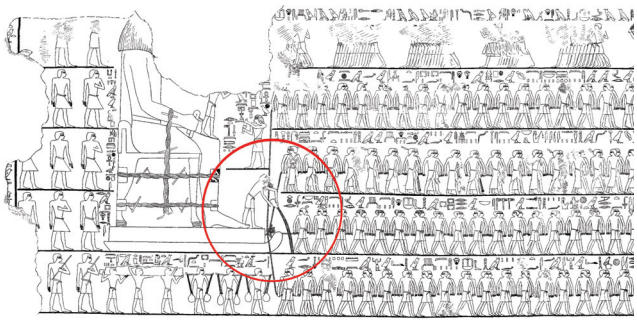

Abbildung 1.1: A painting found at El-Bershed, dated about 1880 B.C., showing an officer pouring a lubricant in front of a statue in order to reduce the sliding friction.

lubricant onto the ground directly in front of the sledge. However, sometimes it is necessary to maximize friction rather than minimize it. For example, around 200.000 B.C., the Neanderthal people used high friction to generate fire by rubbing wood on wood, and by striking flint stones together.

As a modern scientific discipline, tribology itself is a relative young and interdisciplinary subject involving *lubrication*, *friction* and *wear*, and its role has become increasingly important as many technological devices undergo miniaturization of their moving parts. [6, 9, 41]. It has been estimated that the energy losses and wear in technical systems resulting from failure to reduce friction amount to $4 - 6\%$ of the gross national product in industrialized countries. This amounts to billions of Euros every year, a huge economical loss. Improving the efficiency is not just an economical issue, it can contribute in an important way to the fight against global warming and the resulting climate change. In spite of its importance, many aspects of contact mechanics and friction are still not well understood, and an understanding of friction on an atomic level is just starting to emerge.

Recently Persson developed a novel theory to describe the contact formation between two solids and to calculate the friction between these two bodies if one compromises a rubber-like material. This theory has been developed in the context of a tyre running on a road surface (rubber friction) and is based on a novel theory for contact mechanics. Much effort has been devoted to test this approach by comparisons to numerical (e.g. molecular dynamics) simulations, but there has been no comprehensive experimental test of this theory. This has motivated the work presented in this thesis, where a set of experiments has been performed to test the theory. The work presented in the following chapters addresses the validation, improvement and extension of the approach.

The work is structured in the following way. In Sec. 2, different approaches towards contact mechanics for elastic solids with randomly rough surfaces are reviewed briefly

to introduce the framework of this thesis, and experiments are described in Sections 3 – 6 to test the predictions of the theory of Persson and to compare with predictions of the state-of-the-art theories of contact mechanics. The approach is then tested in more detail by studying applications of the theory to the technical problems described below, of which are of great engineering interest. In Sec. 7 the approach of Persson to calculate the friction of an elastic solid in relative motion on a rough substrate is studied.

Interfacial separation is the distance between solids in contact in the non-contact areas. It is important, for example, in leakage of seals, heat transfer and tyre noise. Here the mean interfacial separation between two solids with randomly rough surfaces is studied, as well as its dependance on the squeezing pressure applied.

Leak rate of seals is a topic of economic and ecological interest. By understanding the contact mechanics, it is possible to model the flow of a fluid from the high pressure side to the low pressure side in a static seal. Applying the contact mechanics theory of Persson and percolation theory, one can calculate the leakage resulting from fluid flow in percolating non-contact channels. This approach is described and tested using model experiments.

Squeezing out of fluids between two solids that have rough surfaces and are in contact. Bringing two solids together in the presence of a fluid results in fluid squeeze-out during contact formation. This is relevant, for example, for tyres on a wet road or for dynamic rubber seals. Adopting the leak rate theory it is possible to calculate the time-dependent squeeze out, which is compared with experimental data obtained using a simple device.

Heat transfer between rough surfaces is another application of the theory of contact mechanics. The origin of the heat transfer via the real area of contact, and via the non-contact regions for two solids with rough surfaces in contact will be explained. A simple experiment to test the accuracy of this theory is presented.

Rubber friction A theory of Persson on rubber friction, based on the contact mechanics theory, is described briefly, and its predictions are compared with the results of carefully performed model experiments.

The thesis is concluded with a short summary of the work and the results obtained.

2 Contact Mechanics

The nature of the contact formation between two solids is still not well understood due to the fact that most real surfaces exhibit surface roughness on many decades in length scales. This section deals with the history and the progress of contact mechanics. A simple way of how to describe surface roughness is introduced. Different approaches to contact mechanics are described, namely the traditional and state-of-the-art multiasperity contact theories as well as a novel approach by Persson. The most advanced classical theory by Bush, Gibson and Thomas, as well as the theory of Persson, are briefly reviewed.

Contact mechanics is the study of the deformation of two solids that come into contact. It is fundamental to the field of mechanical engineering by providing information necessary for the safe and energy efficient design of technical systems. Much research has been carried out in the last decades to find accurate contact mechanics models but a full comprehension of the nature of the contact between two solids with randomly rough surfaces has not yet been achieved. The reason for this is that surfaces of solids usually exhibit surface roughness over many decades in length scales. In general, when two elastic solids with surface roughness are squeezed together, they do not make contact everywhere in the apparent contact area, but only at a distribution of asperity contact spots, real atomic contact exists. The three most important physical quantities in contact mechanics are the **area of real contact**, the **interfacial separation** in the non-contact regions, and the **stress distribution** in the contact regions [42, 43, 72, 85, 93].

Contact mechanics has a long history. The first analytical study was presented by Hertz in 1882 where the frictionless contact between elastic solids with smooth surface profiles was studied [38]. Hertz assumed that close to the contact area, these (undeformed) solids have parabolic shape. For this model, the theory predicts a nonlinear increase of the contact area A with the squeezing force F_{N}, namely $A \sim F_{\mathrm{N}}^{2/3}$.

The simplest model of a rough surface consists of a regular array of spherical bumps with equal radius of curvature R and equal height h as illustrated in Fig. 2.1 (a). If such a surface is squeezed against an elastic solid with a flat surface, the Hertz contact theory can approximately be applied to each asperity. This is the simplest *multiasperity contact model* where the surface roughness is modelled as bumps. Applying the Hertz contact theory to each contact spot, this simple approach results in an increase of the real area of contact with the normal load as $\propto F_{\mathrm{N}}^{2/3}$. However, this is not in accordance with experiments, which show indirectly that the real area of contact is proportional to F_{N} as long as the contact area A is small

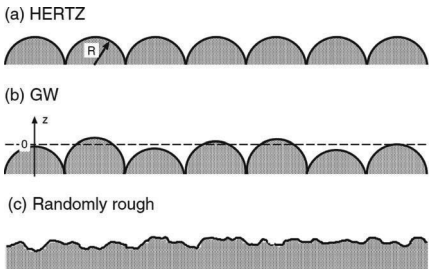

Abbildung 2.1: Three different models of a "rough" surface. In case (a) all the asperities are equally high and have identical radius of curvature. Introducing asperities with a random height distribution as in (b) gives the Greenwood-Williamson approach on contact mechanics. In (c) a real, randomly rough surface is shown where the asperities are of different heights and curvature radii.

compared with the nominal contact area A_0.

In a pioneering study, Archard developed a more realistic hierarchical model, where surface roughness is described as small spherical bumps on top of larger spherical bumps and so on [1]. It can be shown that this idea leads to an area of real contact which is proportional to the applied load. A more useful model, from the point of view of application, was presented by Greenwood and Williamson (GW) [31, 32]. They modeled the roughness as an ensemble of identical spherical asperities with equal radius R and with randomly distributed heights to take account of the surface statistics, see Fig. 2.1 (b).

The most advanced multiasperity contact theory has been presented by Bush, Gibson and Thomas (BGT) [12] in 1975. Following Longuet-Higgins [49] and Nayak's [66] statistical theory of isotropic randomly rough surfaces, they modeled the asperities as paraboloids with two different radii of curvature. While the GW theory assumes roughness on a single length scale, resulting in a slightly non-linear dependance of the real area of contact on the load, the BGT theory takes into account roughness on different length scales. This leads to a linear relation between the real area of contact A with the load as long as A is much smaller then the nominal contact area A_0. Thus, BGT were able to show that A is strictly proportional to the load only when roughness occurs on different length scales. However this linear relation between squeezing pressure and real area of contact holds true only for very low pressures. Multiasperity theories are in general believed to give correct results only for very small loads and contact areas. This is due to two simplifications done: The first and most severe approximation is that long-range elastic deformation is neglected. However, if an asperity is pushed downwards, it will effect the contact between other asperities, as shown schematically in Fig. 2.2. Accounting for the deformation of the big asperity, the contact in (b) is bigger than in (a) where the

(a) (b)

Abbildung 2.2: It is shown how long-range elastic deformation influences the contact formation. In (a) the deformation of the large asperity is neglected leading to a smaller area of contact as in (b) where the influence of the deformation field on the other asperities is considered properly.

long-range elastic deformation is neglected. The second problem is the rather idealized roughness model, where roughness is described by asperities or bumps with identical radius of curvatures. The hierarchical, fractal-like nature of real surfaces, as shown in Fig. 2.1 (c) and 2.3, is not considered properly.

Recently a novel and fundamentally different approach towards contact mechanics has been presented by Persson [74, 75]. In contrast to the multiasperity contact theories, where the area of real contact has to be much smaller than the nominal contact area, this approach starts from the opposite limit of very large contact. Here the squeezing force is so high that nearly complete contact occurs, and in this limit the theory predictions are exact. For small forces the projected (on the xy-plane) contact area A is proportional to the load F_{N}, while A approaches A_0 in a continuous manner as F_{N} increases towards infinity. In this theory a diffusion-like equation is used to calculate the stress distribution at the interface. This equation is derived by studying the interface at different magnification ζ. First the surface is considered to be smooth with no noticeable roughness. Looking at the interface with low magnification (or low resolution), no surface height variations can be observed. The surface appears perfectly smooth. The magnification is then successively increased so that more and more (or shorter and shorter) roughness components are considered. Including all length scales gives the full stress distribution observed at the highest magnification. The area of real contact can then be deduced from the stress distribution.

The experts are still arguing about which approach gives better results [8, 14, 15, 21, 40, 58, 114]. It can be shown that, for the reasons already mentioned above, the multiasperity contact theories only hold when the contact area is very small and when roughness occurs on a single (or a narrow range of) length scale. Therefore they are not of particular interest for most engineering applications. However a rigorous and comprehensive experimental test of the theory of Persson has not been performed yet. In the first part of this section on contact mechanics, surface roughness is introduced and a convenient manner of how to describe it is presented. Then the two different approaches towards contact mechanics, with BGT as the most advanced multiasperity contact theory, are briefly described.

2.1 Surface Roughness

Surface roughness is specified as and quantified by the vertical deviations $z = h(x, y)$ of a real surface from its ideal form. The larger these deviations are, the rougher the surface is considered to be. If the deviations are small, the surface is classified to be smooth. Roughness is usually characterized using simple parameters, e.g. the arithmetic average R_a, the root-mean-squared R_q or the average surface roughness R_z. However, most surfaces tend to be nearly self-affine fractal, and since these parameters are dominated by surface roughness observable at rather low magnification, the roughness can not be properly described by these parameters alone. A self-affine fractal surface has the property that if a part of the surface is magnified, with different magnifications in the perpendicular direction to the surface as compared with the parallel (in plane) direction, it "looks the same" and also the statistical properties are invariant under this scale transformation (see Fig. 2.3).

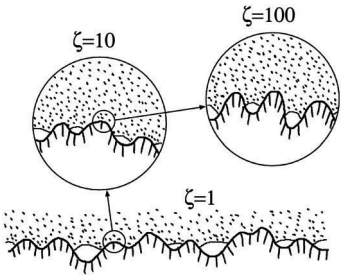

Abbildung 2.3: Magnifying a contact region with the magnification ζ one observes smaller length scale roughness and the surface "looks the same" as before [85].

The best method to describe surface roughness on many different length scales without loosing important information is the surface roughness power spectrum (or power spectral density) $C(\mathbf{q})$ [20, 75]. For a randomly rough surface, that is when $h(\mathbf{x})$ is a Gaussian random variable, the statistical properties of the surface are completely described by the power spectrum. $C(\mathbf{q})$ is the Fourier transform of the height-height correlation function, but it can also be defined through the square modulus of the Fourier transform of $h(\mathbf{x})$. This is indeed the conventional approach adopted from the context of signal theory. Here, the power spectrum describes how the power of a signal or time series is distributed with frequency, i.e. it describes how the signal varies with frequency rather than with time. The power can be the actual physical power but more often it is the squared value of the signal. For the case of the surface roughness power spectrum, the topography information $z = h(x, y)$ is transformed using Fourier transformation from real space $\mathbf{x} = (x, y)$ to frequency or wavevector space $\mathbf{q} = (q_x, q_y)$, (where $q = 2\pi/\lambda$ is the roughness wavelength), whereas the power represents the squared value of the roughness amplitude.

$$C(\mathbf{q}) = \frac{1}{(2\pi)^2} \int \mathrm{d}^2x \ \langle h(\mathbf{x})h(\mathbf{0})\rangle \mathrm{e}^{-i\mathbf{q}\cdot\mathbf{x}} \tag{2.1}$$

Here $z = h(\mathbf{x})$ is the height of the surface at the point $\mathbf{x} = (x, y)$ above a flat reference plane chosen so that $\langle h(\mathbf{x})\rangle = 0$. The angular bracket $\langle ...\rangle$ stands for ensemble averaging. The roughness parameters presented before, e.g. R_q, are usually dominated by the longest wavelength surface roughness components, while higher order moments of the power spectrum such as the average slope or the average surface curvature are dominated by the shorter wavelength components. However these parameters contain no information about the hierarchic structure of the surface. Many surfaces of technological interest are to a good approximation self-affine fractal so that the power spectrum of these surfaces can be written as

$$C(q) \propto \left(\frac{q_0}{q}\right)^{2(H+1)} \tag{2.2}$$

where H is the so called Hurst exponent which can be related to the fractal dimension using $D_\mathrm{f} = 3 - H$. Real surfaces are not self-affine fractal over all length scales. The largest possible wavevector is $q_1 \approx 2\pi/a$ where a is the smallest relevant length scale, e.g. an atomic distance, whereas the smallest possible wavevector $q_L \approx 2\pi/L$ is defined by the linear size L of the system considered. Surfaces of importance in technology are typically, to a good approximation, self-affine fractal in some finite wavevector regime, say for $q_0 < q < q_1$, as it is shown schematically in Fig. 2.4. The fractal dimension of surfaces prepared by sandblasting, grinding or laying of a road surface are typically $D_\mathrm{f} \approx 2.2$ to 2.5.

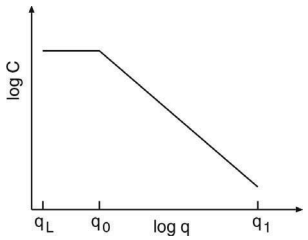

Abbildung 2.4: The surface roughness power spectrum of a surface which is self-affine fractal for $q_0 < q < q_1$. The long distance roll-off wavevector q_0 and the short distance cut-off wavevector q_1 depend on the system under consideration. The slope of the $\log C - \log q$ plot for $q > q_0$ determines the fractal dimension of the surface. The lateral size L of the available surface region determines the smallest wavevector $q_L = 2\pi/L$.

Measuring surface roughness is often performed nowadays, and depending on the wavelength range different methods can be used, e.g. stylus (or linescan) methods,

optical methods, atomic force microscopy or scanning tunneling microscopy. The full power spectrum is obtained by superposition of the information obtained at different lengthscales to a full surface roughness power spectrum as shown in Fig. 2.5. The different partial power spectra join smoothly at the overlapping wavelength intervals.

It is easy to calculate the fractal dimension since the slope of the relation between log C and log q for the region $q_0 < q < q_1$ is defined as [slope $= 2(4 - D_\mathrm{f})$]. The fractal dimension of the surface in Fig. 2.5 is $D_\mathrm{f} \approx 2.3$.

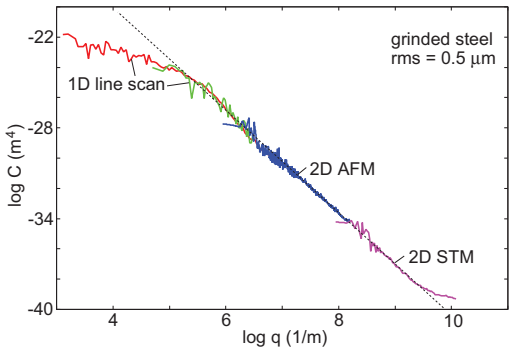

Abbildung 2.5: The surface roughness power spectrum of a ground steel surface obtained by combining different measuring techniques (stylus instruments, atomic force microscope and scanning tunneling microscope).

2.2 Multiasperity Contact Theories

2.2.1 Hertz Contact Theory

All multiasperity contact theories approximate the surface asperities as spherical or elliptical "bumps" to which they apply the Hertz contact theory [38]. It is therefore necessary to describe this approach briefly. The Hertz theory considers the contact between two spherical, elastic bodies (radius R_1 and R_2) with perfectly smooth surfaces. These spheres are squeezed into contact with the external force F. The deformation field in the two bodies can be calculated by minimizing the elastic deformation energy. The radius r_0 of the circular contact region is given by

$$r_0 = \left(\frac{R_1 R_2}{R_1 + R_2}\right)^{1/3} \left(\frac{3F(1-\nu^2)}{4E}\right)^{1/3} \tag{2.3}$$

with

$$\frac{1-\nu^2}{E} = \frac{1-\nu_1^2}{E_1} + \frac{1-\nu_2^2}{E_2} \tag{2.4}$$

Here E_1 and E_2 are the elastic moduli while ν_1 and ν_2 are the corresponding Poisson ratios of the two solids [43]. The penetration s, or the distance the two solids approach each other, is given by

$$s = \left(\frac{R_1 + R_2}{R_1 R_2}\right)^{1/3} \left(\frac{3F(1-\nu^2)}{4E}\right)^{2/3} \tag{2.5}$$

For the case of a sphere with radius R in contact with a flat surface one can deduce from Eq. (2.3) and (2.5) the area of contact:

$$A = \pi r_0^2 = \pi R s \tag{2.6}$$

The squeezing force can be calculated using

$$F = \frac{4E}{3(1-\nu^2)} s^{3/2} R^{1/2} \tag{2.7}$$

The pressure distribution $\sigma(r)$ in the contact depends on the distance r from the center of the circular contact area:

$$\sigma(r) = \frac{F}{\pi r_0^2}\left[1 - \left(\frac{r}{r_0}\right)^2\right] \tag{2.8}$$

The Hertz contact theory can also be generalized to include adhesion between the two solid bodies. This has been done by Johnson, Kendall and Roberts in 1971 [43].

2.2.2 Greenwood and Williamson Theory

Within the framework of multiasperity contact models, the area of contact and the load, as a function of the distance between the two approaching bodies, depends on the joint height probability distribution $P(h)$. Greenwood and Williamson assumed roughness to occur on a single length scale and they simplified the asperities as spherical bumps with equal radius of curvature R (see Fig. 2.1 (b)). The height of the asperities varies and it is described using a Gaussian height distribution:

$$P_h = \frac{1}{(2\pi)^{(1/2)} h^*} \exp\left(-\frac{h^2}{2h^{*2}}\right) \tag{2.9}$$

where h^* is the root-mean-square amplitude of the summit height fluctuation. GW assumed frictionless contact between the elastic solids. In this case the contact stresses depend only upon the shape of the (undeformed) gap between the two solids before loading. Thus, without loss of generality, the system with $z = h_1(\mathbf{x})$ and $z = h_2(\mathbf{x})$ describing the surface height profiles, E_1 and E_2 the Young's elastic moduli of the two solids, and ν_1 and ν_2 the corresponding Poisson's ratios, can be replaced by the contact between a rigid solid with the roughness profile $h(\mathbf{x}) = h_1(\mathbf{x}) + h_2(\mathbf{x})$ in contact with an elastic solid with a flat surface and with the Young's modulus E and Poisson ratio ν chosen so that Eq. (2.4) is obeyed. GW neglected the elastic interactions between the asperity contact regions. If the separation between the

(average plane of) two surfaces is denoted by d, an asperity with height $h > d$ will make contact with the plane, and the penetration s is the difference of h and d. Using the Hertz contact theory with $s = h - d$, the normalized area of real contact is [32]

$$\frac{\Delta A}{A_0} = \pi n_0 R \int_d^\infty \mathrm{d}h \ (h-d) P_h \tag{2.10}$$

Here A_0 denotes the nominal contact area whereas n_0 is the number of asperities per unit area. The number N of contacting asperities per unit area is calculated using

$$\frac{N}{A_0} = n_0 \int_d^\infty \mathrm{d}h \ P_h \tag{2.11}$$

whereas the nominal squeezing stress can be calculated using

$$\sigma_0 = \frac{F_\mathrm{N}}{A_0} = \frac{4E}{3(1-\nu^2)} n_0 \int_d^\infty \mathrm{d}h \ (h-d)^{3/2} R^{1/2} P_h \tag{2.12}$$

It is also possible to account for adhesive contact between randomly rough surfaces using the Greenwood and Williamson theory. However, as this is only a brief introduction the reader is referred to [23] and [32] for a precise illustration of this issue.

2.2.3 Bush, Gibson and Thomas Model

Bush, Gibson and Thomas modeled the asperities as paraboloids with two different radii of curvature. The asperities are summits with heights h, and curvatures r_1 and r_2. Observe that when r_1 is defined to be the maximum curvature and r_2 the minimum curvature of the summit, the following inequality holds $r_1 > r_2 > 0$. Note that $r_1 > r_2$ is necessary because two different summits with different orientation, but with the same maximum curvature r_1 and minimum curvature r_2, are equivalent. BGT, like GW, also neglected the elastic coupling between the asperities, but they included roughness occurring on different length scales. Recalling the Longuet-Higgins [49] and Nayak [66] analysis of surface statistics, it is possible to show that for an isotropic surface the joint probability distribution $P(h, r_1, r_2)$ is given by [16, 17]

$$P(h, r_1, r_2) = \frac{\sqrt{27}}{(4\pi)^2 m_2 m_4 \sqrt{m_0 m_4}} \times C_1^{1/2} \exp\left[-C_1 \left(\frac{h}{m_0^{1/2}} + \frac{3(r_1+r_2)}{4\sqrt{\alpha m_4}} \right)^2 \right] (r_1 - r_2)$$

$$\times r_1 r_2 \exp\left[-\frac{3}{16 m_4} [3(r_1+r_2)^2 - 8 r_1 r_2] \right] \tag{2.13}$$

where the quantities m_0, m_2, and m_4 are the zero, second and fourth moments of the surface roughness power spectrum. In Eq. (2.13) the breadth parameter (as

defined by Nayak) is $\alpha = m_0 m_4 / m_2^2$ and $C_1 = \alpha/(2\alpha - 3)$. Observe that for an isotropic surface the power spectrum $C(\mathbf{q})$ depends only on the modulus $q = |\mathbf{q}|$ of the wave-vector, therefore one can also calculate the moments m_n as

$$m_n = \int_0^{2\pi} \mathrm{d}\phi \, (\cos\phi)^n \int_0^{\infty} \mathrm{d}q \; q^{1+n} C(q) \tag{2.14}$$

In order to determine the area of contact and the load between the rough rigid surface and an initially flat elastic half-space, BGT also makes use of the Hertz's theory to calculate, for a given penetration $s = h - u$, the contact area and load upon contact between the elastic half-space and each single rigid asperity. Hertz's theory states that, beside the elastic properties of the contacting bodies, the contact area and the load depend only on the penetration s and the principal radii of curvature of the contacting asperities. Thus, one can calculate the fraction of area in contact A_c/A_0 and the mean pressure in the nominal contact area $\sigma = F/A_0$ as

$$\frac{A_\mathrm{c}}{A_0} = \int_u^{+\infty} \mathrm{d}h \iint_{\mathcal{D}} \mathrm{d}r_1 \; \mathrm{d}r_2 \; A_\mathrm{H}(h, r_1, r_2) P(h, r_1, r_2) \tag{2.15}$$

$$\frac{F}{A_0} = \int_u^{+\infty} \mathrm{d}h \iint_{\mathcal{D}} \mathrm{d}h \; \mathrm{d}r_2 \; F_\mathrm{H}(h, r_1, r_2) P(h, r_1, r_2) \tag{2.16}$$

where the domain $\mathcal{D} = \{(r_1, r_2) \in \Re^2 \mid r_1 \geq r_2 \geq 0 \,|\}$, $A_\mathrm{H}(h, r_1, r_2)$ and $F_\mathrm{H}(h, r_1, r_2)$ are Hertzian contact area and load on each asperity in contact.

Bush, Gibson and Thomas developed in 1975 [12] the most complete theory of contact mechanics within the framework of multiasperity contact models. They made use of Eq. (2.15) and (2.16) but in a different form. Instead of focusing on the radii of curvature of the asperities, r_1 and r_2, (which, following the Hertz theory, were treated as paraboloidal asperities), they developed calculations by referring to the semi-axes of the ellipse of contact, a_1 and a_2. We refer the reader to the original paper by Bush Gibson and Thomas [12] and to Ref. [17] for a detailed description of the model.

The major result of the BGT theory is that in the limiting case of large separations, the area of true contact A_c is proportional to the applied load F, and equal to just half of the bearing area. However because of the rather simple model of surface roughness and the neglect of long-range elastic coupling, multiasperity theories are expected to be correct only for very small applied squeezing pressures and therefore small areas of real contact [79, 87].

2.3 Contact Mechanics Theory of Persson

The theory approach to contact mechanics of Persson removes the assumption, which is implicit in all the multiasperity contact theories, that the area of real contact is small compared with the nominal contact area. On the contrary, this approach moves from the limiting case of full contact conditions (where the theory gives the exact solution) between a rigid rough surface and an initially flat elastic half-space, and accounts for partial contact by requiring that, in case of adhesionless contact, the stress probability distribution vanishes when the local normal surface stress σ vanishes. The basic idea is to not exclude a priori any roughness length scale from the analysis. If $A(\zeta)$ is the apparent area of contact at the length scale $\lambda = L/\zeta$, then the function $P(\zeta) = A(\zeta)/A_0$ is studied. The theory needs as input the surface roughness power spectrum $C(q)$ and the elastic properties E and ν of the two contacting bodies. $P(\sigma, \zeta)$ is the stress distribution in the contact areas under the magnification ζ. It satisfies the differential equation (see [73, 74])

$$\frac{\partial P}{\partial \zeta} = f(\zeta)\frac{\partial^2 P}{\partial \sigma^2} \tag{2.17}$$

where $f(\zeta) = G'(\zeta)\sigma_0^2$ and $\sigma_0 = F_{\mathrm{N}}/A_0$ being the average or nominal pressure in the nominal contact area. Where the function

$$G(\zeta) = \frac{\pi}{4}\left(\frac{E^*}{\sigma_0}\right)^2 \int_{q_L}^{\zeta q_L} \mathrm{d}q\; q^3 C(q) \tag{2.18}$$

with $E^* = E/(1-\nu^2)$. Eq. (2.17) is a diffusion-like equation where time is replaced by magnification ζ, the spatial coordinate with the stress σ and where the "diffusion constant" $f(\zeta)$ depends on ζ. The physical meaning of Eq. (2.17) is the following. Studying a system at the lowest magnification $\zeta = 1$ no surface roughness can be observed and the block makes (apparent) contact with the substrate everywhere in the nominal contact area, see Fig. 2.7 (a) left. For this case, if friction at the interface can be neglected, the stress at the interface equals everywhere the applied stress σ_0, and the stress distribution (Fig. 2.7 (a) right) is a delta function $P(\sigma, 1) = \delta(\sigma - \sigma_0)$. Increasing the magnification, surface roughness with wavelength down to $\lambda = L/\zeta$ is introduced to the system leading to emerging non-contact regions. Since the stress must continuously go to zero at the edges of the boundary between the contact and the non-contact regions (like in the Hertz theory), it follows that the stress distribution $P(\sigma, \zeta)$ exhibits a tail extending the whole way down to zero stress as indicated in Fig. 2.7 (b). There will also be a tail towards larger stresses $\sigma > \sigma_0$ because the average stress must be equal to σ_0. With increasing magnification this distribution broadens more and more like in a diffusion problem, as indicated in (c).

The expression for the stress distribution $P(\sigma, \zeta)$ at the interface when the contact is studied at the magnification $\zeta = L/\lambda$, where λ is the shortest surface roughness wavelength which can be detected at the resolution ζ, can be written as (see [74])

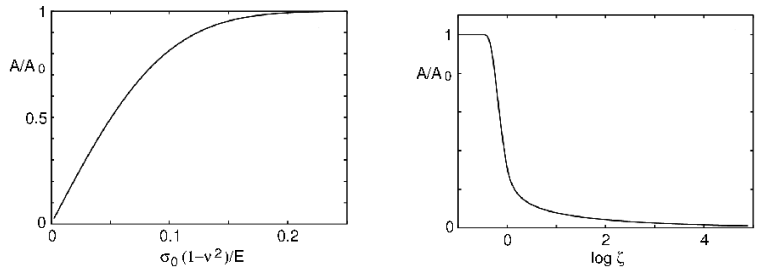

(a) (b)

Abbildung 2.6: (a) The dependence of the normalized contact area (at the highest magnification) A/A_0 on the squeezing pressure σ_0 (in units of $E/(1-\nu^2)$). (b) The dependance of A/A_0 on the logarithm of the magnification.

$$P(\sigma,\zeta) = \frac{1}{A_0}\int_A \mathrm{d}^2x\ \delta(\sigma - \sigma(\mathbf{x},\zeta)) \tag{2.19}$$

with $\sigma(\mathbf{x},\zeta)$ being the stress at the interface when only the surface roughness components with wavevector $q < \zeta q_L$ is considered. The integral in Eq. (2.19) is performed over the area of contact A. Integrating over the whole surface area A_0, the stress probability function would have a delta function $[(A_0 - A)/A_0]\delta(\sigma)$. However this is excluded in this approach. From the stress distribution it is possible to directly obtain the area of real contact projected on the xy-plane. It follows from Eq. (2.19) that

$$P(\zeta) = \frac{A(\zeta)}{A_0} = \int \mathrm{d}\sigma\ P(\sigma,\zeta) \tag{2.20}$$

Eq. (2.19) satisfies (2.17) assuming complete contact. With some appropriate boundary conditions and assuming that Eq. (2.17) holds locally also when only partial contact occurs, the area of (apparent) contact can be derived from Eq. (2.17)

$$\frac{A(\zeta)}{A_0} = \frac{1}{\sqrt{\pi}}\int_0^{\sqrt{G}} \mathrm{d}x\ \mathrm{e}^{-x^{2/4}} = \mathrm{erf}\left(\frac{1}{2}\sqrt{G}\right) \tag{2.21}$$

where $G(\zeta)$ is given by Eq. (2.18).

The dependence of the normalized contact area (at the highest magnification) A/A_0 on the squeezing pressure σ_0 is shown in Fig. 2.6 (a), whereas (b) shows the dependence on the magnification. For low squeezing pressures the approach by Persson predicts a linear increase of the contact area with the load, see Fig. 2.6 (a). In (b) $\zeta = 1$ refers to the resolution $\lambda_0 = 2\pi/q_0$ for a constant nominal pressure σ_0. Increasing the magnification introduces shorter and shorter roughness wavelength

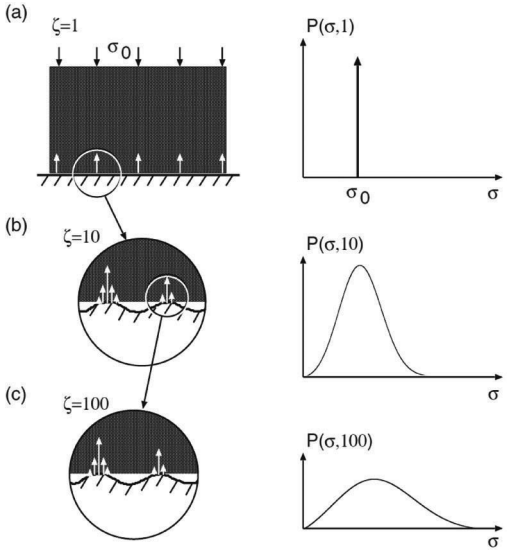

Abbildung 2.7: The stress distribution in the contact region between a rigid block and an elastic substrate at increasing magnification ζ. At the lowest magnification $\zeta = 1$ the substrate looks smooth and the block makes apparent contact with the substrate in the whole nominal contact area leading to a delta function in the stress distribution. As the magnification increases the area of contact decreases while the stress distribution becomes broader and broader.

components, so that the area decreases monotonically, and if no short distance cut-off (atomic dimension) would exist, the true contact area would vanish.
The theory of Persson is quiet flexible, so that adhesional interaction and plastic deformation can be included. Thus, if the local pressure at the asperity contact regions at high magnifications becomes high enough the material yields plastically. In this case the size of the real contact area is determined mainly by the yield stress of the solids.

The predictions of the two theories presented above have already been studied numerically in order to test which method gives better results [8, 40, 87, 113]. In the following sections several experimental tests are presented to test the theory of Persson. In addition, these experiments also show how the theory can be applied to engineering problems. The approaches are briefly introduced, and the theory predictions are compared with experimental data that has been produced in order to test the approach on contact mechanics by Persson.

3 Interfacial Separation between Solids

In this section the interfacial separation and its importance to mechanical engineering is explained. It is then shown how the mean interfacial separation between two contacting solids can be calculated using the theory of Persson. An experimental method to test the theory predictions is introduced and the results from the experiment are then compared with the predictions of the multiasperity approach by Bush, Gibson and Thomas as well as of the approach by Persson.

When two elastic solids with rough surfaces are squeezed together, because of surface roughness, the solids in general do not form contact everywhere in the apparent contact area but only at a distribution of asperity contact spots. The separation $u(\mathbf{x})$ between the surfaces varies in a nearly random way with the coordinates $\mathbf{x} = (x, y)$, as indicated in Fig. 2.3 and 3.1. It is not possible to describe the interfacial separation using simple parameters, because it can only be described as a distribution of interfacial separations. The interfacial separation is of interest, e.g., in the context of the air-pumping contribution to tyre noise, resulting from the compression and outward flow of air between a tyre tread block and the road surface during driving [46]. This is similar to how sound is generated during applause. It is also of importance for the leakage of seals or the heat transfer and the electric conductivity between two solids with randomly rough surfaces.
The work presented below focuses on the mean interfacial separation, as an experimental study measuring the complete distribution would be complicated. The mean value, or average surface separation $u = \langle u(\mathbf{x}) \rangle$, is defined as the distance between the average plane of the lower surface of the block and the average plane of the upper surface of the substrate, see Fig. 3.1. Increasing the applied squeezing pressure on the upper block consequentially leads to a decrease of u [50, 51]. However in most situations it is not possible to squeeze the two solids into full contact corresponding to $u = 0$.

3.1 The Mean Interfacial Separation

Frictionless contact is assumed between an elastic solid (with the Young's modulus E, the Poisson's ratio ν) with a flat surface squeezed against a rigid, randomly rough surface with the surface height profile $z = h(\mathbf{x})$. In Sec. 2.2.1 it has already been described that if $h_1(\mathbf{x})$ and $h_2(\mathbf{x})$ describing the surface profiles, E_1 and E_2 are the Young's elastic moduli of the two solids, and ν_1 and ν_2 are the corresponding Poisson's ratios, then the elastic contact problem is equivalent to the contact between

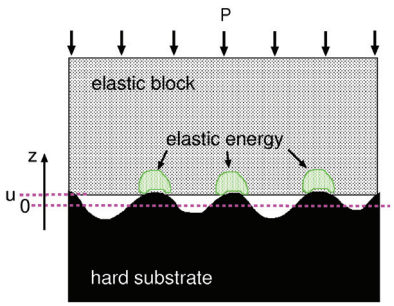

Abbildung 3.1: An elastic block squeezed against a rigid rough substrate. The separation between the average plane of the substrate and the average plane of the lower surface of the block is denoted by u. The elastic energy is stored in the block in the vicinity of the asperity contact regions.

a rigid solid (the substrate) with the roughness profile $h(\mathbf{x}) = h_1(\mathbf{x}) + h_2(\mathbf{x})$, in contact with an elastic solid (the block) with a flat surface and with Young's modulus E and Poisson's ratio ν chosen so that Eq. (2.4) is satisfied.

The mean interfacial separation between the two bodies is denoted by u with $u \geq 0$. The work done by the external pressure p in order to squeeze the two solids into contact is stored as elastic energy in the upper block in the vicinity of the asperity contact regions. Assuming a purely elastic block, so that no energy gets dissipated during the squeeze process, it can be shown that

$$\int_u^\infty \mathrm{d}u \; A_0 p(u) - U_{\mathrm{el}} = 0 \tag{3.1}$$

where A_0 is the nominal contact area. Rearranging Eq. (3.1) for $p(u)$ gives

$$p(u) = -\frac{1}{A_0}\frac{\mathrm{d}U_{\mathrm{el}}}{\mathrm{d}u} \tag{3.2}$$

For elastic solids the two equations (3.1) and (3.2) are in fact exact [78, 113]. But they also hold true for viscoelastic materials if the compression happens so slowly that negligible energy dissipation (caused by the internal friction of the solid) occurs during the compression. It is well known that, for low squeezing pressures, the area of real contact A varies linearly with the squeezing force $F_{\mathrm{N}} = p(u)A_0$, and that the (normalized) interfacial stress distribution, as well as the size distribution of contact spots, are independent of the applied pressure [63, 76]. The reason for this is that with increasing $p(u)$ the existing contact areas grow while also new contact areas form in such a way, that in the thermodynamic limit (infinite-sized system), the quantities referred to above remain unchanged. From this follows immediately

that for small loads the elastic energy stored in the asperity contact regions also increases linearly with the load, so that $U_{\mathrm{el}}(u) = u_0 A_0 p(u)$ is true. Here u_0 is a characteristic length (of order the root-mean-square-roughness) depending on the nature of the surface roughness and which is independent of the squeezing pressure $p(u)$. The detailed description of how u_0 can be calculated is given in [113]. Using Eq. (3.2) one gets

$$p(u) = u_0 \, \frac{\mathrm{d}p}{\mathrm{d}u} \tag{3.3}$$

or

$$p(u) \sim e^{-u/u_0} \tag{3.4}$$

This exponential relation between the average distance and the applied pressure is predicted by the contact mechanics theory of Persson, but differs drastically from the predictions of the multiasperity theories, which for the same system predict

$$p(u) \sim u^{-a} \; e^{-bu^2} \tag{3.5}$$

Later experimental results will be compared with the theoretical predictions of Eq. (3.4) and Eq. (3.5). To derive the relation $p(u)$ in a more general case, an analytical expression for the asperity induced elastic energy must be used, given by the approach by Persson [75, 76]:

$$U_{\mathrm{el}} \approx A_0 \, \frac{E}{1-\nu^2} \, \frac{\pi}{2} \int_{q_0}^{q_1} \mathrm{d}q \; q^2 \; P(q,p) \; C(q) \tag{3.6}$$

Here, in the simplest approximation, $P(q,p)$ is the relative contact area $A(\zeta)/A_0$ when the contact is studied at the magnification $\zeta = q/q_0$ as a function of the applied pressure p. $C(q)$ is the surface roughness power spectrum (see Sec. 2.1). Substituting Eq. (3.6) in (3.2) gives for small squeezing pressures

$$p(u) = \beta \frac{E}{1-\nu^2} \; e^{-u/u_0} \tag{3.7}$$

For self-affine fractal surfaces, the characteristic length u_0 and the parameter β depend on the Hurst exponent H, the long distance roll-off wavevector q_0 as well as on the short distance cut-off wavevector q_1. Most surfaces which are self-affine fractal have a Hurst exponent $H \geq 0.5$ (or a fractal dimension $D_{\mathrm{f}} \leq 2.5$). For these surfaces u_0 and β are nearly independent from the highest surface wavevector (q_1) included in the analysis. Using $1/(1-\nu^2) \approx 4/3$ (since for rubber $\nu \approx 0.5$) and with the squeezing pressure $p = \sigma = F/A_0$ one can also write Eq. (3.7) as

$$\log\left(\frac{\sigma}{E}\right) = \log\left(\frac{4\beta}{3}\right) - \frac{u}{u_0} \tag{3.8}$$

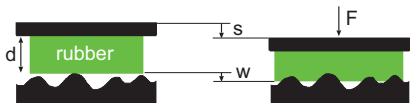

Abbildung 3.2: A rubber block in contact with a rigid, randomly rough substrate. *Left*: No applied load. *Right*: The rubber block is squeezed against the substrate with the normal force F. The upper surface of the block moves downwards by s, whereas the mean plane of the deformed lower surface penetrates inside the surface roughness by the distance w.

3.2 Experimental Method

Consider a rubber block (elastic modulus E) with a flat surface (area A_0) and thickness d. If the block is squeezed against a rigid, randomly rough counter surface, the upper surface of the block will move downwards by the distance s as indicated in Fig. 3.2. This movement is the sum of basically two different effects. The lower surface of the rubber block penetrates a distance w into the valleys or cavities of the counter surface and elastic energy is stored up as described above. There also occurs an uniform compression of the rubber block which can be calculated using $d\sigma/E$. Thus, the downward movement is described by

$$s = w + d\sigma/E \tag{3.9}$$

If u denotes the average separation between the block and the substrate (so that $u = 0$ corresponds to perfect contact) then, assuming that the initial position of the lower surface of the block corresponds to the separation where the block just forms contact with the highest substrate asperity with the height $h_{\max}$ above the average substrate surface plane, one can write

$$w = h_{\max} - u \tag{3.10}$$

Combining Eq. (3.9) and (3.10) gives

$$u = h_{\max} - s + d\sigma/E \tag{3.11}$$

Substituting Eq. (3.11) in (3.6) leads to

$$\log\left(\frac{\sigma}{E}\right) = \log\left(\frac{4\beta}{3}\right) - \frac{1}{u_0}\left(h_{\max} - s + d\,\frac{\sigma}{E}\right) \tag{3.12}$$

with $B = \log(4\beta/3) - h_{\max}/u_0$ one can also write

$$\log\left(\frac{\sigma}{E}\right) = B + \frac{1}{u_0}\left(s - d\,\frac{\sigma}{E}\right) \tag{3.13}$$

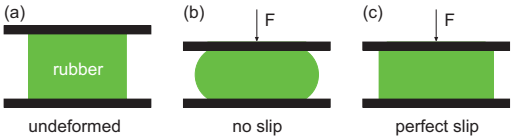

Abbildung 3.3: A rubber block between two flat and rigid solid plates. (a) Undeformed state. (b) Squeezed block assuming no slip at the rubber-plate interfaces, i.e. because of high enough static friction. (c) Squeezed block assuming perfect slip at the rubber-plate interfaces.

Depending on the interfacial slip conditions between the rubber and the upper and lower rigid solids, it is necessary to replace the elastic modulus E in the formulas above with the effective elastic modulus $E' \geq E$. In Fig. 3.3 the two extreme cases are shown. Applying a normal load on the plates results in a deformation of the elastic block from the undeformed state (see Fig. 3.3 (a)) to a deformed state. If the friction at the interfaces is low enough, e.g. lubricated surfaces, perfect slip can occur and for this case, the elastic modulus remains unchanged, see (c). However when there is no slip, the rubber block deforms as indicated in Fig. 3.3, and for this case the effective modulus is higher compared with perfect slip conditions. The confinement of the surfaces of the elastic block leads to a buckling in the lateral direction. The increase of the effective modulus can be estimated using the Lindley equation [34]

$$E' \approx E\ (1 + 1.4\ S^2) \tag{3.14}$$

where S is the shape factor. For a cylinder, the shape factor can be calculated as $S = R/2d$. With the effective elastic modulus E', Eq. (3.13) takes the form

$$\log\left(\frac{\sigma}{E'}\right) = B + \frac{1}{u_0}\left(s - d\ \frac{\sigma}{E'}\right) \tag{3.15}$$

where $B' = log(4\beta E/3E') - h_{\max}/u_0$.

Another case that also can happen is schematically shown in Fig. 3.4 (b). Here one of the rigid plates exhibits surface roughness, resulting in perfect slip at the upper interface and no slip conditions at the rough interface.

3.3 Experimental Procedure and Conditions

In the experimental studies presented below, a rubber block with a nominal flat surface is squeezed against different types of road samples with randomly rough surfaces. The procedure is schematically shown in Fig. 3.2 and 3.4. The block gets squeezed into the surface roughness cavities by changing the displacement s of the upper surface of the rubber block in small steps. For each step, the restoring force F is measured. For this experiment an instrument was used, shown in Fig. 3.5, produced

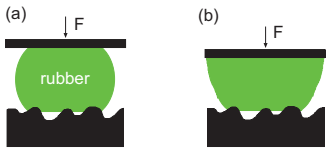

Abbildung 3.4: A rubber block squeezed between a rigid solid plate and a rigid randomly rough substrate: (a) dry surfaces and (b) lubricated upper surface.

by SAUTER GmbH (Albstadt, Germany). The displacement can be changed with a resolution of 0.01 mm while the force sensor can measure forces up to 500 N with an accuracy of 0.1 N.

Abbildung 3.5: Picture of the instrument produced by SAUTER GmbH (Albstadt, Germany) used in the experiment. A rubber block is squeezed against different surface samples. The displacement s of the upper surface of the rubber block is changed in steps while the restoring force F is measured by a force cell.

The rubber block used in this study is made out of PDMS (polydimethylsiloxane), a widely used silicone elastomer with purely elastic behavior. Hence the condition for purely elastic deformation as required in Sec. 3.1 is satisfied. The PDMS samples are prepared using a two-component kit (Sylgard 184) from Dow Corning (Midland, MI). The kit consists of a base (vinyl-terminated polydimethylsiloxane) and a curing agent (methylhydrosiloxane-dimethylsiloxane copolymer) with a suitable catalyst. From these two components a mixture of 10:1 (base/cross linker) in weight is prepared. Variating the ratio between base and curing agent changes the Young's modulus of the rubber block. The mixture needs to be degassed in order to remove the trapped

air induced from the stirring process. It is then poured into cylindrical casts to produce PDMS blocks with diameter $D = 30$ mm and height $h = 10$ mm. The bottom of these casts is made from glass to obtain a smooth PDMS surface with negligible surface roughness. Finally, the samples are cured in an oven at 80° C for over 12 hours to activate the crosslinking process.

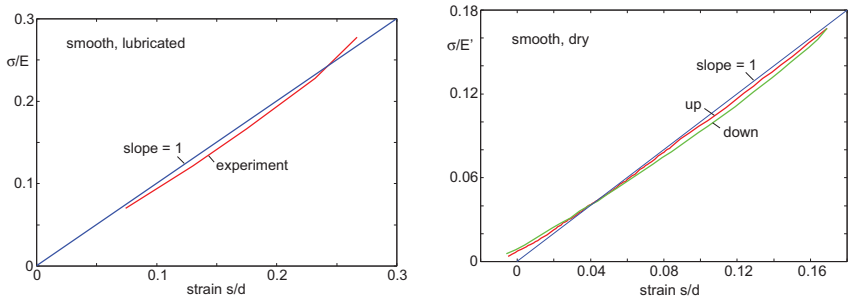

(a) (b)

Abbildung 3.6: The stress σ in units of the elastic modulus E as a function of the strain s/d, where s is the displacement of the upper surface and d the thickness of the block. In (a) the elastic modulus for the PDMS block confined between smooth and lubricated (wet) surfaces is $E = 2.3$ MPa. For (b) the PDMS block is confined between smooth and dry surfaces. The effective elastic Modulus $E' = 4.2$ MPa. The two experimental curves in (b) correspond to increasing and decreasing the strain showing that the block deforms purely elastic.

In the first experiment the elastic modulus E has been measured by squeezing the PDMS block between two flat surfaces. Therefore three different tests were made with (a) both interfaces lubricated (wet), (b) both interfaces not lubricated (dry) and with (c) only one of the two interfaces lubricated. The lubricant used was polyfluoroalkylsiloxane (PFAS), a fluorinated silicone oil with high viscosity ($\eta = 1000$ cSt). Because of its high viscosity, the fluid is an excellent lubricant also in extreme pressure applications and should therefore not be easily squeezed out of the contact area. It also does not react (or interdiffuse) with the PDMS elastomer. For dry interfaces, the PDMS sample deforms laterally at the force free area, as shown in Fig. 3.3 (b). The reason for this is, that the rubber is nearly incompressible and the block is not able to slip at the interfaces. Lubricating the upper and lower surface results in perfect slip and the rubber block deforms as shown in Fig. 3.3 (c).

Fig. 3.6 (a) shows the results for the relation between the stress and the strain for case (c) (lubricated interfaces) so that the shear stress at the boundaries vanishes. The stress has been normalized with $E = 2.3$ MPa so that a nearly straight line with slope 1 is observed. This shows that the relation $\sigma = Es/d$ holds. The elastic

modulus of $E = 2.3$ MPa is consistent with the elastic modulus reported in the literature for similar silicon rubbers [7, 100]. Repeating the experiment, as well as the other experiments described below, the data never differs by more than ≈ 2.5 %.

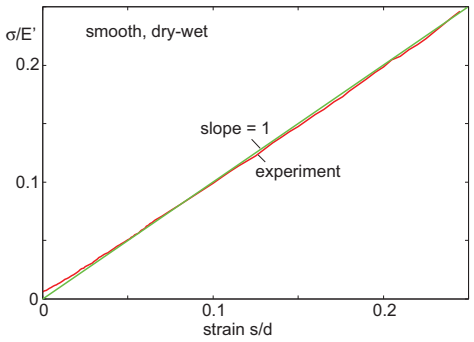

Abbildung 3.7: The same as in Fig. 3.6 for a rubber block confined between a lubricated (wet) and a dry surface. The effective elastic modulus is $E' = 2.9$ MPa.

Repeating the experiment with the same settings as before but this time with no lubricant (dry) at the contacting areas, no or negligible slip occurs at the interfaces with the confining walls. Thus the PDMS block bulges laterally at the force free areas, see Fig. 3.3 (b). Still a linear (or nearly linear) relation between stress and strain is expected but the effective elastic modulus E' should be larger then that for case (a). Thus the effective elastic modulus deduced from the experimental data $E' \approx 4.2$ MPa is about 80 % larger than for lubricated interfaces. To test the system for hysteresis effects, some of the experiments were performed bidirectional. One result is shown in Fig. 3.6 (b), where the strain was carefully increased stepwise and then slowly decreased again. The hysteresis observed is so small that it can be neglected. This is in fact expected because of the low glass transition temperature of PDMS. The increase in the effective elastic modulus in the compression test, from 2.3 MPa to 4.2 MPa, going from slip to non-slip boundary conditions is consistent with the predictions of the Lindley equation (3.14). In this case $E = 2.3$ MPa with the shape factor for a cylinder $S = R/(2d) = 15$ mm$/(2 \cdot 10$ mm$) = 0.75$ gives an effective elastic modulus of $E' = 4.1$ MPa. This agrees very well with the measured value of 4.2 MPa.

In Fig. 3.7 the results are shown for case (c), where one of the interfaces is lubricated while the other one is dry. Here the rubber displaces laterally in an asymmetric way (as indicated in Fig. 3.4 (b)) and the measured elastic modulus $E' = 2.9$ MPa is slightly smaller than the average of the effective modulus obtained assuming no slip and complete slip on both surfaces: $(2.3 + 4.2)/2$ MPa ≈ 3.3 MPa).

In this first comparison of experimental data to the theoretical predictions of

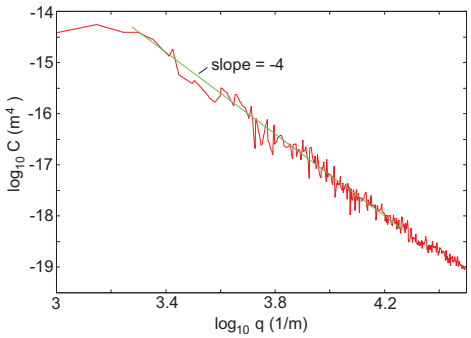

Abbildung 3.8: The surface roughness power spectrum C of the asphalt road surface 1 as a function of the wavevector q on a log-log scale. The straight green line has the slope -4, corresponding to the Hurst exponent $H = 1$ and fractal dimension of $D_\mathrm{f} = 2$.

the mean interfacial separation, three different surfaces were used. All surfaces are road surfaces with rather large surface roughness that have been cut from a road. The topography was measured with optical methods using a chromatic sensor with two different optics produced by Fries Research & Technology GmbH (Bergisch Gladbach, Germany). The statistical analysis of the samples has been carried out to calculate the surface roughness power spectrum. The first surface sample is used to validate the approach by Persson while the results obtained with the other two samples are used to compare the predictions of the theory of Persson with the multiasperity contact theories. Below, the most important data about the surface roughness of the three surfaces is summarized:

Surface 1 is an asphalt road surface. The calculated power spectrum is plotted in Fig. 3.8. It has a root-mean-square roughness of $h_\mathrm{rms} \approx 0.29$ mm and for wavevectors $q > q_0 \approx 2500\ \mathrm{m}^{-1}$ it can, on a log-log scale, be well approximated with a straight line with the slope corresponding to a self-affine fractal surface with $D_\mathrm{f} = 2.0$. For $q < q_0$ the power spectrum $C(q)$ is approximately constant so that q_0 can be referred to as the roll-off wavevector. Unlike the other two surfaces there was no picture of this sample available.

Surface 2 is an asphalt road surface shown in Fig. 3.9 (a). A fractal dimension of $D_\mathrm{f} = 2.15$ can be deduced from the power spectrum shown in Fig. 3.10 (a). In order to compare the two theories, the quantities $m_0 = \langle h^2 \rangle = 0.091\ \mathrm{mm}^2$, $m_2 = 0.5\ \langle \nabla h^2 \rangle = 2.67$, $m_4 = 2.1{\cdot}10^4\ \mathrm{mm}^{-2}$ and $\alpha = 263$ have been calculated. The highest point of the surface is located at a distance $h_\mathrm{max} = 1.37$ mm from the mean plane. The height probability density function is shown in Fig. 3.10 (b).

Surface 3 is a concrete road surface. The power spectrum is shown in Fig. 3.11 (b) and for wavevectors $q > q_0 \approx 630\ \mathrm{m}^{-1}$ a fractal dimension of $D_\mathrm{f} = 2.3$ has been calculated. The moments of the power spectrum are $m_0 = \langle h^2 \rangle = 0.071\ \mathrm{mm}^2$, $m_2 = 0.5\ \langle \nabla h^2 \rangle = 0.27$, $m_4 = 62\ \mathrm{mm}^{-2}$ and $\alpha = 60$. The highest point is located a distance $h_\mathrm{max} = 1.1$ mm from the mean plane. The power spectrum as well as the height probability density function can be seen in Fig. 3.11 (a) and (b) respectively.

(a) Surface 2 (b) Surface 3

Abbildung 3.9: Pictures of two surfaces used for the experimental investigation. (a) An asphalt road surface, denoted as surface 2. (b) A concrete road surface denoted as surface 3.

The height probability function of the surfaces 2 and 3 deviate from the ideal Gaussian distribution, which is the implicit assumption of the BGT and the theory of Persson. However, the ensemble averaged height distribution, which has not been calculated, may be much closer to Gaussian. In any case the deviation of the measured height probability distribution from a Gaussian distribution is not large and it is believed that BGT and the approach on contact mechanics by Persson can still be applied.

3.4 Experimental Results

This section deals with the experimental data that has been measured using the experimental approach reported on above. In Sec. 3.4.1 the results from the experiment on surface 1 is compared with the results of the contact mechanics theory of Persson. The following section also compares the predictions of the most advanced multiasperity theory, namely the BGT theory, with the experimental information from surface 2 and 3, as well as to the predictions of the approach by Persson.

Fig. 3.12 shows the PDMS block squeezed against surface 3. Since PDMS is transparent one can study how the number and the size of the contact areas increases when the compressive force is slowly increased from zero pressure (a) to maximum

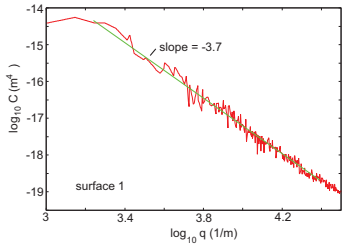

(a) Power spectrum

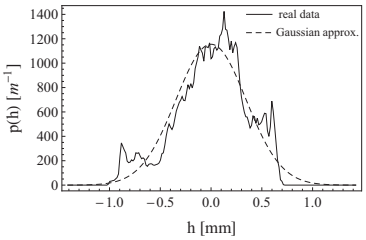

(b) Height probability

Abbildung 3.10: The surface roughness power spectrum $C(q)$ (a), and the height probability density function (b), for surface 2. The straight line in (a) has the slope -3.7, corresponding to a fractal dimension $D_\mathrm{f} = 2.15$, while in (b) the dashed line represents a Gaussian approximation.

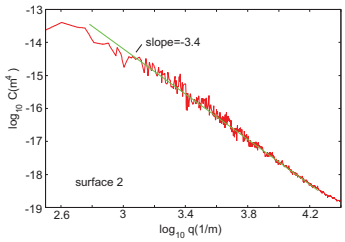

(a) Power spectrum

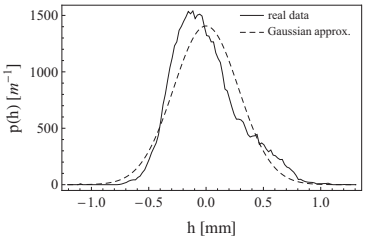

(b) Height probability

Abbildung 3.11: The surface roughness power spectrum $C(q)$ (a), and the height probability density function (b), for surface 3. The straight line in (a) has the slope -3.4, corresponding to a fractal dimension $D_\mathrm{f} = 2.3$, while in (b) the dashed line represents a Gaussian approximation.

pressure (d). First only the largest asperities come into contact and deform the rubber. At the highest pressures the contact looks to the naked eye as nearly complete, and it can be understood that the elastic coupling between nearby asperities will have a strong influence on the contact formation.

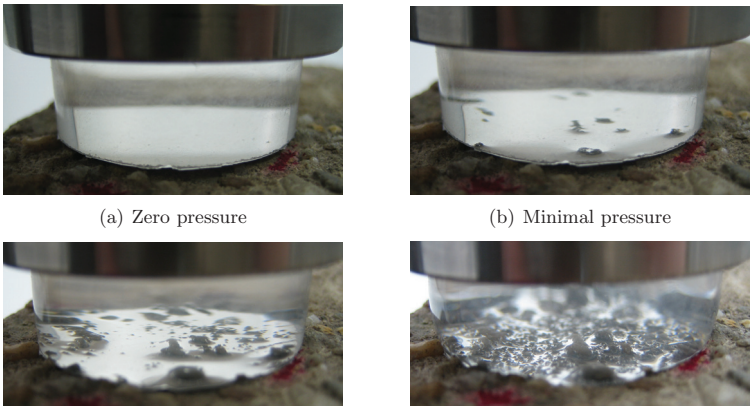

(a) Zero pressure (b) Minimal pressure

(c) Medium pressure (d) Maximum pressure

Abbildung 3.12: Pictures of the rubber sample forming contact and penetrating into the surface roughness valleys with increasing normal pressure. The dark area is where the rubber is in contact with the substrate.

3.4.1 Comparison to the Theory of Persson

The PDMS rubber block has been squeezed into contact with surface 1 as shown schematically in Fig. 3.2. The displacement of the upper surface of the block has been changed in steps of 0.05 mm while the repulsing force is measured. The red and blue lines in Fig. 3.13 show the results of two measurements for the natural logarithm of the squeezing pressure (divided by the effective elastic modulus) as a function of $s - d\sigma/E'$, where s is the displacement of the upper surface of the rubber block relative to the substrate, and where d is the thickness of the rubber block. The green line is the theory prediction (Eq. (3.13)) where $E' = 4.8$ MPa and $B' = -6.85$ have been used. The value of B' has been calculated using Eq. (3.15) so that the only uncertain parameter was the effective Young's modulus E'. However it agrees rather well with the measurements for flat and not lubricated surfaces ($E' = 4.2$MPa), see Fig. 3.6 (b).

The experiment has been repeated with lubricated surfaces in order to test the influence of the effective elastic modulus and the predictions of the Lindley equation (3.14). Here the effective elastic modulus used in the analysis is $E' = 3.4$ MPa and $B' = -6.50$. The results are shown in Fig. 3.14 plotted in the same way as in Fig.

3.13. The value for B' is slightly smaller than for dry contacts. The difference $\delta B' = -6.50 - (-6.85) = 0.35$ reflects the difference in the effective elastic modulus since according to Eq. (3.15) $\delta B' = \log[E'(\text{dry})/E'(\text{lubricated})] = \log(4.8/3.4) \approx 0.35$. The value is larger than E' measured for flat lubricated surfaces (here $E = 2.3$ MPa), but this can be explained as follows.

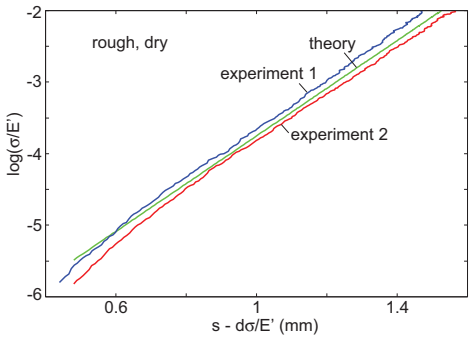

Abbildung 3.13: The natural logarithm of the squeezing pressure, divided by the effective elastic modulus, as a function of the penetration $s - d\sigma/E'$. For the analysis the effective elastic modulus $E' = 4.8$ MPa and $B' = -6.85$ were used. The two experimental curves were obtained using two different silicon rubber blocks, produced in the same way. The results are for dry contact.

Visual inspection of the contact between the rubber cylinder and the two confining walls showed that, as expected from above, the rubber block slips against the top (flat) steel surface while no slip, or only very limited slip, occurs against the rough substrate surface, see Fig. 3.4 (b). This is consistent with the fact that the observed elastic modulus is larger than $E = 2.3$ MPa, as obtained above when complete slip occurs at both (lubricated) interfaces. In fact, the observed effective Young's modulus (3.4 MPa) is quite close to the value 2.9 MPa measured for smooth surfaces when slip occurs at one surface and no-slip at the other surface. The fact that no (or very small) slip occurs at the interface between the rubber and the rough substrate surface may be due to at least two facts:

(1) The pressure in the asperity contact regions is much higher than the average pressure, and the asperity contact regions are much smaller than the nominal contact area, resulting in a much faster squeeze out of the lubricant from the asperity contact regions as compared with the case of flat surfaces. This consequently leads to higher friction in the contact regions.

(2) The substrate surface roughness on different length scales contributes to the friction during slip due to viscoelastic deformations of the rubber on different length scales. However, since for silicon rubber viscoelastic dissipation only occurs at very high frequencies, it is likely that this effect is small for the presented system.

The measured E'-values for rough surfaces (4.8 and 3.4 MPa) are roughly 15 % larger than for smooth surfaces (4.2 and 2.9 MPa), as obtained assuming no slip on the confining surfaces in one case, and no slip on only one of the confining surfaces in the other case. The origin of this (small) difference in effective elastic modulus is not known. For $s - d\sigma/E' < 0.6$ mm the experimental curves in Fig. 3.13 and 3.14 drop off faster then predicted by the theory of Persson when the interfacial separation becomes larger. This is a finite size effect. The theoretical approach was developed for an infinite system which has arbitrary many and arbitrary high asperities, so that contact between the two solids will occur already at arbitrary large surface separations and the relation $p \sim \exp(-u/u_0)$ holds for arbitrary large u. However a finite system has asperities with height below some finite length $h_{\max}$, and for $u > h_{\max}$ no contact occurs between the solids so that $p = 0$.

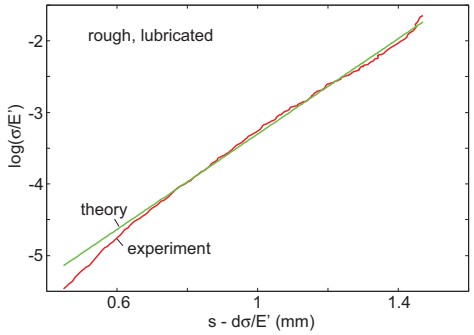

Abbildung 3.14: The same as in Fig. 3.13 for lubricated (wet) contact. Here $E' = 3.4$ MPa and $B' = -6.50$ are used to calculate the predictions of the approach by Persson for the given system.

The presented combined experimental - theoretical study of the contact between a rigid solid with a randomly rough surface and an elastic block with a flat surface shows nearly perfect agreement between theory predictions and experimental data.

It is concluded that for non-adhesive interaction and small applied pressure the relation $p \sim \exp(-u/u_0)$ holds true (similar qualitative results were obtained in [25]). The only parameter that needs to be adjusted due to a lack of information is the effective elastic modulus E' of the PDMS cylinder in contact with a rough and a smooth hard counter surface. However, taking into account the uncertainty about the slip boundary conditions at the contacting interfaces, the values for E' are consistent with the theoretical values of the Lindley equation. The experimental results indicate that for surfaces with fractal-like roughness profiles the contact mechanics theory of Persson may be exact for the fractal dimension $D_\mathrm{f} = 2.0$ [79]. A comparison to the multiasperity contact theories is presented in the following section.

3.4.2 Comparison to BGT and the Theory of Persson

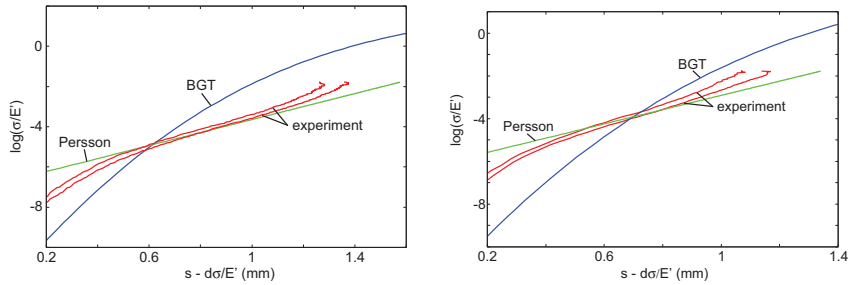

(a) Surface 2

(b) Surface 3

Abbildung 3.15: The natural logarithm of the quantity σ/E' as a function of $s - d\sigma/E'$ for surface 2 and 3, under dry conditions (no-slip). The effective elastic modulus is $E' = 4.2$ MPa.

The same experimental procedure as for surface 1 was used for the test with surfaces 2 and 3 too. The experimental data is shown in Fig. 3.15 (a) and (b) (red lines). Here an effective elastic modulus of 4.2 MPa has been assumed as deduced from the experiments for smooth and dry surfaces and also predicted by the Lindley equation. In each figure the results of two experiments have been presented to give an indication of the precision of the experiment. Other experiments performed gave results located in between the two red lines shown in the figures. The predictions of the BGT theory is shown as blue line while the green line is the predictions of the theory of Persson. Both plots show that the predictions of the approach by Persson are in relative good agreement with the experiments, while the BGT theory does not show good agreement. This is true even for large separations where multiasperity theories are believed to be correct. However, a detailed study shows that multiasperity theories require in addition, that the surfaces roughness occurs on only one length scale. It can be concluded that the BGT theory (and in general

multiasperity contact models) cannot be utilized to correctly describe the mean interfacial separation as a function of the applied load. This approach not only fails quantitatively but also qualitatively.

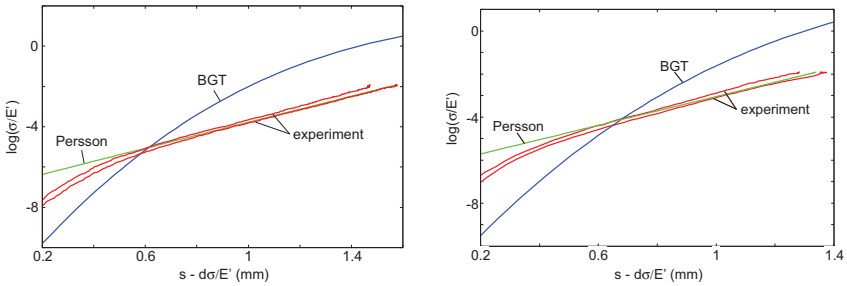

(a) Surface 2 (b) Surface 3

Abbildung 3.16: The natural logarithm of the quantity σ/E' as a function of $s - d\sigma/E'$ for surface 2 and 3, under dry conditions (no-slip). The effective elastic modulus is $E' = 4.8$ MPa.

For large separations the same deviation between theory and experiment as in Sec. 3.4.1 can be observed. Again, this is a finite size-effect: for a finite size system σ must rapidly decrease to zero as u approaches $h_{\max}$. The figures confirm the correctness of the predicted exponential law between the separation u and the applied pressure σ for the tested surfaces with fractal dimensions of $D_{\mathrm{f}} = 2.15$ and 2.3. A slightly different slope can be observed in Fig. 3.15 (a) and (b) for small interfacial separations. This completely disappears if E' in the analysis is changed from 4.2 MPa to 4.8 MPa as in Sec. 3.4.1. This is illustrated in Fig. 3.16 where nearly perfect agreement between the experimental data and the predictions of the contact mechanics theory of Persson occurs.

3.5 Summary on the Interfacial Separation

Experimental results for the average interfacial separation as a function of the nominal contact pressure have been presented. The results are in very good agreement with the predictions of the contact mechanics theory of Persson while the predictions of the BGT model differ even qualitatively from the experimental data. The experiments involved squeezing a PDMS rubber block against three different rough surfaces with different surface properties. The multiasperity contact theories, of which the most accurate is the BGT model, are believed to give reasonable results for very small normal pressures and therefore large separations. However comparing BGT predictions to the experimental results, agreement cannot even be found in this limiting case. The curves are described nicely by an exponential function of the type $\sigma \sim e^{-u/u_0}$, as it is predicted by the Persson model.

Summarizing this first combined experimental comparison of the BGT theory and the approach on contact mechanics by Persson it can be concluded that the multiasperity theories predict a wrong dependance of the mean interfacial separation on the squeezing pressure. The experimental results could be explained very well by the theory of Persson.

4 Leak Rate of Static Seals

Seals are devices of huge importance in numerous engineering systems. Their essential functions are to prevent fluid leakage, to retain a pressure difference and to protect the working fluid and moving machine elements from contamination. Despite their importance there still does not exist an appropriate physical model to correctly describe the leakage of a fluid at the seal substrate interface. The dimensioning of a sealing system is until now mainly based on expertise and empirical procedures that has developed only little over the last decades. This is due to a lack of insight about how to describe what is happening when the seal forms contact with the hard substrate. In this chapter a new approach to this problem is presented based on percolation theory and the contact mechanics theory of Persson. It is then compared with experimental data obtained using a simple device.

4.1 Introduction to Seals

Every year approximately 1.1 million tons of mineral oil based lubricants are used in Germany. About 50% of the annual demand can be recovered by recycling and/or further utilisation of waste oil, while the other half, approximately 500.000 tons, is lost to the environment. There are several reasons for this. It can be either *system induced*, e.g burning of oil in a combustion engine, because of *accidents* or due to *leakage* [65]. Thus understanding the leakage of seals is not only of academic interest, but it is also of great importance in order to minimize the loss of lubricant to the environment (to prevent environmental pollution), and for economic reasons [22]. In addition to improve the understanding of seals, the following work has been done to test the contact mechanics theory of Persson. Two very important elements of contact mechanics are tested within this approach, namely the predictions for the **real area of contact**, and the **interfacial separation** in the non-contacting regions.

Fig. 4.1 shows the schematics of a static seal. A rubber seal is pressed with a constant pressure P_0 against a hard counter surface, e.g. steel, separating the fluid under the hydrostatic pressure P_a on the left hand side, from the fluid under the hydrostatic pressure P_b to the right-hand side. Because of surface roughness an interfacial fluid flow will occur at the interface between the rubber and the hard substrate driven by the pressure difference $\Delta P = P_\mathrm{a} - P_\mathrm{b}$. Despite the apparent simplicity of the shown sealing system, it is not easy to describe the interfacial fluid flow and until now there does not exist any good model to calculate this leak rate.

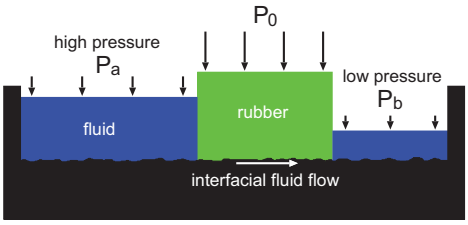

Abbildung 4.1: Schematic picture of a rubber seal separating two fluids under the hydrostatic pressure P_a and P_b from each other. Because of the pressure difference and of surface roughness at the rubber-seal interface, fluid will flow from the high to the low pressure side.

This lack of understanding arises from the problem that one needs to understand what happens in the apparent contact area.
In the following sections a physical model is described to predict the interfacial fluid flow. The predictions of this model is then tested by comparing it to experimental data obtained in a simple model experiment [52, 53, 54, 55].

4.2 Theory Approach by Persson

Looking at the seal from a top view, it is assumed that the nominal contact region between the rubber and the hard counter surface is rectangular with the lateral size L_x and L_y. The high pressure fluid region is for $x < 0$ and the low pressure region for $x > L_x$. The contact area is separated/divided into squares with the lateral length of $L_x = L$ and the area $A_0 = L^2$ as indicated in Fig. 4.2.

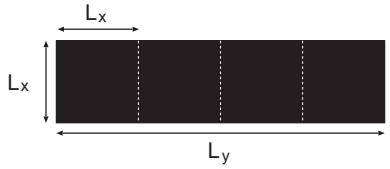

Abbildung 4.2: The rubber-counter surface apparent contact area is rectangular $L_x \times L_y$. It is divided into $N = L_y/L_x$ square areas with side $L = L_x$ and area $A_0 = L^2$.

Studying the contact between the two solids within one of the squares, the magnification ζ is defined as $\zeta = L/\lambda$, where λ is the resolution. At the lowest magnification one cannot observe any surface roughness and the contact between the solids seems to be complete, $A(\zeta = 1) = A_0$. This is indicated in Fig. 4.3 (a), where the real area

of contact projected on the xy-plane is shown in black color. Increasing the magnification introduces surface roughness and the contact will not appear to be complete any longer, so that one now observes regions where the rubber is not in contact with the substrate (white color). Increasing the magnification ζ further (i.e decreasing λ) introduces smaller and smaller surface roughness components. This leads to a monotonic decrease of the real area of contact as shown in Fig. 4.3 (b) - (f). For the highest magnification (atomic resolution), the real area of contact ends up to be only about 33 % of the nominal contact area. During this process of magnifying into the contacting region, one will at a certain point observe the formation of a percolating path of non-contact area from the high to the low pressure side. This channel forms at the critical magnification $\zeta = \zeta_{\text{crit}}$, and the most narrow constriction along this percolating path is denoted as the *critical constriction*. Increasing the magnification further leads to the formation of additional channels that have smaller constrictions then the critical constriction. These channels allow the fluid to leak through the rubber-substrate interface.

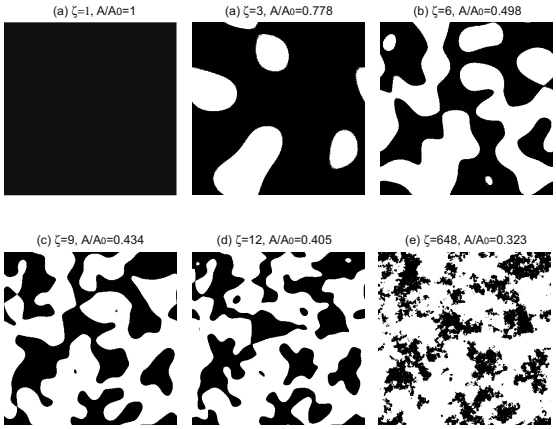

Abbildung 4.3: The contact region at different magnifications (ζ = 1, 3, 6, 9, 12 and 648) is shown in (a) - (f) respectively. When the magnification increases from 9 to 12 the non-contact region percolates. The plotted data shows the results of Molecular Dynamics simulations of the contact between elastic solids with randomly rough surfaces, from [92].

In the following sections two different theories are presented in order to calculate the fluid flow from the high pressure side to the low pressure side through the channels. They are referred to as:

- Single Junction Theory
- Effective Medium Theory

Within the single junction theory only the very first channel is considered that appears when the magnification is increased. This is also the biggest channel through which most of the fluid will flow. The effective medium theory takes into account also the smaller channels that appear when the magnification is increased even further.

4.2.1 Single Junction Theory

As shown in Fig. 4.3, introducing more and more surface roughness to the analysis of the contact formation between an elastic body and a rigid surface finally leads to the formation of a percolating channel of non-contact region at the critical magnification ζ_{crit}. Along this percolation channel a most narrow constriction can be observed that is referred to as the critical constriction. Within this approach, the whole pressure drop is assumed to occur at this single junction [83, 85, 92].

It is assumed that the nominal contact region between the rubber seal and the counter surface is rectangular with the contact area $L_x \times L_y$ (with $L_x < L_y$). For further considerations, the contact patch is "divided" into regions with side $L_x = L_y = L$ and area $A_0 = L^2$. This assumes that $N = L_y/L_x$ is an integer, but this restriction does not affect the final result.

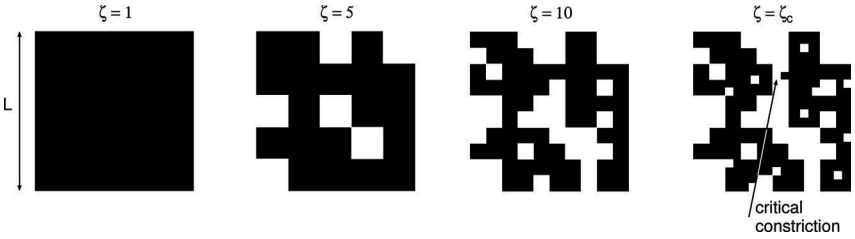

Abbildung 4.4: Schematic picture of the contact region at different magnifications. The non-contact area (white) percolates at $A(\zeta_{\mathrm{crit}}) \approx 0.4 A_0$ and the critical constriction appears.

The critical magnification ζ_{crit} is determined by assuming that the apparent relative contact area $A(\zeta)/A_0$ for $\zeta = \zeta_{\mathrm{crit}}$ is given by percolation theory. Thus, the relative contact area $A(\zeta_{\mathrm{crit}})/A_0 \approx 1 - p_{\mathrm{c}}$, where p_{c} is the so-called percolation threshold [105]. For infinite-sized 2D systems and assuming site percolation $p_{\mathrm{c}} \approx 0.70$ for a hexagonal lattice, 0.59 for a square lattice and 0.50 for a triangular lattice [105]. For bond percolation the corresponding numbers are 0.65, 0.50 and 0.36, respectively. For continuous percolation in 2D the Bruggeman effective-medium theory predicts $p_{\mathrm{c}} = 0.50$. Here it is assumed that for an infinite system the non-contact area percolates when $p_{\mathrm{c}} \approx 0.60$ so that $A(\zeta)/A_0 \approx 0.40$. It is known that for finite-sized systems the percolation, on the average, occurs for slightly smaller values of p_{c} and fluctuations in the threshold are also noticeable between different realizations of the same physical system [96]. For the following analysis it will be assumed that percolation occurs for

$p_c \approx 0.50$. This is also what is used in the effective medium approach presented later. Using the contact mechanics theory of Persson [74, 75, 76, 87, 113] and assuming that $A(\zeta)/A_0 \approx 0.50$, one can calculate the (critical) magnification ζ_{crit} where the first channel of non-contact area percolates. The following expression relates the ratio between real area of contact and apparent area of contact to the magnification ζ:

$$\frac{A(\zeta)}{A_0} = \frac{1}{(\pi G)^{1/2}} \int_0^{P_0} \mathrm{d}\sigma \ \mathrm{e}^{-\sigma^2/4G} = \mathrm{erf}\left(\frac{P_0}{2G^{1/2}}\right) \tag{4.1}$$

where

$$G(\zeta) = \frac{\pi}{4}\left(\frac{E}{1-\nu^2}\right)^2 \int_{q_0}^{\zeta q_0} \mathrm{d}q \ q^3 C(q) \tag{4.2}$$

with the surface roughness power spectrum

$$C(q) = \frac{1}{(2\pi)^2} \int \mathrm{d}^2x \ \langle h(\mathbf{x})h(\mathbf{0})\rangle \mathrm{e}^{-i\mathbf{q}\cdot\mathbf{x}} \tag{4.3}$$

Here the $\langle ... \rangle$ stands for ensemble average, $h_{(\mathbf{x})}$ is the height profile of the rough surface, while E and ν are the Young's elastic modulus and the Poisson's ratio of the rubber.

Using Eq. (4.1) it is now possible to calculate the critical magnification ζ_{crit} where the ratio $A(\zeta)/A_0 \approx 0.50$. Knowing the critical magnification, the lateral size of the critical constriction $\lambda_c = L/\zeta_{\text{crit}}$. The separation between the two interfaces at this point is denoted by u_c. It can be calculated (or estimated) as $u_c \approx u_1(\zeta_{\text{crit}})$ using the contact mechanics theory of Persson. Here $u_1(\zeta)$ is defined to be the average height separating the surfaces which appear to come into contact when the magnification decreases from ζ to $\zeta - \Delta\zeta$, where $\Delta\zeta$ is an infinitesimal small change in the magnification. In Fig. 4.6 (a) the black area is the asperity contact regions at the magnification ζ. The green area is the additional contact area forming when the magnification is reduced to $\zeta - \Delta\zeta$ while $u_1(\zeta)$ is the average surface separation in this green area. The quantity $u_1(\zeta)$ is a monotonically decreasing function of ζ, which can be calculated from the average interfacial separation $\bar{u}(\zeta)$ and $A(\zeta)$ using [113]

$$u_1(\zeta) = \bar{u}(\zeta) + \bar{u}'(\zeta)A(\zeta)/A'(\zeta) \tag{4.4}$$

where $\bar{u}(\zeta)$ is the average separation between surfaces in the apparent contact regions observed at the magnification ζ. It can be calculated from

$$\bar{u}(\zeta) = \sqrt{\pi} \int_{\zeta q_0}^{q_1} \mathrm{d}q \ q^2 C(q) w(q,\zeta) \int_{p(\zeta)}^{\infty} \mathrm{d}p' \ \frac{1}{p'} e^{-[w(q,\zeta)p'/E^*]^2} \tag{4.5}$$

where $p(\zeta) = p_0 A_0/A(\zeta)$ and

$$w(q,\zeta) = \left(\pi \int_{\zeta q_0}^{q} \mathrm{d}q' \; q'^3 C(q')\right)^{-1/2} \tag{4.6}$$

Knowing the lateral dimension (width and length) $\lambda_c \approx L/\lambda_c$ and the height $u_c = u_1(\zeta_{crit})$ of the critical constriction, one can estimate the leak rate by assuming that all the leakage occurs through the critical percolation channel and that the whole pressure drop $\Delta P = P_a - P_b$ occurs over the critical constriction. Increasing the magnification even further leads to the formation of more percolating channels between the surfaces but with more narrow constrictions then the first channel. As a first approximation the contribution to the leak rate from these channels is neglected.

The critical constriction is now approximated as a pore with rectangular cross-section of width and length λ_c and height $u_c << \lambda_c$. Assuming an incompressible Newtonian fluid, the volume flow per unit time through the critical constriction is given by (Poiseuille flow)

$$\dot{Q} = \alpha \frac{u_1^3(\zeta_c)}{12\eta} \Delta P \tag{4.7}$$

where η is the fluid viscosity. In deriving (4.7) laminar flow is assumed and that $u_c << \lambda_c$, which is always satisfied in practise. Another assumption is no-slip boundary condition on the solid walls. This may not always be satisfied at the micro or nano-scale, but is likely to be a very good approximation in the present case owing to surface roughness which occurs at length scales shorter than the size of the critical constriction.

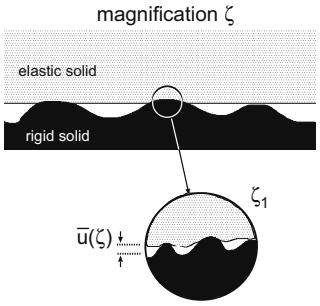

Abbildung 4.5: An asperity contact region observed at magnification ζ. It appears that complete contact occurs but increasing the magnifications to the highest (atomic scale) magnification ζ_1, it is observed that the solids are actually separated by the average distance $\bar{u}(\zeta)$.

In Eq. (4.7) a factor α is introduced which depends on the exact shape of the critical constriction, but which is expected to be of order unity. For a channel with

rectangular shape and a height much smaller than the lateral dimensions, the flow rate is calculated using $\alpha = 1$. However, the real flow channel at the critical constriction will differ from a rectangular cross-section because the pore height must continuously decrease towards zero at the "edges" in the direction perpendicular to the fluid flow. The pore will also not be exactly rectangular in the xy-plane, which also influences α. The separation in the critical constriction also variates within the pore. This is shown schematically in Fig. 4.6 (b) where, because of surface roughness observed at shorter length scales then λ_c, the actual separation between the solid walls in the green area varies around the average $u_1(\zeta)$. Thus it is expected that $u_c = \alpha u_1(\zeta)$ where $\alpha < 1$.

Due to the simplifications of the critical constriction to a rectangular pore and the lack of information about the real shape in the application, α is in this study treated as a fitting factor. Note also that a given percolation channel could have several narrow (critical or nearly critical) constrictions of nearly the same dimension which would reduce the flow along the channel. But in this case one would also expect more channels from the high to the low fluid pressure side of the junction, which would tend to increase the leak rate again. These two effects will, at least in the simplest picture, compensate each other (see discussion in [92]). Finally, since there are $N = L_y/L_x$ square areas in the rubber counter surface contact area, the leak rate can be calculated using

$$\dot{Q} = \alpha \frac{L_y}{L_x} \frac{u_1^3(\zeta_c)}{12\eta} \Delta P \tag{4.8}$$

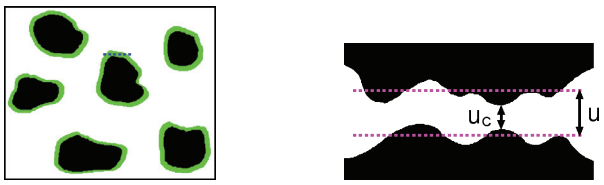

(a) (b)

Abbildung 4.6: (a) The black area represents the asperity contact regions at the magnification ζ. The green area is the additional contact area observed when the magnification is reduced to $\zeta - \Delta\zeta$. The average separation between the solid walls in the green surface area is denoted by $u_1(\zeta)$. (b) The separation between the solid walls along the blue dashed line in (a). Since the surfaces of the solids are rough everywhere, the actual separation between the solid walls in the green area fluctuates around the average $u_1(\zeta)$. At the most narrow constriction the surface separation is u_c.

4.2.2 Effective Medium Theory

The single junction theory presented before assumes that the leak rate is determined by the resistance towards fluid flow through the critical constriction. In reality one observes, with increasing magnification, many flow channels at the interface and all of them contribute to the total leak rate. Here the 2D Bruggeman effective medium theory is used to calculate (approximately) the leak-resistance resulting from the network of flow channels. The effective medium theory is a physical model that is used to describe the macroscopic properties of a medium consisting of random disordered components, in this case random fluctuations in the interfacial separation $u(\mathbf{x})$. For a n-component system, as in this case where the separation u takes n different discrete values, one assumes that the flow in the effective medium is the same as the average fluid flow obtained when circular regions of the n-components are embedded in the effective medium.

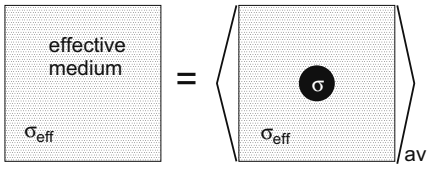

Abbildung 4.7: Effective medium theory takes into account random disorder in a physical system. The equation determining the "effective medium" (e.g. the effective conductivity σ_{eff}) is obtained by calculating some properties of the effective medium and demanding that the same result is obtained by embedding into the effective medium a circular region of one component of the original system, and then averaging over the different components, with weights determined by the fractional areas of the various components in the original physical system.

Using the 2D Bruggeman effective medium theory it can be shown that (see [11, 47, 53] and Fig. 4.7):

$$\dot{Q} = \frac{L_y}{L_x}\sigma_{\text{eff}}\Delta P \tag{4.9}$$

where $\Delta P = P_{\text{a}} - P_{\text{b}}$ is the pressure drop and where (see [53])

$$\frac{1}{\sigma_{\text{eff}}} = \int \mathrm{d}\sigma\ P(\sigma)\frac{2}{\sigma_{\text{eff}}+\sigma} = \int \mathrm{d}\zeta\ \left(-\frac{A'(\zeta)}{A_0}\right)\frac{2}{\sigma_{\text{eff}}+\sigma(\zeta)} \tag{4.10}$$

where

$$\sigma(\zeta) = \frac{[\alpha u_1(\zeta)]^3}{12\eta} \tag{4.11}$$

Eq. (4.10) can be solved by iteration.
However, it is not clear that the effective medium theory gives better results than the single junction theory. The reason for this is the following: In the effective medium model there is no correlation between the size of a region and the (average) separation between the surfaces in the region. In reality, the regions where the surface separation is large are not distributed randomly, but they form large compact and connected regions (since they are observed already at low magnification).

4.3 Experimental Approach to Leakage

This chapter deals with the presentation of the experimental method that has been developed in order to test the theoretical approach towards leak rate of static seals. The method is straight forward and it has been motivated by the simple picture of a seal shown in Fig. 4.1. The actual device is shown in Fig. 4.8 where a rubber seal with rectangular cross-section is attached to the bottom surface of a plexiglass (PMMA) cylinder. The seal is squeezed against a hard solid with well defined surface roughness by the force F_N. The contact between the rubber ring and the counter surface is covered with distilled water. To obtain a pressure difference between the inner and the outer region of the seal, the PMMA cylinder is filled with distilled water up to a fixed height H. The pressure difference $\Delta P = P_a - P_b = \rho g H$, where g is the gravitation constant, ρ the fluid density ($\rho \approx 1.0$ kg/m^3 for distilled water) and H the height of the fluid column. With $H \approx 1$ m, one gets $\Delta P \approx 0.01$ MPa or $\Delta P \approx 0.1$ bar. The leakage of the fluid is detected by measuring the drop in height of the water column as a function of time. Experimental data is for the fluid leak rate as a function of the squeezing pressure P_0 on different rough surfaces. The squeezing pressure is varied by changing the normal force F_N.

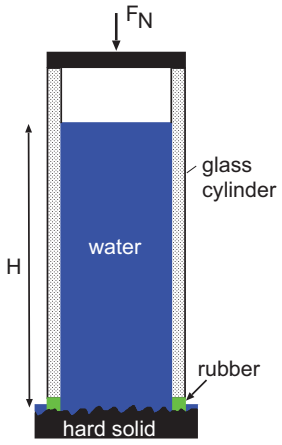

Abbildung 4.8: Experimental device for measuring the leak rate of a static seal. A plexiglas cylinder with a rubber seal attached at the bottom surface is squeezed against a hard counter surface with well-defined surface roughness. A pressure difference is realized by filling water into the cylinder up to a certain height. The leak rate is then detected by measuring the drop of the water column as a function of time.

The rubber seal is made from PDMS (Sylgard 184) with purely elastic behavior

to avoid time dependent deformation or creep of the rubber. The Young's elastic modulus $E = 2.3$ MPa and the Poisson's ratio $\nu = 0.5$ for rubber. The inner and outer diameter is 30 mm and 40 mm, respectively, with a height of 5 mm. The condition $P_0 >> \Delta P$ for this instrument is already satisfied for nominal loads of the order kg. This is necessary in order to avoid the influence of the fluid pressure on the contact mechanics at the interface.

According to Eq. (4.7) it is expected that the leak rate depends linearly on the fluid pressure difference ΔP. In order to test the device, an experiment has been done variating the height of the water column and measuring the corresponding leak rate. The nominal squeezing pressure is kept constant at $P_0 \approx 60$ kPa. The results in Fig. 4.9 show that, within the accuracy of the experiment, the leak rate depends linearly on ΔP.

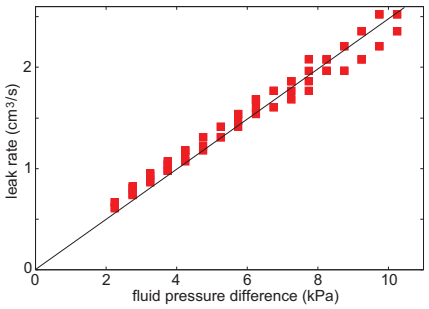

Abbildung 4.9: The leak rate as a function of the fluid pressure difference ΔP for the nominal squeezing pressure $P_0 \approx 60$ kPa. Square symbols are the measured data while the straight line indicates the linear relation between leak rate and ΔP.

4.4 Comparison to the Single Junction Theory

In order to test the theory, experiments have been performed as described before. The substrate in the first test is a randomly rough corundum paper with the grit size 120. Corundum paper is also referred to as sandpaper. It is usually manufactured by bonding small abrasive particles to a sheet of paper typically using a resin bond. This first experiment has been performed using sandpaper because it is available in many different grit sizes. This makes it is easier to find a suitable roughness profile so that the experiment can be done on an acceptable time scale. However, it is not a perfect model surface to apply the contact mechanic theory of Persson since the theory assumes that the average surface slope is not too large. Sandpaper has much larger and sharper roughness than the counter surfaces usually used in normal rubber-seal applications. From a theory point of view it should not really matter

on which length scale the roughness occurs, expect for "complications" such as the influence of adhesion and fluid contamination particles which tend to clog narrow flow channels. Nevertheless, the first validation will be presented using this rather "unsuitable" sandpaper surface.

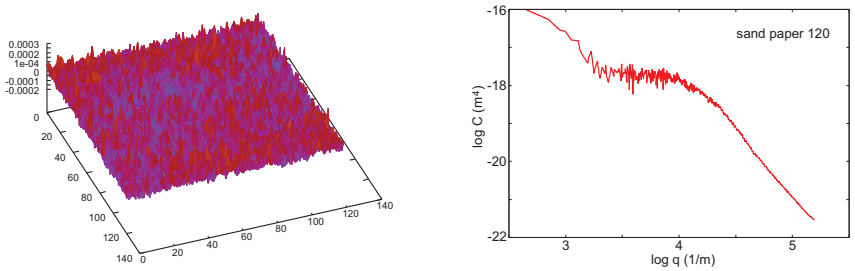

(a) (b)

Abbildung 4.10: (a) shows the surface topography and (b) the surface roughness power spectrum of the sandpaper 120 surface used in the experiment. The root mean square roughness is 44 μm. It consists of hard corundum particles with diameter of order 110 μm glued to the substrate. The surface area (including only roughness with wavelength above $\lambda_1 = 20$ μm) is about 40 % larger than the nominal surface area A_0.

The topography of the sandpaper 120 sheet has been measured using the same optical methods as reported on in Sec. 3.3. The surface topography data is plotted in Fig. 4.10 (a) from which the power spectrum $C(q)$ has been calculated as shown in (b). The measured root mean square roughness of the sandpaper is 44 μm.

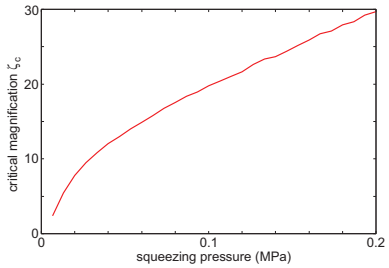

Abbildung 4.11: The calculated critical magnification $\zeta_{\rm crit}$, where the non-contact area percolates, as a function of the squeezing pressure P_0.

According to the procedure that has been introduced in Sec. 4.2.1, first the critical

magnification ζ_{crit}, where the non-contact area percolates, has been calculated using the surface roughness power spectrum and the elastic properties of the PDMS seals. Notice that in this first comparison a percolation threshold of $p_{\mathrm{c}} = 0.6$ has been used. The results are shown in Fig. 4.11 as a function of the applied nominal pressure on the seal. As expected the percolation happens at higher and higher magnifications as the squeezing pressure is increased.

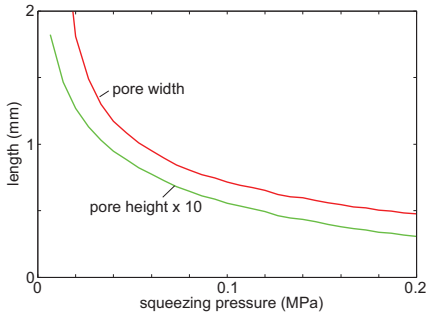

Abbildung 4.12: Calculated critical pore size as a function of the squeezing pressure. The red line is the lateral pore width and length λ_{c} whereas the green curve represents the pore height u_{c} multiplied by a factor 10.

After calculating the critical magnification it is now possible to compute the dimensions of the critical constriction. In Fig. 4.12 the lateral dimensions λ_{c} and the height u_1 are plotted as a function of the squeezing pressure. With increasing normal force, the pore gets smaller and smaller. Note that in the figure the height is multiplied by a factor 10. Thus, the assumption $u_{\mathrm{c}} << \lambda_{\mathrm{c}}$ for the inspected system is fulfilled. Knowing the dimensions of the critical constriction, Eq. (4.8) is used to calculate the leak rate. The experimental data has been obtained by placing the PDMS rubber seal attached to the PMMA tube onto the rough surface. The cylinder is filled with distilled water up to its maximum height and constantly refilled. It is important to ensure that the contact is covered with distilled water. After some fixed time period, in order to get rid of undesired effects that may happen in the first minutes after contact formation, the leak rate is measured by stopping the time the water column needs to drop a (small) specific distance. The experiment is repeated for 10 different squeezing pressures. It has been repeated on several locations on the sandpaper surface with increasing the load and then decreasing it again. The results are shown in Fig. 4.13 (a) and (b). In (a) the measured leak rate is represented by the data points as a function of the squeezing pressure whereas the green and blue squares correspond to two different measurements. The solid line is the calculated leak rate using the surface topography, the measured elastic modulus of the rubber $E = 2.3$ MPa and the fluid pressure difference $\Delta P = P_{\mathrm{a}} - P_{\mathrm{b}} = 10$ kPa. The parameter in Eq. (4.8) has been chosen to be $\alpha = 0.2$, which is in fact in a reasonable

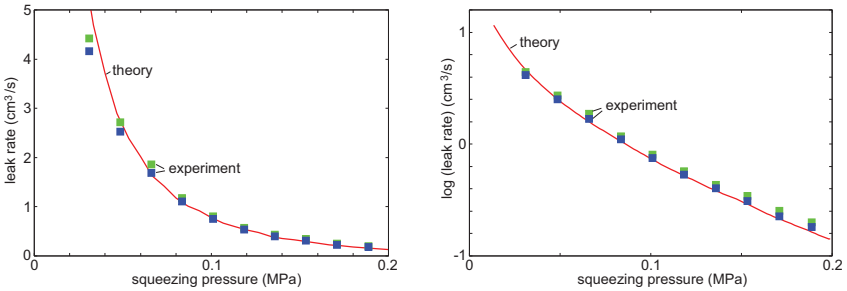

(a) (b)

Abbildung 4.13: (a) Square symbols: the measured leak rate for 10 different squeezing pressures. Solid line: the calculated leak rate using $\alpha = 0.233$. (b) shows the same as in (a) but with natural logarithm of the leak rate for a better illustration.

range. Fig. 4.13 (b) shows the same data as in (a), but with the natural logarithm of the leak rate.

To study how sensitive the theory is on the elastic properties of the seal, the calculated leak rate for $E = 2.5$ MPa and for $E = 1.0$ MPa are shown in Fig. 4.14 (a) and (b). The factor α has been chosen so that in (a) $\alpha = 0.182$ and in (b) $\alpha = 0.625$. Note that the theory predictions are rather insensitive on small changes in the elastic modulus. However, as illustrated in Fig. 4.14 (b), changing E by a factor of ≈ 2 results in a very different contact pressure dependance on the leak rate than observed.

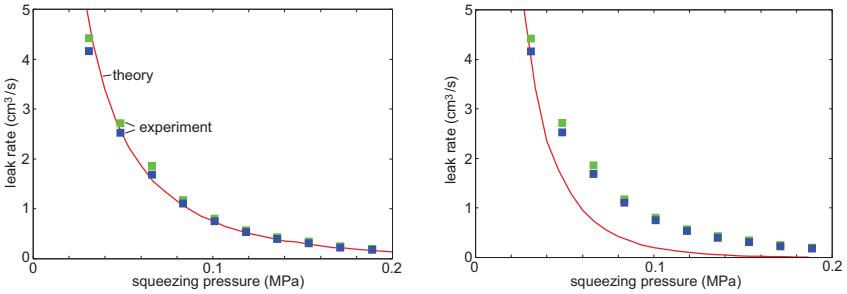

(a) (b)

Abbildung 4.14: The leak rate as a function of the squeezing pressure. For (a) $E = 2.5$ MPa and $\alpha = 0.182$ while for (b) the parameters have been varied to test its influence on the predictions to $E = 1.0$ MPa and $\alpha = 0.625$.

Good agreement was found between the predictions of the single junction theory and the experimental data for a PDMS seal squeezed against a sandpaper surface.

4.5 Comparison to the Effective Medium Theory

The effective medium approach predicts a percolation threshold of $p_c = 0.50$. To compare the predictions of the effective medium theory with those of the single junction theory $p_c = 0.50$ has been used in Sec. 4.2.1 as well. The surfaces used for this comparison are a corundum paper with grit size 120 and two sand-blasted plexiglas plates. The root-mean-square roughness has been calculated from the measured topography to be 44 μm, 34 μm and 10 μm, respectively. The different height probability distributions and the surface roughness power spectra are shown in Fig. 4.15 and 4.16. The roughness profile has been measured using a tactile stylus instrument. Similar to atomic force microscopy, a stylus is brought into contact with the surface probe. It is then moved over the surface while the vertical deflection is measured. It turns out that this method gives much better results than the optical reading of the surface height profile. As already mentioned before, sandpaper consists of particles with sharp edges pointing above the surface while the regions between the particles are filled with a resin binder making the valleys smoother and wider than the peaks. This is the reason for the asymmetry in the height probability distribution P_h as observed.

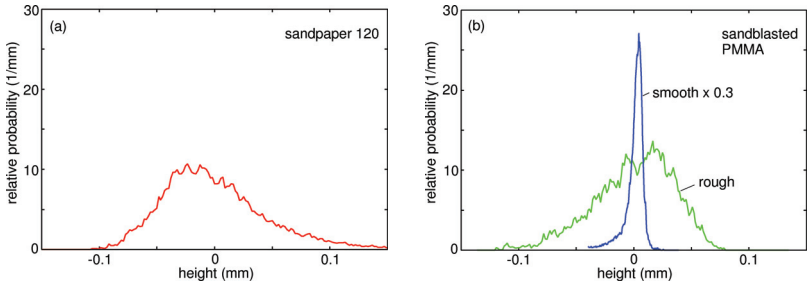

(a) (b)

Abbildung 4.15: The surface height probability distribution of (a) sandpaper 120 and (b) two sand-blasted PMMA surfaces. Note that in (b) the results for the smooth PMMA sample (blue curve) have been multiplied by a factor of 0.3. The surfaces have a root-mean-square roughness of 44 μm, 34 μm and 10 μm respectively. The surface area is about 49 %, 28 % and 10 % larger than the nominal surface area A_0. The distribution is skewed and not perfectly Gaussian.

Randomly rough surfaces have a Gaussian height probability distribution. However in Fig. 4.15 (b) it is observed that, opposite to the sandpaper surface, the plexiglass

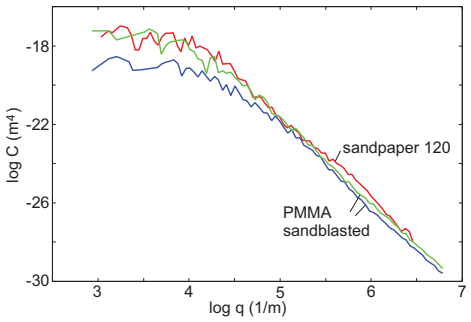

Abbildung 4.16: The surface roughness power spectrum $C(q)$ of sandpaper 120 and two sandblasted PMMA surfaces calculated from the measured topography data.

surfaces are asymmetric with a tail towards smaller h. The PMMA surfaces have been prepared by bombarding smooth plexiglass plates with small hard particles. This results, at least for a short time of sand-blasting, in local indentations (where the particles hit the surface) separated by smoother surface regions, leading to the observed asymmetry in P_h. The root-mean-square roughness of the two plexiglass samples are 34 μm and 10 μm, respectively.

The square symbols in Fig. 4.17 show the logarithmic (with 10 as basis) of the measured leak rate, for several different squeezing pressures, for both the sandpaper surface and for the two sand-blasted PMMA surfaces. The solid lines are the calculated leak rate using the measured rubber elastic modulus $E = 2.3$ MPa and the surface roughness power spectra $C(q)$ shown in Fig. 4.16. The red lines correspond to the predictions of the single junction theory while the green lines represent the effective medium theory. In the calculations α has been chosen to be $\alpha = 0.73$ for the sandpaper 120 surface, and $\alpha = 0.31$ for both PMMA surfaces. Note that the two theories give remarkable similar results and that the parameter α for the sandpaper case approaches 1 as the percolation threshold has been changed to $p_c = 0.50$. The value of α is in a reasonable range, of order unity, as expected before.

Surprisingly, the effective medium theory, where all percolation paths are taken into account, predicts a slightly lower leak rate than the "simple" single junction theory where only the first flow channel is included in the analysis. The explanation for this result may be that in the effective medium model there is no correlation between the size of a region and the average interfacial separation of the two surfaces in this region. In reality however regions with large separations also form large, connected domains. This effect tends to increase the leak rate.

Fig. 4.18 shows the same as Fig. 4.17 but for a wider range of squeezing pressures. It illustrates what happens if the nominal pressure on the seal is increased further and further. The red lines are the results of the single junction theory, whereas the green

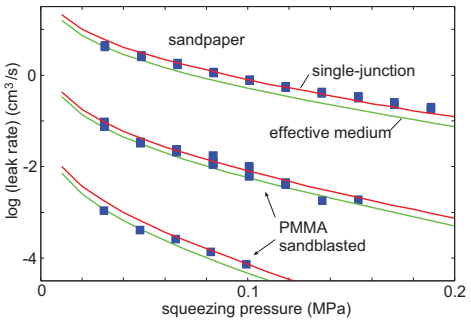

Abbildung 4.17: Square symbols: the measured leak rate for different squeezing pressure for sandpaper (upper data points) and sand-blasted PMMA (lower set of data points). In each case the green line corresponds to the calculated leak rate using the single junction theory whereas the red lines represent the effective medium approach. Input for the calculations has been the measured surface topography, the measured rubber elastic modulus $E = 2.3$ MPa and the fluid pressure difference $\Delta P = P_a - P_b = 10$ kPa obtained from the height of the water column. Here $\alpha = 0.73$ for sandpaper and 0.32 for PMMA.

line shows that the effective medium theory gives nearly the same results. Note that the leak rate of the sandpaper and the two sand-blasted PMMA systems strongly decays until it finally vanishes. Because the magnification can only be increased until it reaches its natural cut-off (of order atomic dimensions), for high enough pressure the condition for the percolation of a flow channel, $A(\zeta)/A_0 \approx 1 - p_c$, will no longer be reached. That is, even for the highest magnification the area of real contact would be too large for a non-contact region to percolate. In the present case this would happen for the squeezing pressures 1.0, 0.85 and 0.49 MPa.

To conclude, it has been shown that both theoretical approaches give nearly the same results for the tested systems. The experimental results are in good agreement with the predicted leak rate, which has been calculated using percolation theory and the contact mechanics theory of Persson. Employing a percolation threshold of $p_c = 0.50$ instead of 0.60 also caused a more realistic value for α.

4.6 Influence of Skewed Surface Roughness

Randomly rough surfaces have a Gaussian height probability distribution. However many surfaces of engineering interest have skewed distributions, as already observed in Sec. 4.5. This may also affect the leak rate of a static seal as can be understood from the following extreme case. A rigid solid block with a flat surface is brought into contact with a rigid substrate with periodic "surface roughness" as indicated

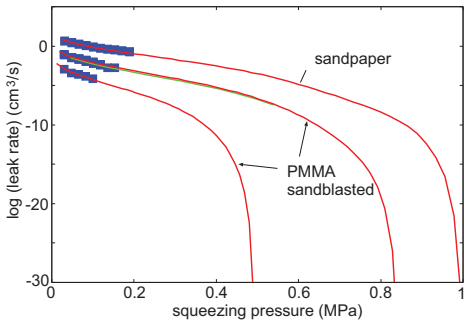

Abbildung 4.18: Same as in Fig. 4.17 but for a larger range of squeezing pressures. The red lines are the results of the single junction theory. The effective medium theory gives practically the same results as illustrated for one rough sandblasted PMMA (green curve).

in Fig. 4.19. The two substrate surfaces shown in (a) and (b) have in fact the same root-mean-square roughness and the same power spectrum. However, intuitively it is easy to understand that for (a) the leak rate should be much larger than in (b) due to the larger empty volume between the surfaces in (a).

In the real application the roughness is of course not periodic and the solids are not rigid but it is expected that the leak rate is larger for a situation where the asymmetry of the height profile is as for case (a). This may also be the physical origin why the factor α is larger for the sandpaper surface compared with the PMMA samples. The surface roughness power spectrum of the rough PMMA surface and the sandpaper 120 are in fact very similar. However the leak rate differs by roughly two orders of magnitude. This indicates that some aspects of the surface topography, not contained in the power spectra, is likely to be of importance. For randomly rough surfaces, the statistical properties of the surfaces are fully contained in the power spectrum.

$$C(\mathbf{q}) = \frac{1}{(2\pi)^2} \int \mathrm{d}^2x \ \langle h(\mathbf{x})h(\mathbf{0})\rangle \mathrm{e}^{-i\mathbf{q}\cdot\mathbf{x}} \tag{4.12}$$

However the surfaces presented before are not perfectly Gaussian (P_h is non-Gaussian) and to account for this, the top and bottom power spectra are defined as follows

$$C_T(\mathbf{q}) = \frac{1}{(2\pi)^2} \int \mathrm{d}^2x \ \langle h_T(\mathbf{x})h_T(\mathbf{0})\rangle \mathrm{e}^{-i\mathbf{q}\cdot\mathbf{x}} \tag{4.13}$$

$$C_B(\mathbf{q}) = \frac{1}{(2\pi)^2} \int \mathrm{d}^2x \ \langle h_B(\mathbf{x})h_B(\mathbf{0})\rangle \mathrm{e}^{-i\mathbf{q}\cdot\mathbf{x}} \tag{4.14}$$

where $h_\mathrm{T}(\mathbf{x}) = h(\mathbf{x})$ for $h > 0$ and zero otherwise, while $h_\mathrm{B}(\mathbf{x}) = h(\mathbf{x})$ for $h < 0$ and zero otherwise. These "rectified" profiles are schematically shown in Fig.

(a) (b)

Abbildung 4.19: The figure shows the contact between a rigid block with a flat surface and a rigid substrate with periodic surface structure. The two substrate surfaces in (a) and (b) have the same surface roughness power spectrum. Note that the empty volume between the surfaces is much larger in case (a) than in case (b), and therefore one would expect the leak rate to be largest.

4.20. It is clear by symmetry that for a randomly rough surface with Gaussian height distribution, $C_{\mathrm{T}}(q) = C_{\mathrm{B}}(q)$. If n_{T} and n_{B} are the fractions of the nominal surface area (i.e. the surface area projected on the xy-plane) where $h > 0$ and $h < 0$, respectively, then one can also define $C^*_{\mathrm{T}}(q) = C_{\mathrm{T}}(q)/n_{\mathrm{T}}$ and $C^*_{\mathrm{B}}(q) = C_{\mathrm{B}}(q)/n_{\mathrm{B}}$. Roughly speaking, C^*_{T} would be the power spectrum resulting if the actual bottom profile (for $h < 0$) was replaced by a mirrored top profile (for $h > 0$). A similar statement holds for C^*_{B}. For randomly rough surfaces with Gaussian height distribution it is expected $C^*_{\mathrm{T}}(q) = C^*_{\mathrm{B}}(q) \approx C(q)$.

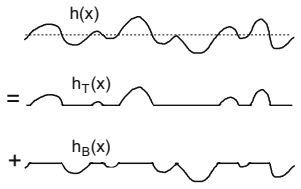

Abbildung 4.20: The surface profile is decomposed into a top $h_{\mathrm{T}}(x)$ and a bottom $h_{\mathrm{B}}(x)$ profile. Using these profiles, the top and bottom power spectra can be calculated.

The contact mechanics theory of Persson can in principle also (approximately) be applied to surfaces with skewed height distributions. For this case it can be shown, that the predictions can be improved if $C^*_{\mathrm{T}}(q)$ is used rather than $C(q)$. It gives a better representation of the surfaces roughness. The reason for this is that, for small squeezing pressures, the rubber will only probe the upper part of the substrate surface roughness profile. Hence the dependence of the area of contact on the magnification, and therefore the critical magnification determining the percolation of non-contact area, will be more accurately described employing $C^*_{\mathrm{T}}(q)$. Using the top power spectrum does not mean that one does not take into account for the surface roughness below the average plane. These region below the average surface plane are in replaced by a mirrored top profile with the same statistical properties

as the top profile. From Fig. 4.19 it is also clear that the largest volume of fluid between the two surfaces will occur above the average surface plane and not below, at least for small squeezing pressures.

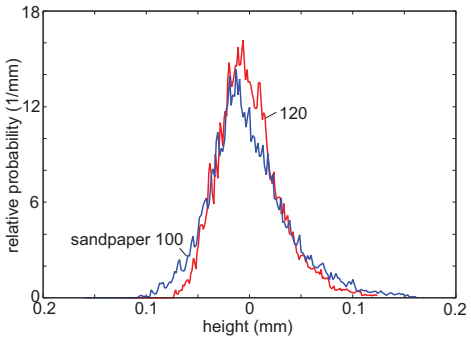

Abbildung 4.21: The surface height probability distribution for the sandpaper 100 and 120 surfaces with the root-mean-square roughness amplitudes 40 μm and 31 μm. The two surfaces have the skewness $\langle h^3\rangle/\langle h^2\rangle^{3/2} = 0.85$ and 0.82 respectively.

To study the influence of skewness on the leak rate, experiments have been performed for the following two systems:

First system: Two corundum (sandpaper) surfaces with grit sizes 100 and 120. The rms roughness of the surfaces (40 μm and 31 μm) has been calculated from the measured surface topography. A stylus instrument has been used to measure the roughness. From this data the height probability distribution $P(h)$ (shown in Fig. 4.21) and the surface roughness power spectra $C(q)$ as well as the top and bottom power spectra (see Fig. 4.22 (a) and (b)) have been deduced. Both surfaces exhibit an asymmetric height probability distribution with a tail towards higher h. This has already been noticed in Fig. 4.15 (a) for a different (but with the same grit size) sandpaper surface. This can be explained by how these surfaces are produced. The sandpaper surface consist of particles with sharp edges pointing above the surfaces while the region between the particles is filled with a resin binder making the valleys smoother and wider than the peaks. This leads to the asymmetry in $P(h)$ as observed.

Second system: Two samples with "inverted" surface roughness profiles of the two sandpaper surfaces described before have been studied. The "negatives" are produced by crosslinking PDMS against the sandpaper surfaces. The samples obtained have inverted surface statistics so that $C^*_{\mathrm{B,sandpaper}}(q)$ now equals $C^*_{\mathrm{T,inverted}}(q)$. To measure the leak rate for this system, the seals have been squeezed against a flat glass substrate.

Comparing the measured leak rate for the configuration flat seal against rough substrate with flat seal with "inverted" roughness against smooth substrate, one can address the problem illustrated in Fig. 4.19.

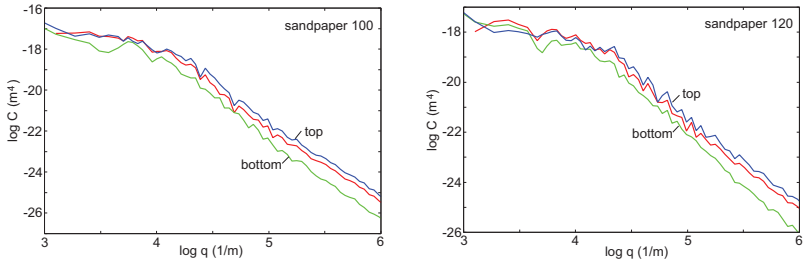

(a) (b)

Abbildung 4.22: The surface roughness power spectrum of (a) sandpaper 100 and (b) 120. The three curves are the original surface roughness power spectrum $C(q)$ (red), and the top $C^*_{\rm T}(q)$ (blue) and the bottom power spectrum $C^*_{\rm B}(q)$ (green). For (a) the root-mean-square roughness is 40 μm and for (b) 41 μm. The fraction of the projected surface area above the average surface plane is about 0.44 and 0.45 for (a) and (b), respectively.

Fig. 4.23 (a) shows the logarithm of the measured leak rate for the sandpaper 100 substrate (upper squares) and for the inverted surface (lower squares) as a function of the squeezing pressure. The solid lines are the calculated leak rate using the single junction theory. The experimental data obtained on the sandpaper 120 substrate as well as the inverted system are shown in (b). The calculation of the top curve uses the top power spectrum $C^*_{\rm T}(q)$ while the leak rate of the inverted systems employs the measured bottom power spectrum $C^*_{\rm B}(q)$ of the sandpaper sample.

Considering the experimental data first, there exist a noticeable difference between the leak rate of the "original" system compared with the "inverted" system. This difference was explained qualitatively already before, and is related to the larger empty volume between the surfaces for the original surface as compared with the inverted surface (see Fig. 4.19). The effect on the leak rate is huge, roughly two orders of magnitude difference. Utilizing the single junction theory and the top power spectrum gives very good agreement between the calculated leak rate and the measured data (upper curves). The fitting parameter α used for the analysis of the first system is $\alpha = 1.0$.

Note that the theory is also able to describe the observed effect or difference between system 1 and 2. Using $C^*_{\rm B}(q)$ of the measured sandpaper surfaces, the calculated leak rate of the inverted system is in good agreement with the experiment (see Sec. 4.23 (a) and (b), lower curves), where $\alpha = 0.8$ is used. However with increasing squeezing pressure the deviation between theory and experiment becomes

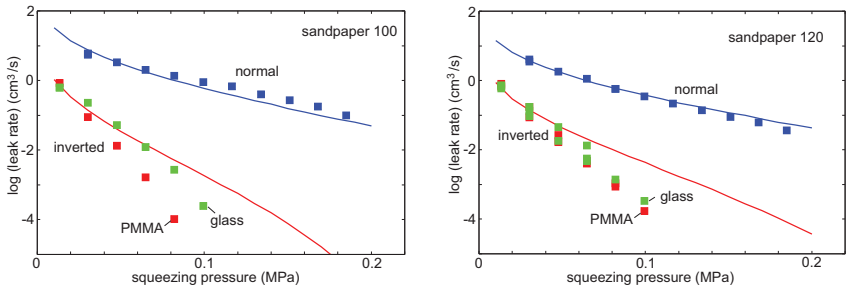

(a) (b)

Abbildung 4.23: Square symbols: the measured leak rate for (a) sandpaper 100 and (b) sandpaper 120 (upper curves) and for the inverted surfaces (lower curves). The solid lines are the calculated leak rate using the single junction theory. The top curves have been calculated using the top power spectrum $C_{\mathrm{T}}^{*}(q)$. For the inverted samples (bottom curves) the bottom power spectrum $C_{\mathrm{B}}^{*}(q)$ was used. The measured elastic modulus of the rubber seal is $E = 2.3$ MPa while the fluid pressure difference $\Delta P = P_{\mathrm{a}} - P_{\mathrm{b}} = 10$ kPa. For the normal system $\alpha = 1.0$ while for the inverted system $\alpha = 0.8$.

larger. This is because the leak rate decreases faster as predicted by the theory. This may be attributed to the influence of adhesion on the contact mechanics and consequently also on the leak rate. The top of the asperities of the inverted surfaces are quite smooth as they arise from the relative smooth resin film in the valleys between the abrasive particles of the sandpaper surface. This feature allows effective adhesion between the asperities on the PDMS seal and the smooth substrate.

When the glass substrate is clean water will almost completely wet its surface so that the work of adhesion between glass and PDMS through water may be zero or even slightly negative. This would lead to a repulsion instead of attraction. However the glass surfaces were not cleaned chemically and therefore probably covered by nanometer thick organic contamination layers. In general, these layers are strongly absorbed to glass. Organic molecules floating in the air are partly oxidized with reactive bonds, and when absorbed on the glass, they may interact with the surface by some strong specific interactions. These molecules are not easy to remove by water. In this case one would expect a dewetting transition in the asperity contact regions between the substrate surface and the silicon rubber surface [10, 91]. This results in an effective adhesion which pulls the surfaces in closer contact than expected taking only the influence of the squeezing pressure into account.

For the case where PDMS is squeezed against a PMMA substrate, the work of adhesion is effectively larger, pulling the seal even into closer contact with the counter surface. This explains the difference in the leak shown in Fig. 4.23 (a). In (b) the

difference is not as big as in (a). This may be due to organic contamination which could not be removed sufficiently and therefore leads to a smaller difference between the two different experiments.

4.7 Influence of the Hydrostatic Pressure on the Leak Rate

In all the calculations presented earlier, the influence of the fluid pressure on the contact mechanics is neglected. This is a good approximation as long as the squeezing pressure P_0 is much higher than the fluid pressure P_{fluid} which is true for all experiments discussed before. However in many practical situations it is not a good approximation to neglect this influence and therefore the influence of the hydrostatic pressure on the leakage is studied in this section. Consider the case where $P_{\text{fluid}} \approx P_0$. Since the fluid pressure for the seal is higher on the fluid entrance side than on the fluid exit side, one expects the elastic body to deform and tilt relative to the average substrate surface plane. This effect consequently leads to higher leakage. To test this effect the experiment has been repeated as described before. The inner and outer diameter of the PDMS seal is 40 mm and 60 mm with a height of 5 mm. The normal force is kept constant in the following experiment at $F_{\text{N}} = 18.5$ N giving a squeezing pressure of 11.8 kPa. Using a water column with the maximal applicable height $H = 1.2$ m gives the fluid pressure $P_{\text{fluid}} = P_{\text{a}} - P_{\text{b}} = 11.8$ kPa at the bottom of the fluid column. This equals the squeezing pressure applied on the seal. If the fluid pressure is larger than the squeezing pressure, the experiment becomes instable and the tube lifts off from the substrate. The substrate used here is the "rough" sandblasted PMMA surface reported on in Sec. 4.5. The height probability distribution and the power spectrum are plotted in the Fig. 4.15 and 4.16 respectively.

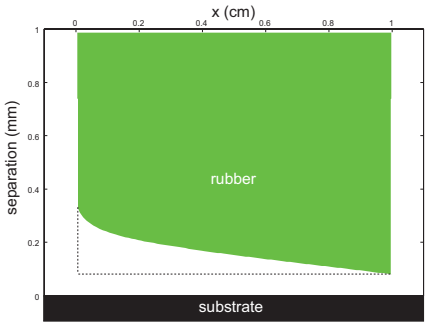

Abbildung 4.24: The shape of the rubber block for $P_{\text{a}} - P_{\text{b}} = P_0$. The nominal squeezing pressure is $P_0 = 11.8$ kPa. The dashed line is the shape of the block when $\Delta P = P_{\text{a}} - P_{\text{b}} = 0$ against a sandblasted PMMA surfaces with the root-mean-roughness 34 μm.

Fig. 4.24 shows the expected calculated shape/deformation of the rubber seal for the case if $P_a - P_b = P_0 = 11.8$ kPa. The dashed line corresponds to no hydrostatic deformation where the average separation is determined by the substrate surface roughness. In this most extreme case, where the system becomes instable and lift off from the counter surface, the main contribution to the area of contact between the two solids is shifted outwards. More results from calculations are presented in Fig. 4.25 (a) and (b). In (a) the contact pressure between the seal and the rough substrate is shown as a function of the distance x between the high-pressure and low-pressure side, for three different cases where $(P_a - P_b)/P_0 = 0,\ 0.5$ and 1.0. The higher the fluid pressure, the lower the contribution of the contact pressure. For $(P_a - P_b)/P_0 = 0$ the contact pressure is highest and independent of the distance x. Increasing the fluid pressure further and further reduces the contact pressure. This is true especially on the high-pressure side of the seal. Fig. 4.25 (b) shows the separation between the average plane of the rough substrate and the lower surface of the seal as a function of the position x.

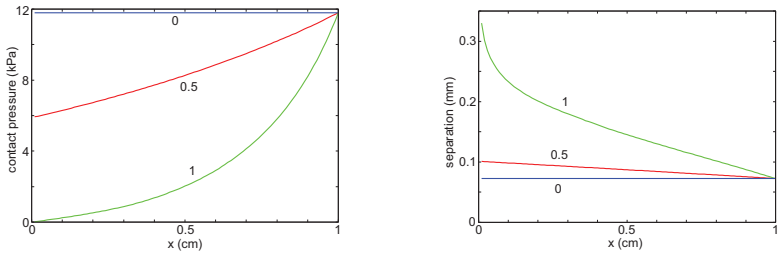

(a) (b)

Abbildung 4.25: In (a) the calculated contact pressure as a function of the distance x between the high-pressure and low-pressure side is shown for the three cases where $(P_a - P_b)/P_0 = 0,\ 0.5$ and 1.0. (b) shows the calculated interfacial separation as a function of x. For sandblasted PMMA with root-mean-square roughness 34 μm.

To test the influence of the hydrostatic pressure the leak rate has then been measured for different water column heights resulting in different fluid pressures $\Delta P = P_a - P_b$. The height is then increased up to the critical fluid pressure where the system becomes unstable. The experimental data is plotted in Fig. 4.26 as square symbols. Note that the fluid leak rate rapidly increases when the fluid pressure approaches the nominal squeezing pressure $P_0 = 11.8$ kPa. The solid lines are the corresponding theory predictions of both the single junction and the effective medium theory. The theory predictions are both in good accordance to the experimental data and the pressure dependance is well described by both approaches. It is interesting to note that the influence of the hydrostatic pressure on the contact mechanics can, as a good simplification, be neglected until it reaches about 60 % of P_0.

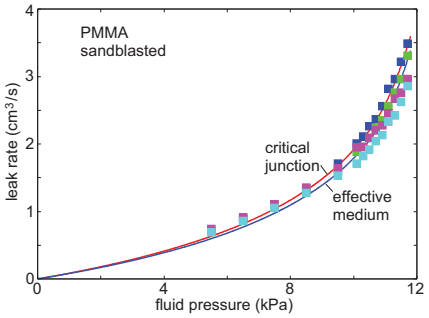

Abbildung 4.26: Fluid leak rate as a function of the fluid pressure difference $\Delta P = P_a - P_b$. The nominal squeezing pressure is $P_0 = 11.8$ kPa. The square symbols are measured data while the solid lines are the theory predictions. In the calculation $\alpha = 0.54$. The substrate is a sandblasted PMMA surface with a root-mean-square roughness of 34 μm.

4.8 Conclusions on the Leak Rate

This study about the leak rate of static seals has been motivated by its importance in technological applications as well as to test the theory of Persson. Based on the approach by Persson and percolation theory a model has been developed to simulate the leak rate. The theory involves the real area of contact as well as the interfacial separation and therefore test both these aspects of the theory of Persson. A series of experiments has been carried out in order to validate this model. Within the comparison it could be demonstrated that the theory is in good agreement with the experimental data. This is true for both systems studied in Sec. 4.2.1 and 4.2.2 respectively. The conclusion is that the predictions of the contact mechanics theory are correct.

It has been found that the qualitative behavior of the leakage is well described by the model. Only the amplitude of the leak rate needs to be adjusted. This could be accomplished by introducing a factor α. This factor has in fact a physical justification and can be explained by the origin of the pores not to be a perfect rectangular pore. Introducing the top and bottom power spectra improved the theory predictions a lot, so that α could be chosen to be of order unity. Also interfaces with skewed surface height profiles can be analyzed using the contact mechanics theory of Persson when the top power spectrum is used in the calculations. This information may in fact be of great importance for many other applications, e.g. rubber friction.

In the last section it was shown that the theory still works well when the fluid pressure is of order the squeezing pressure. Here the fluid-pressure induced elastic deformation of the rubber seal enhances the fluid leakage. However it was shown that

this effect can be neglected until the fluid pressure becomes of order 60 % of the contact pressure P_0. New theory development has been done since the analyzes of the experiments presented above. The extended theory avoids the fitting parameter α. Further studies on the leak rate of seals will be performed to test this new theory and to study the influence of viscoelastic relaxation the rubber and the role of contamination particles which can clog the flow channels. Note that viscoelastic effects are also very important for the types of rubber usually used in seal applications.

5 The Fluid Squeeze-Out

The time dependency of the squeezing out of a fluid from the interface between an elastic solid with a flat surface and a rigid solid with a randomly rough surface is studied. The experimental data is analyzed using a model based on the contact mechanics approach by Persson and the Bruggeman effective medium theory.

The influence of surface roughness on the fluid flow at the interface between two solids in stationary or sliding contact is a topic of great importance in Nature and technology. This includes for example the leakage of static and dynamic seals, mixed lubrication as well as the removal of water between a tire tread block and the road surface. In Nature, fluid squeeze-out is important for the adhesion and grip between the adhesive pads of a tree frog, or a gecko, with the counter surface during rain. For all these applications it is of particular interest how long time it takes to squeezing out the fluid from the contact region between the two solids.

Most objects in engineering have a particular shape characterized for example by a radius of curvature, e.g. the radius R of a cylinder in a combustion engine. To the naked eye the surface may appear perfectly smooth, but on short enough length scales the surface exhibits irregularities, referred to as surface roughness. When studying the fluid flow between two macroscopic solids, the microscopic equations of fluid dynamics may be replaced with effective equations describing the average fluid flow on length scales much larger that the roll-off wavelength λ_0 of the surface roughness power spectrum. This approach of eliminating or integrating out short length scale degrees of freedom to obtain the effective equations of motion, describing the long distance (or slow) behavior, is a common and powerful concept often used in physics.

Patir and Cheng developed in the context of fluid flow at the interface between closely spaced solids with surface roughness a model, showing how the Navier-Stokes equations of fluid dynamics can be reduced to effective equations of motion involving locally averaged fluid pressures and flow velocities [68, 69]. In the effective equations occur so called flow factors. These flow factors are functions of the locally averaged interfacial surface separation which can be determined by solving numerically the fluid flow in small rectangular units with linear size of order (or larger than) the roll-off wavelength λ_0. Recently a new analytical theory to calculate the pressure flow factor was presented by Persson [80]. This approach is based on the contact mechanics theory of Persson and the Bruggeman effective medium theory to take into account the topography disorder resulting from the roughness. This is the same theory that was used in Sec. 4.2 as well.

In the following section, the basic equations of fluid dynamics are presented and some simplifications which are valid in the present analysis are introduced. A detailed description can be found in [55, 56, 80]. After this first part on the theory, the experimental method used to test this approach is described and the experimental results are compared with the theory predictions.

5.1 Fluid Squeeze-Out Theory

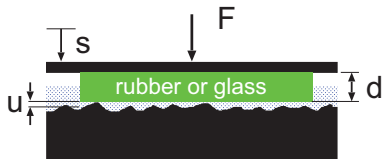

Abbildung 5.1: The squeezing out experimental device (schematically). A cylindrical glass or rubber block is squeezed against a substrate with smooth or rough surface in the presence of a fluid. The cylindrical body has the height $d = 3$, 5 or 10 mm and a diameter of $D = 2R = 30$ mm. The normal load $F_N = 13.8$ N and the fluid viscosity $\eta = 100$ Pas. The vertical displacement s of the upper surface is registered as a function of time.

5.1.1 Fluid Flow between Elastic Solids with Surface Roughness

Consider two elastic solids with randomly rough surfaces. As discussed before, even if the solids are squeezed into contact with a large nominal pressure, because of surface roughness there will in general be non-contact regions at the interface. If the squeezing force is small enough, one will observe non-contact channels from one to the other side of the nominal contact region, see Sec. 4.2. A model has been developed to calculate the fluid flow at the interface between the solids [56]. Assuming a Newtonian fluid and that the fluid velocity field $\mathbf{v}(\mathbf{x}, t)$ satisfies the Navier-Stokes equation:

$$\frac{\partial \mathbf{v}}{\partial t} + \mathbf{v} \cdot \nabla \mathbf{v} = -\frac{1}{\rho} \nabla p + \nu \, \nabla^2 \mathbf{v} \tag{5.1}$$

where $\nu = \eta/\rho$ is the kinetic viscosity and ρ the mass density. For simplicity an incompressible fluid is assumed so that

$$\nabla \cdot \mathbf{v} = 0 \tag{5.2}$$

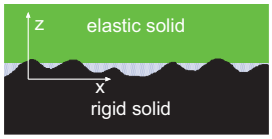

Abbildung 5.2: An elastic solid (block) with a smooth surface in contact with a rigid solid (substrate) with a rough surface in a fluid. Also shown is coordinate system as described in the text.

Assuming that the non-linear term $\mathbf{v} \cdot \nabla \mathbf{v}$ can be neglected. This is true for small inertia and small Reynolds numbers, which is usually the case for fluid flow in between narrowly spaced solid walls. For simplicity the lower solid is assumed to be rigid with a flat surface, while the upper solid is elastic with a rough surface. A coordinate system xyz is introduced with the xy-plane in the surface of the lower solid and the z-axis pointing towards the upper solid as indicated in Fig. 5.2.

The upper solid moves with the velocity $\mathbf{v}_0$ parallel to the lower solid. Let $u(x, y, t)$ be the separation between the solid walls and assume that the slope $|\nabla u| << 1$. Another condition is that $u/L << 1$, where L is the linear size of the nominal contact region. Under these conditions one expects that the fluid velocity varies slowly with the coordinates x and y as compared with the variations in the orthogonal direction z. Assuming a slow time dependency, the Navier Stokes equation reduces to

$$\eta \frac{\partial^2 \mathbf{v}}{\partial z^2} \approx \nabla p \tag{5.3}$$

where $\mathbf{v} = (v_x, v_y)$, $\mathbf{x} = (x, y)$ and $\nabla = (\partial_x, \partial_y)$ are two-dimensional vectors. $v_z \approx 0$ and $p(\mathbf{x})$ is to a good approximation independent of z. The solution of the equation above is

$$\mathbf{v} \approx \frac{1}{2\eta}(z - u_0(\mathbf{x}))(z - u_1(\mathbf{x}))\ \nabla p + \frac{z - u_0(\mathbf{x})}{u_1(\mathbf{x}) - u_0(\mathbf{x})}\ \mathbf{v}_0 \tag{5.4}$$

so that $\mathbf{v} = 0$ on the solid walls at $z = u_0(\mathbf{x})$ and $\mathbf{v} = \mathbf{v}_0$ for $z = u_1(\mathbf{x})$. Integrating over z from $z = u_0(\mathbf{x})$ to $z = u_1(\mathbf{x})$ gives the fluid flow vector:

$$\mathbf{J} = -\frac{u^3(\mathbf{x})}{12\eta}\nabla p + \frac{1}{2}u(\mathbf{x})\mathbf{v}_0 \tag{5.5}$$

Mass conservation demands that

$$\frac{\partial u(\mathbf{x}, t)}{\partial t} + \nabla \cdot \mathbf{J} = 0 \tag{5.6}$$

where the interfacial separation $u(\mathbf{x}, t)$ is the volume of fluid per unit area. In this last equation a slow time dependency of $u(\mathbf{x}, t)$ is allowed as it would be the case during squeezing out of a fluid from the interfacial region between two solids.

5.1.2 Roughness on Many Length Scales

The two equations (5.5) and (5.6) describe the fluid flow at the interface between contacting solids with rough surfaces. The surface roughness can be eliminated or integrated out in using the Renormalization Group (RG) procedure. In this procedure the surface roughness components are eliminated in steps and one obtains a set of RG flow equations describing how the effective fluid equations evolves as the surface roughness is integrated out. It has been shown that after eliminating all roughness components, the fluid current takes the form

$$\mathbf{J} = A(\bar{u})\nabla\bar{p} + B(\bar{u})\mathbf{v}_0 \tag{5.7}$$

where A and B are 2×2 matrices and where $\bar{u}(\mathbf{x}, t)$ and $\bar{p}(\mathbf{x}, t)$ are now locally averaged quantities. A and B are in general also functions of ∇p (see [98]), but for the low pressures and pressure gradients prevailing in the application presented below, they can be neglected. Assuming the sliding velocity $\mathbf{v} = 0$ and surface roughness with isotropic statistical properties, A is proportional to the unit matrix and can be written as $A = -\bar{u}^3\phi_p(\bar{u})/(12\eta)$. Then one gets from Eq. (5.6) and Eq. (5.7)

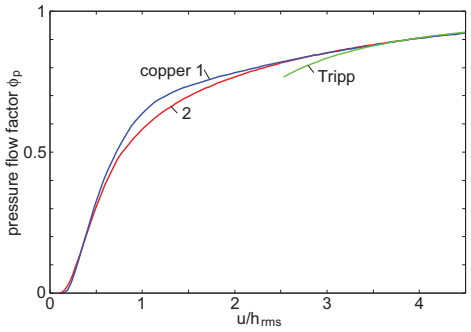

Abbildung 5.3: The fluid pressure flow factor for the two copper surfaces 1 and 2 as a function of the average interfacial separation $\bar{u}$ divided by the root-mean-square roughness amplitude $h_{\rm rms}$. The green curve shows the large $\bar{u}$-behavior predicted by Tripp [108].

$$\frac{\partial\bar{u}}{\partial t} - \nabla\cdot\left(\frac{\bar{u}^3\phi_p(\bar{u})}{12\eta}\nabla\bar{p}\right) = 0 \tag{5.8}$$

Fig. 5.3 shows the pressure flow factor $\phi_p(\bar{u})$ that has been calculated using the contact mechanic theory of Persson and the Bruggeman effective medium theory for two copper surfaces with different surface roughness as described below. Here, the dependance of the flow factor on the separation $\bar{u}$ for the two copper surfaces used

in the experimental study below is shown. The green curve is the large $\bar{u}$-behavior predicted by Tripp [108]:

$$\phi_p \approx 1 - \frac{3}{2}\frac{\langle h^2 \rangle}{\bar{u}^2} \tag{5.9}$$

where $\langle h^2 \rangle = h_{\text{rms}}^2$ is the mean square roughness. The small contact pressure involved in the experiments below results in relative large average separations between the surfaces, $\bar{u} > 1.4 h_{\text{rms}}$ for both surfaces [78, 113] so that $\phi_p(\bar{u})$ is always close to unity in the presented application.

5.1.3 Theory Approach to the Squeeze-Out of a Fluid

The following model has been developed for a cylindrical rubber block, with height d and radius R, squeezed against a substrate in the presence of a fluid. It is assumed that macroscopic deformations of the rubber, due to macroscopically non-uniform fluid pressure, can be neglected. In this case $\bar{u}(\mathbf{x}, t)$ only depends on the time t and Eq. (5.8) implies that the fluid pressure

$$\bar{p} = 2 p_{\text{fluid}} \left(1 - \frac{r^2}{R^2}\right) \tag{5.10}$$

where $r = |\mathbf{x}|$ denotes the distance from the cylinder axis. The average fluid pressure in the nominal contact region is denoted p_{fluid}. Substituting Eq. (5.10) in (5.8) gives

$$\frac{\mathrm{d}\bar{u}}{\mathrm{d}t} \approx -\frac{2\bar{u}^3 \ \phi_p(\bar{u}) \ p_{\text{fluid}}(t)}{3\eta R^2} \tag{5.11}$$

If p_0 is the applied pressure acting on the top surface of the cylinder block, then

$$p_{\text{fluid}}(t) = p_0 - p_{\text{cont}}(t) \tag{5.12}$$

where p_{cont} is the asperity contact pressure. Assume first that the pressure p_0 is so small that for all times $\bar{u} >> h_{\text{rms}}$. Fig. 5.3 shows that for this case one can assume that $\phi_p(\bar{u}) \approx 1$. For large $\bar{u}$ one can use from the theory of Persson:

$$p_{\text{cont}} \approx \beta E^* \exp\left(-\frac{\bar{u}}{u_0}\right) \tag{5.13}$$

with $u_0 = h_{\text{rms}}/\alpha$, where α and β depend on the fractal properties of the rough surface. Employing equations (5.12) and (5.13) in Eq. (5.11) gives

$$\frac{\mathrm{d}p_{\text{cont}}}{\mathrm{d}t} \approx \frac{2\bar{u}^3(p_{\text{cont}}(t))}{3\eta R^2 u_0} p_{\text{cont}} \ (p_0 - p_{\text{cont}}) \tag{5.14}$$

For long times $p_{\text{cont}} \approx p_0$ and Eq. (5.14) simplifies to

$$\frac{\mathrm{d}p_{\text{cont}}}{\mathrm{d}t} \approx \frac{2\bar{u}^3(p_0)}{3\eta R^2 u_0} p_0 (p_0 - p_{\text{cont}}) \tag{5.15}$$

or

$$p_{\mathrm{cont}}(t) \approx p_0 - [p_0 - p_{\mathrm{cont}}(0)] \exp\left(-\left(\frac{\bar{u}(p_0)}{h_{\mathrm{rms}}}\right)^3 \frac{t}{\tau}\right) \tag{5.16}$$

with

$$\tau = \frac{3\eta R^2 u_0}{2h_{\mathrm{rms}}^3 p_0} = \frac{3\eta R^2}{2\alpha h_{\mathrm{rms}}^2 p_0} \tag{5.17}$$

Using Eq. (5.13) leads to

$$\bar{u} \approx u_\infty + \left(1 - \frac{p_{\mathrm{cont}}(0)}{p_0}\right) u_0 \exp\left(-\left(\frac{\bar{u}(p_0)}{h_{\mathrm{rms}}}\right)^3 \frac{t}{\tau}\right) \tag{5.18}$$

where $u_\infty = u_0 \log(\beta E^*/p_0)$. Thus, the separation $\bar{u}(t)$ will approach the equilibrium separation u_∞ in an exponential way. The time to squeeze out the fluid may be defined to be the time it takes to reach, say $1.01u_\infty$, which equals a few times the time constant $\tau' = [h_{\mathrm{rms}}/\bar{u}(p_0)]^3\tau$.

For flat surfaces, within continuum mechanics, the film thickness approaches zero as $t \to \infty$ as $\bar{u} \sim t^{-1/2}$. Thus for this configuration, there is no natural or characteristic timescale and it is therefore not possible to define a meaningful fluid squeeze-out time.

At high enough squeezing pressures and after long enough time, the interfacial separation will be smaller than h_{rms} so that the asymptotic relation in Eq. (5.13) no longer holds. Then the relation $p_{\mathrm{cont}}(\bar{u})$ must be calculated numerically using the contact mechanics theory of Persson. Substituting Eq. (5.12) in (5.11) and measuring pressure in units of p_0, separation in units of h_{rms} and time in units of τ one obtains

$$\frac{\mathrm{d}\bar{u}}{\mathrm{d}t} \approx -\alpha^{-1}\phi_p(\bar{u})\bar{u}^3(1 - p_{\mathrm{cont}}) \tag{5.19}$$

This equation together with the relation $p_{\mathrm{cont}}(\bar{u})$ constitute two equations for the two unknowns $\bar{u}$ and p_{cont} which can be solved numerically.

5.1.4 Rubber Block under Vertical Loading

Consider a cylindrical rubber block with the height d and the radius R squeezed between two flat surfaces. If both surfaces are lubricated so that no friction and therefore perfect slip occurs at the interfaces, the stress at the interfaces is constant $p = p_0 = F_N/\pi R^2$. The change in thickness of the block, Δd, (assuming linear elasticity) is determined using $p_0 = E\Delta d/d$. If the rubber adheres to the upper surface, so that no slip occurs at the contacting interface, the situation can be very different [26, 107]. If $d > R$, the stress at the lower interface will again be nearly uniform and Δd is determined by $p_0 = E_{\text{eff}}\Delta d/d$ where $E_{\text{eff}} > E$ but nearly identical to E. In the opposite limit of a very thin rubber disk, with $d << R$, the pressure distribution is nearly parabolic as shown in Fig. 5.4.

$$p(r) \approx 2p_0[1 - (r/R)^2] \tag{5.20}$$

and the effective elastic modulus $E_{\text{eff}} >> E$. For a substrate with large enough surface roughness, it has been shown that even for a very thin rubber disk the locally averaged pressure distribution at the bottom surface of the rubber disk is nearly constant [97]. The reason for this is that the rubber is pressed into the ridges on the rough surface under vertical loading so that the hydrostatic pressure decreases. Note that while $E_{\text{eff}} > E$ determines the change in the thickness of the rubber block, the asperity-induced elastic deformations at the lower interface are still determined by the Young's modulus E.

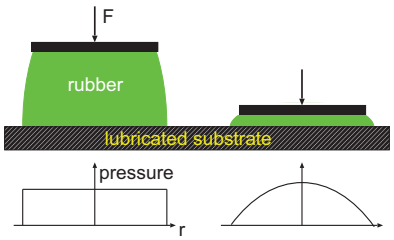

Abbildung 5.4: A cylindrical rubber block (height d and radius R) squeezed against a lubricated substrate (no friction). If $d > R$ the pressure distribution at the interface is nearly uniform (left). For $d \ll R$ (right) the pressure distribution is nearly parabolic. It is assumed that the upper surface of the two rubber cylinders is glued to a flat rigid disk so that no slip occurs at the interface.

It has already been shown (see Eq. (5.10)) that squeezing a flat cylinder surface against a flat substrate in a fluid results in a parabolic fluid pressure distribution. This implies that for a very thin elastic disk, adhered to a rigid and flat upper

surface, the bottom surface is expected to remain nearly flat and the assumption made in Sec. 5.1.3 holds to a good accuracy. However, when the thickness of the rubber block increases so that $d > R$ the bottom surface of the block will bend inwards as indicated in Fig. 5.5. This will slow down the fluid squeezing out because of the trapped fluid.

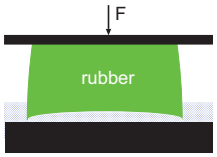

Abbildung 5.5: The non-uniform hydrodynamic pressure is highest at the center of the contact region and deforms the rubber block as indicated if $d > R$. A reservoir of trapped fluid is formed.

5.2 The Squeeze-Out Experiment

The squeezing out of a fluid from the contacting interface between two solids with rough surfaces is studied experimentally. In the experiment a cylindrical silicon rubber block is squeezed against different rough counter surfaces in the presence of a fluid. The experiment is schematically shown in Fig. 5.1 and discussed theoretically in Sec. 5.1. The rubber block is attached to a dead weight resulting in the loading or squeezing force $F_{\mathrm{N}} = 13.8$ N. This normal force is kept constant for all experiments reported on below. A position sensor measures the downwards movement of the dead weight as a function of time. The sensor is a digital gauge with a relative position resolution of 0.5 μm. In order to slow down the whole experiment a very high viscosity silicon oil (Dow Corning 200 Fluid) is used: Compared with most technological applications, a relative low nominal squeezing pressure has been applied. The viscosity of the fluid is $\eta = 100$ Pas while the nominal squeezing pressure is of order 10^4 Pa.

In the experiments below, different configurations are used in order to test different effects on the squeezing out process. Either an elastic silicon rubber block or a rigid glass block is squeezed against a smooth glass substrate or a rough copper surface. The rubber blocks all have the same radius $R = 15$ mm but they differ in height $d = 3$, 5 and 10 mm. The silicon elastomer used is PDMS (Sylgard 184) and it has been prepared as described in Sec. 3.3. The rough copper surfaces were prepared by pressing different sandpaper surfaces against a flat and plastically soft copper surface using a hydraulic press. Variating the grit size and repeating the procedure many times, resulted in some nearly randomly rough surfaces suitable for the experiments. The roughness of the copper surface can be changed by using sandpaper of different maximum grade (consisting of particles with different average diameter).

The experiments have been performed by placing the silicon rubber or the glass block, attached to the dead weight, in the high viscosity fluid with some distance to the rough copper surface or the smooth glass substrate. To avoid trapped air in the fluid it has been poured in the container carefully and degassed in a vacuum chamber for a couple of hours. This is necessary because of the high viscosity of the silicon oil. In order to avoid kinetic effects, due to the inertia of the dead weight, the initial separation is selected to be very small. The normal force is applied by dropping the weight while simultaneously the displacement from the starting position is registered as a function of time.

The surface roughness of the two rough copper surfaces 1 and 2 used in this study has been measured using an optical sensor. The corresponding root-mean-square roughness values are 42 μm and 88 μm. Fig. 5.6 shows the power spectrum of the two rough substrates used in this experiment.

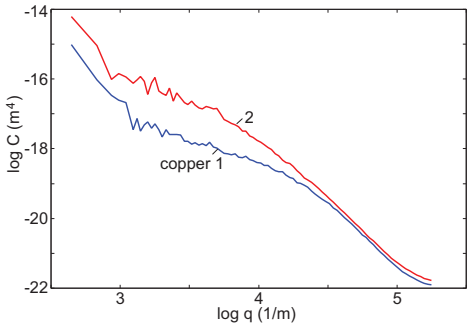

Abbildung 5.6: The surface roughness power spectrum for the two copper surfaces 1 and 2. The root-mean-square roughness of the two surfaces are 42 μm and 88 μm, respectively.

Three different configurations of the experiment have been tested. In the first test, a nominally flat PDMS or glass cylinder is squeezed against a flat glass substrate. This is done in order to test the influence of the non-uniform hydrodynamic pressure on the deformation of the PDMS sample. The squeezing out for the PDMS-glass combination is expected to take longer than for the glass-glass combination, due to the trapped fluid as indicated in Fig. 5.5. This first test is referred to as *PDMS or glass cylinder against flat substrate*. In the second experiment, flat PDMS cylinders with different thickness d are squeezed against the rough copper 1 sample. In the last experiment the flat PDMS cylinder is squeezed against the copper 2 surface.

5.3 Comparison with the Theory Predictions

In this section the experimental data is compared with the calculated squeezing out from the model presented in [55]. All relevant information, such as the surface roughness power spectra as well as the elastic properties of the PDMS, are known.

PDMS or glass cylinder against flat substrate

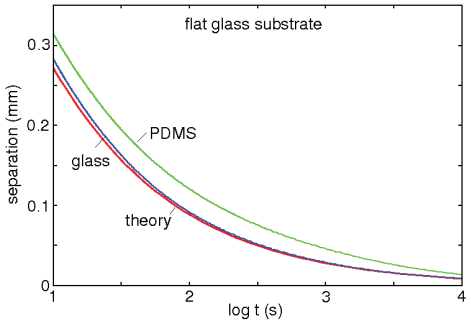

Abbildung 5.7: The surface separation as a function of the logarithm of time when a glass and a PDMS cylindrical block is squeezed against a flat glass substrate in the presence of a high viscosity silicon oil. Also shown is the theoretical prediction (lower curve). The cylindrical body has the height $d = 5$ mm and the diameter $D = 2R = 30$ mm. The normal load $F_N = 13.8$ N and the fluid viscosity $\eta = 100$ Pas.

Fig. 5.7 shows the surface separation as a function of the logarithm of time when a PDMS or a glass cylindrical block is squeezed against a flat glass substrate in the presence of a silicon oil. The lower curve in the figure shows the theoretical predictions neglecting the macroscopic deformation of the block. The cylinder used in this experiment has a thickness $d = 5$ mm and diameter $D = 2R = 30$ mm. The result from the theory agrees almost perfect for the case of a glass cylinder squeezed against a flat substrate. There are no fitting parameters used in the calculation. However for the PDMS block squeezed against a flat substrate, the average separation between the substrate and the PDMS rubber block is larger and the squeezing out occurs slower than predicted by the theory. This discrepancy is attributed to the temporarily trapped fluid resulting from the macroscopic deformation of the PDMS surface before the two solids form contact. This effect is not included in these model calculations but it can be estimated as follows. The trapped fluid volume ΔV is defined as the fluid volume between the bottom surface of the block and a flat surface in contact with the block only at the edge $r = R$. Using the theory of elasticity $\Delta V = \pi R^2 \delta$ with $\delta = CR\bar{p}/E_{\text{eff}}$, where C is a constant of order unity. For the present case ($d = 5$ mm) $E_{\text{eff}} \approx E[1 + 0.5 \cdot (R/2d)^2] \approx 4$ MPa one gets $\delta \approx 40$ μm.

This results in a volume of trapped fluid that can not be neglected and which results in a longer squeezing out time as this additional silicon oil is slowly removed. This assumption is consistent with the experimental observations.

PDMS against the Copper 1 Surface

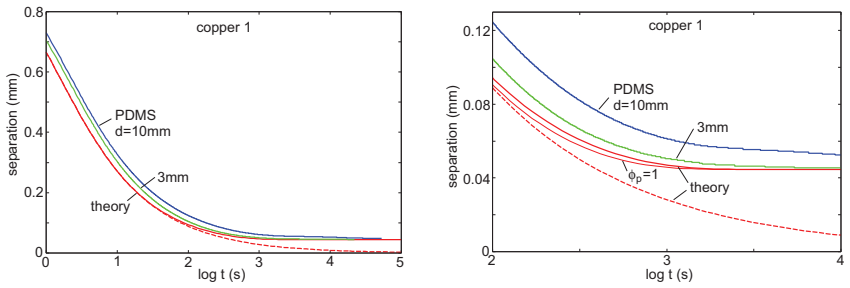

(a) (b)

Abbildung 5.8: (a) shows the surface separation as a function of the logarithm of time when two PDMS cylindrical blocks with the thickness 3 mm and 10 mm are squeezed against the rough copper surface 1 in a silicon oil. Also shown is the theoretical prediction for a flat substrate (dashed curve) and for the copper surface 1 (lower solid line). (b) shows the same as in (a) but for a more narrow time interval. The thin solid line is the calculated squeezing out assuming the pressure flow factor $\phi_p(\bar{u}) = 1$.

Fig. 5.8 (a) and (b) show the surface separation as a function of the logarithm of time when the PDMS cylindrical block is squeezed against the rough copper surface 1 in the presence of a silicon oil. The experiment has been repeated with PDMS samples with thickness 3 mm (green curve) and $d = 10$ mm (blue curve). There is a clear dependance on the squeezing out process due to the thickness of the rubber block. Increasing the thickness of the PDMS block also increases the time it takes for the upper solid to reach its equilibrium position. The reason for this is the effect described in Sec. 5.3 and explained in Sec. 5.1.4. The fluid pressure induced curvature of the bottom surface of the rubber is expected to be smaller for the thin rubber disk.

The dashed line in Fig. 5.8 shows the theory prediction for a flat substrate while the lower (red) solid curve is the calculated squeezing out for the copper 1 substrate. In both cases the bottom surface of the rubber disk is assumed to be macroscopically flat. The agreement between theory and experiment is better for the thinner rubber disk. But even for the thin rubber disk, fluid-pressure induced bending of the bottom surface is expected. This effect is believed to be the main origin for the slightly slower

squeezing out observed in the experiment as compared with the theory.

The thin solid line in Fig. 5.8 (b) shows the calculated squeezing out assuming the pressure flow factor $\phi_p(\bar{u}) = 1$. Here, he pressure flow factor is close to unity and this explains the relative small difference between using $\phi_p(\bar{u}) = 1$ (thin red line) or the calculated $\phi_p(\bar{u})$ (thick red line).

Fig. 5.9 shows the surface separation as a function of the logarithm of time when the PDMS disk, with thickness $d = 5$ mm, is squeezed against a flat glass substrate (lower curve) and against the rough copper surface 1 in a silicon oil. Before contacting the substrate the fluid-pressure induced bending of the bottom surface of the block is the same for both cases. This leads to overlapping curves for $t < 300$ s. This changes when the PDMS block comes into contact with the substrate.

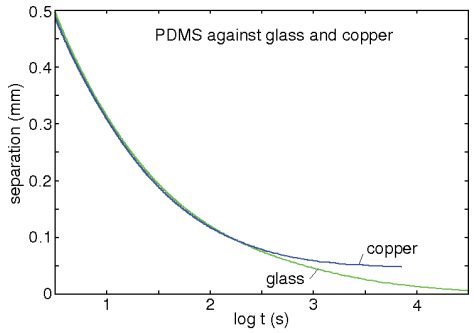

Abbildung 5.9: The surface separation as a function of the logarithm of time when a 5 mm thick PDMS cylindrical block is squeezed against a flat glass substrate (lower curve), and against the rough copper surface 1 in a silicon oil.

PDMS against the Copper 2 Surface

In Fig. 5.10 the surface separation as a function of the logarithm of time is shown when the $d = 5$ mm thick PDMS cylindrical block is squeezed against the rough copper 2 surface. The lower (solid) curve is the theoretical prediction for the squeezing out. The dashed line again represents the case for PDMS against a flat substrate. Note that the experimental data and the theory prediction differ in the beginning. Again, the main reason for this is the macroscopic bending of the lower PDMS surface due to the fluid pressure. Note that increasing the roughness of the substrate tends to result in a faster squeezing out. This is also expected as the leak channels, when the PDMS block has formed contact with the substrate, are much bigger for surface 2 as for surface 1. The qualitative behavior of the system however is not changed and the agreement between the predictions of the theoretical approach by Persson with the experimental information show that the contact is well described

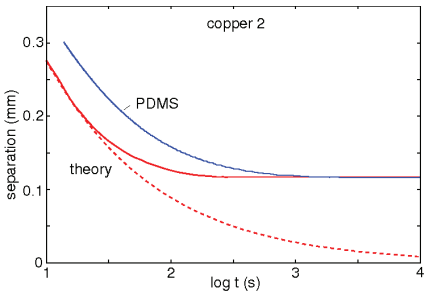

Abbildung 5.10: The surface separation as a function of the logarithm of time when a $d = 5$ mm thick PDMS cylindrical block is squeezed against the rough copper surface 2 in a silicon oil. Also shown is the theoretical prediction (lower solid curve). The dashed curve is the theory prediction for the case of a flat substrate.

by the theory.

5.4 Conclusions to the Squeezing Out

In this section the squeezing out of a fluid from the interface between an elastic block with a flat surface and a randomly rough, rigid solid has been studied. The approach by Persson to calculate the average interfacial separation as a function of time by considering the fluid flow out of the contact has been discussed. The contact mechanics theory of Persson has been used in combination with thin-film hydrodynamics with flow factors which were calculated using a recently developed theory [80]. The importance of the large length-scale elastic deformation on the squeeze-out has been discussed theoretically. An experiment has been designed in order to test this approach and the theoretical results have been compared with the experimental data. In the experiments above, cylindrical rubber blocks with different height d have been squeezed against rough copper surfaces in the presence of a high viscosity silicon oil. Changing the height d of the block and also performing additional experiments, where the flat rubber rubber block is squeezed against a flat substrate, the importance of the large length-scale and the asperity induced elastic deformation on the squeezing out could be probed experimentally. In particular, the large length-scale deformation of the bottom surface of the rubber block resulted in temporary trapped fluid which drastically slowed down the squeezing out. It was shown that this effect is smallest for the thinnest rubber block. Indeed, for this configuration good agreement between theory (which neglects the macroscopic deformation of the elastic body) and experiment is found.

The good agreement between the theory results and the experiment shows that the contact formation is well described using the contact mechanics theory of Persson.

As in Sec. 4.2, where the leakage of a seal is addressed, the application in this section involved both, the **real area of contact** and the **interfacial separation**.

6 Heat Transfer between Rough Surfaces

The heat transfer between two solids with rough surfaces in contact with each other is addressed. The contact mechanics theory of Persson is used to calculate the heat transfer, both via the real area of contact, and from the non-contact regions. A brief introduction to this topic is given in the first part of this chapter. The heat transfer between two elastic solids is derived and the predictions are analyzed. An experimental approach to this topic is presented, and the experimental results are compared with the theory predictions and discussed.

The heat transfer between two solids is a topic of great practical importance and it is closely connected to the nature of the contact between the two solid bodies. Classical applications include matters such as the cooling of heat exchangers, tyres, microelectronic devices, spacecraft structures and nuclear engineering. Heat transfer is also of crucial importance in friction and wear processes, e.g. rubber friction on hard and rough substrates depends crucially on the temperature increase in the rubber-counter surface asperity contact regions [77]. Other potential applications involve the cooling of microelectromechanical systems (MEMS).

A lot of work has been carried out and published on the heat transfer between randomly rough surfaces [3]. However, most of these studies are based on multiasperity contact models such as the Greenwood and Williamson theory (GW). It has been shown above that the GW-model, and other asperity contact models, are rather inaccurate, see Sec. 3.4.2 and [15, 17, 89]. The main reason for this is that the multiasperity contact models neglect long-range elastic coupling between the asperity contact regions [79, 87]. Also, the asperity contact regions are assumed to be circular or elliptical. However, the actual contact regions, observed at high enough resolution, have in fact fractal-like boundary lines, see Fig. 6.1 and [8, 70, 92]. Thus, because of their complex nature, one should avoid to directly involve the nature of the contact regions when studying contact mechanic problems. Note also that for elastically hard solids the area of real (atomic) contact A may be only a very small fraction of the nominal or apparent contact area A_0, even if the nominal squeezing pressures are high [72, 85].

The contact regions between two elastic solids observed at atomic resolution are just a few atoms wide, so that the typical diameter of the contact regions may be of order ~ 1 nm [40, 61, 114]. The heat transfer via such small junctions may be very different from the heat transfer through macroscopic-sized contact regions, where the heat transfer usually is assumed to be proportional to the linear size of the contact regions, rather than the contact area. In particular, if the typical phonon

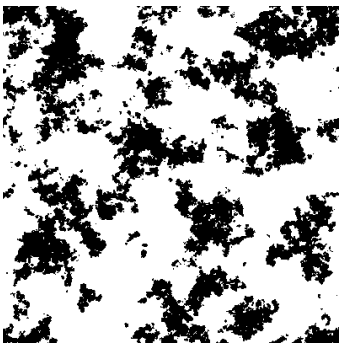

Abbildung 6.1: The black area is the contact between two elastic solids with randomly rough surfaces. For surfaces which have fractal-like roughness the whole way down to atomic length scale, the contact at the highest magnification (atomic resolution) typically consists of nanometer-sized atomic clusters. The result is obtained using Molecular Dynamics (MD), but since there is no natural length scale in elastic continuum mechanics the picture could also be the contact observed between two macroscopic elastic solids. Adopted from [92].

wavelength involved in the heat transfer becomes larger than the linear size of the contact regions, which always happens at low enough temperature, the effective heat transfer may be strongly reduced. Similarly, if the phonon mean free path is longer than the linear size of the contact regions, ballistic phonon energy transfer may occur which cannot be described by the macroscopic heat diffusion equation. These effects are likely to be of crucial importance in many modern applications involving micro- (or nano-) sized objects, such as MEMS, where just a few atomic-sized contact regions may occur. However, for macroscopic solids the thermal (and electrical) contact resistance is usually very insensitive to the nature of the contact regions. In fact, the heat transfer is determined mainly by the nature of the contact regions observed at lower magnifications where it appears to be larger, see Fig. 6.2 and [4, 30].

Recently a novel approach has been presented describing the heat transfer between macroscopic-sized solids using the approach on contact mechanics by Persson [88]. This approach does not directly involve the complex nature of the contact regions. The contribution to the heat transfer from the area of real contact observed at atomic resolution [101, 102, 103] and also the heat transfer across the area of non-contact, in particular the contribution from the fluctuating electromagnetic field which surrounds all solid object, are taken into account [45, 109]. The different heat transfer mechanisms are presented briefly and the necessary information to calculate the total heat transfer are derived from the contact mechanics theory of Persson.

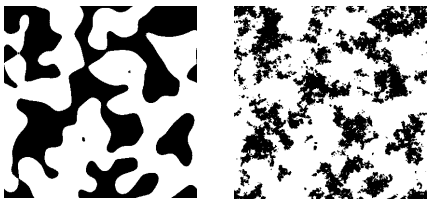

Abbildung 6.2: The contact region (black area) between two elastic solids observed at low (left) and high (right) magnification. The contact resistance depends mainly on the long-wavelength roughness and can usually be calculated accurately from the nature of the contact observed at low magnification (left).

The reader is referred to [88] for a detailed description of the model. In order to test this approach, a simple device was designed and experiments have been carried out.

In this section, it is assumed that the solids deform elastically and that the adhesional interaction between the solids can be neglected. However the contact mechanics theory of Persson can also be applied to cases where adhesion and plastic flow are important.

6.1 The Heat Transfer Model

In most applications one is interested in the heat transfer between solid objects located in the normal atmosphere or in a fluid. Most solid objects in the normal atmosphere have organic and water contamination layers, which may influence the heat transfer for at least two reasons: (a) Thin contamination layers may occur at the interface in the asperity contact regions, which will affect the acoustic impedance of the contact junctions, and hence the propagation of phonons between the solids (which usually is the origin of the heat transfer, at least for most non-metallic systems). (b) In addition, capillary bridges may form in the asperity contact regions and increase the heat transfer. In the normal atmosphere heat can also be transferred between the non-contact regions via heat diffusion or (at short separation) ballistic processes in the surrounding gas. For larger separations convective processes may also be important.

For high-resistivity materials and for hard and very flat surfaces, such as those involved in many modern applications, e.g. MEMS applications, the non-contact radiative heat transfer may in fact dominate in the total heat transfer (at least under vacuum condition). Note that for flat surfaces (in vacuum) separated by a distance d larger than the thermal length $d_{\mathrm{T}} = c\hbar/k_{\mathrm{B}}T$, the non-contact heat transfer is given by the classical Stefan-Boltzmann law, and is independent of d. However, for very short distances the contribution from the evanescent electromagnetic waves to the heat transfer will be many orders of magnitude larger than the contribution from

propagating electromagnetic waves.

As mentioned above, the heat transfer is mainly determined by the nature of the contact regions observed at low magnification. It can be shown that for self-affine fractal surfaces, the contact resistance depends on the range of surface roughness included in the analysis as $\sim r(H) - (q_0/q_1)^H$, where q_0 and q_1 are the smallest and the largest wave vector of the surface roughness included in the analysis. The number $r(H)$ depends on the Hurst exponent H but is of order unity. In a typical case $H \approx 0.8$, and including surface roughness over only one wave vector decade $q_0 < q < q_1 = 10q_0$ results in a heat resistance which typically is only ~ 10 % smaller that obtained when infinitely many decades of length scales are included. At the same time, for elastic solids, the area of real contact approaches zero as $q_0/q_1 \to 0$. Thus, there is in general no relation between the area of real contact (which is observed at the highest magnification, and which determines, e.g. the friction force in most cases), and the heat (or electrical) contact resistance between the solids.

In the context of electric conduction, one aspect of this was pointed out a long time ago: if an insulating film covers the solids in the area of real contact, and if electrical contact occurs by a large number of small breaks in the film, the resistance may be almost as low as with no film at all [2]. Similarly, the thermal contact resistance of macroscopic solids usually does not depend on wether the heat transfer occurs by diffusive or ballistic phonon propagation, but rather by the nature of the contact regions observed at relative low, magnification.

6.1.1 Heat Transfer Coefficient

Consider two elastic solids (rectangular blocks) with randomly rough surfaces that are squeezed into contact as illustrated in Fig. 6.3. Assuming that the temperature at the outer surfaces $z = -d_0$ and $z = d_1$ is kept fixed at T_0 and T_1, respectively, with $T_0 > T_1$. Close to the interface the heat current will vary rapidly in space, $\mathbf{J} = \mathbf{J}(\mathbf{x}, z)$, where $\mathbf{x} = (x, y)$ denote the lateral coordinate in the xy-plane. Far from the interface the heat current should be constant and in the z-direction, i.e., $\mathbf{J} = J_0\hat{z}$. The average distance between the macro asperity contact regions is denoted by λ (see [76]). It is assumed that $\lambda << L$, where L is the linear size of the apparent contact between the elastic blocks. The temperature a distance $\sim \lambda$ from the contacting interface is approximately independent of the lateral coordinate $\mathbf{x} = (x, y)$ and these temperatures are introduced as T_0' and T_1' for $z = -\lambda$ and $z = \lambda$, respectively. The heat current for $|z| >> \lambda$ is independent of $\mathbf{x}$ and can be written as (to zero order in λ/d_0 and λ/d_1)

$$J_0 = -\kappa_0 \frac{T_0' - T_0}{d_0} = -\kappa_1 \frac{T_1 - T_1'}{d_1} \tag{6.1}$$

where κ_0 and κ_1 are the heat conductivities of the two solid blocks. It is further assumed that the heat transfer across the interface is proportional to $T_1' - T_1'$ and the heat transfer coefficient is defined as α so that

$$J_0 = \alpha(T_0' - T_1') \tag{6.2}$$

Combining Eq. (6.1) with (6.2) gives

$$J_0 = \frac{T_0 - T_1}{d_0\kappa_0^{-1} + d_1\kappa_1^{-1} + \alpha^{-1}} \tag{6.3}$$

This equation is valid as long as $\lambda << L$ and $\lambda << d_0$ and d_1. Note that α depends on the macroscopic (or normal) pressure acting at the interface. Thus if the macroscopic pressure is non-uniform, as it may be the case in many practical applications (e.g. when a ball is squeezed against a flat substrate), one needs to include the dependency of α on $\mathbf{x}$. Thus in general one has to write

$$J(\mathbf{x}) = \alpha(\mathbf{x})\left[T_0'(\mathbf{x}) - T_1'(\mathbf{x})\right] \tag{6.4}$$

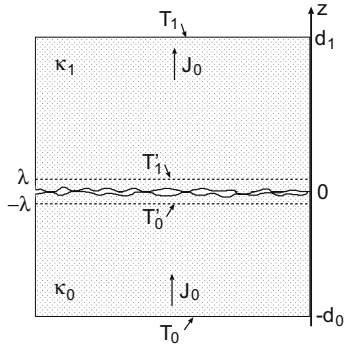

Abbildung 6.3: Two elastic solids with nominally flat surfaces squeezed together with the nominal pressure p_0. The heat current $J_z(\mathbf{x})$ at the contacting interface varies strongly with the coordinate $\mathbf{x} = (x, y)$ in the xy-plane. The average heat current is denoted by $J_0 = \langle J_z(\mathbf{x})\rangle$.

Assume now for simplicity that the two solids are made of the same material so that one expects the contribution to α from the area of real contact to be proportional to the heat conductivity κ. Assuming only elastic deformation, contact mechanics theories show that for low enough squeezing pressures p_0, the area of real contact is proportional to p_0, and the size distribution of contact regions (and the interfacial stress probability distribution) are independent of p_0. Thus one can expect that α is also proportional to p_0. For randomly rough surfaces the contact mechanics depend only on the (effective) elastic modulus E^* and on the surface roughness power spectrum $C(q)$. The only way to construct a quantity which is proportional to $p_0\kappa$ and with the same dimension as $J_0/\Delta T$, using the quantities which characterize the problem, is

$$\alpha \approx \frac{p_0 \kappa}{E^* u_0} \tag{6.5}$$

where u_0 is a length parameter which is determined from the surface roughness power spectrum $C(q)$. For self-affine fractal surfaces, $C(q)$ depends only on the root-mean-square roughness h_{rms}, the fractal dimension D_{f} which is dimension less, and on the low and high cut-off wavevectors q_0 and q_1. Thus in this case $u_0 = h_{\mathrm{rms}} f(D_{\mathrm{f}}, q_0/q_1, q_0 h_{\mathrm{rms}})$. This result is consistent with the analysis presented in Sec. 2.2.1 in [88]. Using the GW theory also results in an expression for α of the form given above, but with a different function f which now (even for low squeezing pressures) also depends on p_0/E^* (see for a complete description [93]).

6.2 The Experimental Method

In order to test the approach towards heat transfer between randomly rough surfaces based on the contact mechanics theory of Persson, the following experiment has been performed. The instrument is schematically shown in Fig. 6.4. It consists of two containers which are both filled with distilled water. They are standing on each other with a thin silicon rubber film separating them. The upper container is made from copper with an inner diameter of 50 mm. The water is heated to boiling temperature so that $T_0 = 100°$ C. The lower container is made from PMMA with a cylindrical copper block at the top. To study the effect of surface roughness on the heat transfer, this copper block can be replaced by other blocks with different surface roughness. For the experiment reported on below, four different copper blocks with different surface properties were used. In both containers, the water gets mixed in order to obtain a uniform water temperature and to enhance the heat transfer from the water to the copper surfaces. Therefore magnetic-driven, rotating metal bars are used.

The temperature of the water in the lower container increases with time t due to the heat current J_0 flowing from the upper container via the interface of the rubber sheet and the rough copper sample to the water in the lower container. Neglecting the heat transfer to the surrounding from the lower container, energy conservation gives

$$J_0 = \rho C_{\mathrm{V}} \dot{T}_1 d \tag{6.6}$$

Here d is the height of the water column in the lower container (in this configuration $d = 35$ mm), ρ is the water mass density and C_{V} is the heat capacity of water. In the experiment the temperature rise of the water in the lower container, due to the heat transfer, is detected starting at 25° C.

The heat transfer has been investigated using copper blocks with different surface roughness. These samples were prepared as described in Sec. 5.2. Plastically soft copper blocks with smooth surfaces have been pressed against different sandpaper surfaces using a hydraulic press. This procedure has been repeated several times

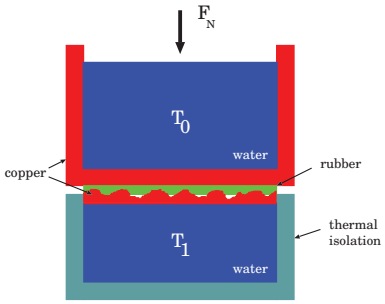

Abbildung 6.4: The experimental device to test the theory predictions for the heat transfer across the interface. The time dependent increase in the temperature $T_1(t)$ of the water in the lower container determines the heat transfer between the upper and the lower water container.

in order to obtain surfaces with randomly roughness properties. Due to surface roughness, the contact between the top surface of the lower container and the thin silicon rubber sheet (diameter 50 mm, thickness $d_0 = 2.5$ mm), attached to the upper container, is only partial. Fig. 6.5 shows the corresponding surface roughness power spectra of the copper surfaces used. They are denoted as surface 1, 2 and 3 with rms roughness 42, 88 and 114 μm respectively. A fourth surface was used which has been highly polished so that the surface appears to be very smooth. It is denoted surface 0 and its measured rms roughness is 64 nm.

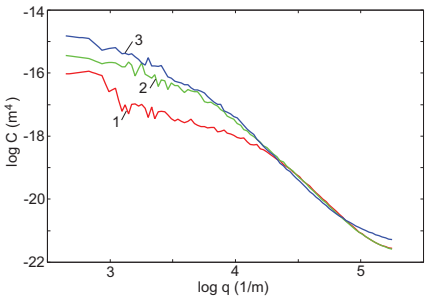

Abbildung 6.5: The surface roughness power spectrum of the three copper surfaces used in the experiment. The surfaces 1, 2 and 3 have the root-mean-square roughness 42, 88 and 114 μm, respectively.

The bottom surface of the upper container has been highly polished so that the resistance to the heat flow at this rubber-copper interface can be neglected. Compared with the resistance to the heat flow arising from the heat diffusion through

the rubber sheet and also at the interface between the rubber and the rough copper block, this assumption is fairly accurate. As in all the experiments before, the rubber sheet used is made from PDMS (Sylgard 184). Because of its purely elastic behavior (on the time scales involved in this experiment) this is a good model rubber where the increase of real area of contact due to creep motion of the rubber film can be neglected. The elastic modulus measured for the rubber is $E = 2.5$ MPa (Poisson's ratio $\nu = 0.5$).

6.3 Numerical Calculations and Results

As in Eq. (6.3) one can write for the heat flow of the system described before

$$J_0 \approx \frac{T_0 - T_1(t)}{d_0 \kappa_0^{-1} + \alpha^{-1}} \tag{6.7}$$

where κ_0 is the heat conductivity of the rubber. The resistance to the heat transfer from the copper blocks is neglected because of the high thermal conductivity of copper. Combining Eq. (6.6) with (6.7) leads to

$$\tau_0 \dot{T}_1 = T_0 - T_1(t) \tag{6.8}$$

where τ_0 is the relaxation time

$$\tau_0 = \rho C_\mathrm{v} d \left(\frac{d_0}{\kappa_0} + \frac{1}{\alpha} \right) \tag{6.9}$$

Assuming that the relaxation time is time independent gives

$$T_1(t) = T_0 + [T_1(0) - T_0] e^{-t/\tau_0} \tag{6.10}$$

It is further assumed that there is no heat transfer from the lower container to the surrounding. This should be a good approximation because of the rather low temperature difference and the good isolation of the container.

The heat transfer across the rubber-copper interface can have three different causes. It can occur via the area of real contact through direct contact, via heat diffusion in the thin air film in the non-contact area, or via radiative heat transfer. All these heat transfer processes act in parallel, so that on needs to take all of them into account.

$$\alpha \approx \alpha_\mathrm{con} + \alpha_\mathrm{gas} + \alpha_\mathrm{rad} \tag{6.11}$$

The different contributions are now estimated for the given experimental configuration. Assuming a nominal pressure of $p_0 \approx 0.01$ MPa, $E^* \approx 2$ MPa, $u_0 \approx 10$ μm and the heat conductivity for rubber $\kappa_0 = 0.2$ WmK (neglecting the heat conductivity of copper κ_1 because it is much higher than for rubber) gives

$$\alpha_\mathrm{con} = \frac{p_0 \kappa_0}{E^* u_0} \approx 100 \ \mathrm{W/m^2K} \tag{6.12}$$

Using the diffusive heat conductivity of air $\kappa_{\rm gas} \approx 0.02$ W/mK and assuming that the average of the inverse of the interfacial separation $\langle d^{-1} \rangle = (20\ \mu{\rm m})^{-1}$ gives

$$\alpha_{\rm gas} = \kappa_{\rm gas} \langle (d + \Lambda)^{-1} \rangle \approx \kappa_{\rm gas} \langle d^{-1} \rangle \approx 1000\ {\rm W/m^2K} \tag{6.13}$$

Finally, assuming that the radiative heat transfer is well approximated by the Stefan-Boltzmann law and that $(T_0 - T_1)/T_1 << 1$, while $T_0 = 373$ K, one can calculate

$$\alpha_{\rm rad} \approx \frac{\pi^2 k_B^4}{60 h^3 c^2} 4 T_0^3 \approx 10\ {\rm W/m^2K} \tag{6.14}$$

The thickness of the silicon rubber film is $d_0 = 2.5$ mm so that $d_0^{-1}\kappa_0 \approx 100$ W/m^{2}K This finally gives

$$\frac{1}{d_0^{-1}\kappa_0} + \frac{1}{\alpha} \approx \left(\frac{1}{100} + \frac{1}{100 + 1000 + 10} \right)\ ({\rm W/m^2K})^{-1} \tag{6.15}$$

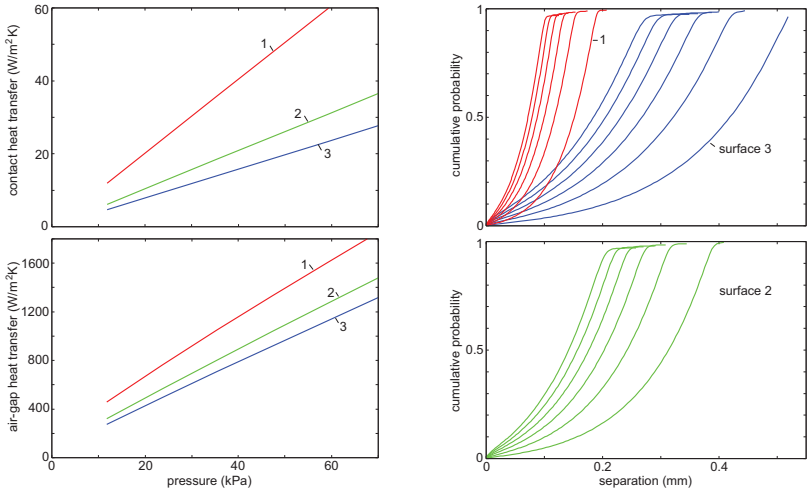

Abbildung 6.6: Theory results for the surfaces 1, 2 and 3. (a) the variation of the heat transfer coefficient from the real area of contact, $\alpha_{\rm con}$, and the diffusion via the air-gap, $\alpha_{\rm gas}$, as a function of the squeezing pressure. (b) the variation of the cumulative probability of the interfacial separation u for the squeezing pressures 11.8, 23.7, 35.5, 47.3, 59.2, and 71.9 kPa (from left to right).

This shows that in the present case the thin rubber film gives the dominant contribution to the heat resistance. However it is not possible to use a thinner film neither to change the rubber material. The reasons are that a thinner film will would no longer behave as an elastic half space and therefore the contact mechanics would be changed. Changing the material also doesn't help because of the small variation in heat conductivity between different rubber materials. Choosing a different rubber one would also loose the perfect elastic response properties of the PDMS. However, the experimental results reported on below should give some indication about how good the theory works.

Before comparing the experimental results to the theory predictions, some calculated results are shown. Fig. 6.6 (a) shows the pressure dependence of the contact heat transfer coefficient, α_{con} (upper figure), and the air-gap heat transfer coefficient, α_{gas} (lower figure), for the surfaces 1, 2 and 3. Increasing the normal pressure results in an increase of the area of real contact. For low squeezing pressures, the relation between A and p_0 is linear so that the contact heat transfer is proportional to p_0. The lower figure shows that α_{gas} also varies nearly linear with p_0. At first sight this appears remarkable because it has been shown in Sec. 3.1 that the average surface separation $\bar{u}$ depends logarithmical on the applied pressure. However, the heat transfer via heat diffusion in the air gap depends on $\langle (u + \Lambda)^{-1} \rangle$. This expression depends almost linear on p_0 as long as $\bar{u} >> \Lambda$ and this is true in the presented configuration.

From Fig. 6.6 (a) it can be concluded that in this experiment mainly the theory for the heat flow in the air gap has been tested. The reason for this is that $\alpha_{\text{gas}} >> \alpha_{\text{con}}$. Fig. 6.6 (b) shows the variation of the cumulative probability of the interfacial separation u as a function of the normal pressure p_0 for the surfaces 1 and 3 (top) and 2 (bottom). The squeezing pressure is increased stepwise resulting in decreasing interfacial separations (from left to right).

6.4 Comparison to Experimental Data

Fig. 6.7 shows the measured temperature (dots) in the lower container as a function of time. The results are for all copper surfaces used and for the normal squeezing pressure $p_0 = 0.012$ MPa. The solid lines in Fig. 6.7 are the predictions of the theoretical approach, using the contact mechanics theory of Persson for the four given configurations. Each experiment has been repeated several times and all the measured information are plotted in Fig. 6.7. Changing the surface roughness properties clearly leads to a difference in the resistance to the heat flow. Increasing the roughness more and more also increases the time it takes to heat the water in the lower container. However the heat transfer of the different configurations does not vary too much. This can, as already mentioned above, be attributed to the dominating heat resistance of the thin rubber film (because of the low heat conductivity κ_0). For direct metal-metal contact the contact resistance would be much more important. However, for very rough metallic surfaces it is likely that plastic flow of the me-

tals could be already observed at low magnifications which would affect the contact resistance as well.

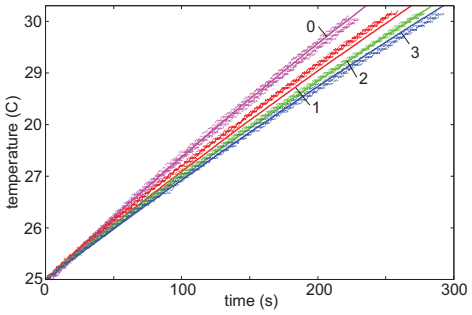

Abbildung 6.7: The measured temperature increase (dots) in the lower container as a function of time. Also shown as solid lines, the calculated temperature increase. Results are for all four surfaces. The applied, nominal squeezing pressure is $p_0 = 0.012$ MPa.

An additional experiment has been performed to test the dependency of the heat transfer on the squeezing pressure p_0. The experiment was performed with the copper surface 2 for two different squeezing pressures $p_0 = 0.012$ MPa and 0.071 MPa. Fig. 6.8 shows the measured temperature (dots) in the lower container and the calculated temperature (solid lines) as a function of time.

In the analysis discussed above there are no fitting parameter involved. The heat transfer model is based on the contact mechanics approach by Persson taking into account the heat transfer via the real area of contact and via the non-contact regions.

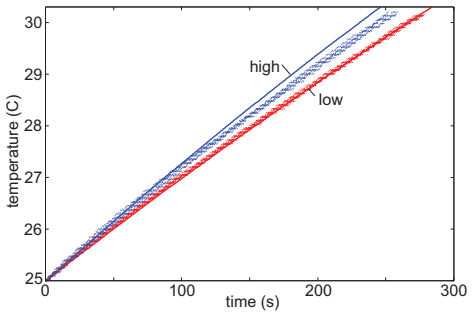

Abbildung 6.8: The same as in Fig. 6.7 but for the two different squeezing pressures $p_0 = 0.012$ (lower curve) and 0.071 MPa (upper curve). The substrate used for this test was the copper 2 surface.

As in Sec. 4.2, this application was also useful to test the predictions of the contact mechanics theory of Persson as the heat transfer model needs important information such as the **area of real contact** and the **interfacial separation**. The agreement between theory and experiment is relatively good taking into account the problems described before. In order to obtain better experimental information two different configurations could be considered. One would be to use two metal surfaces to avoid the high resistance of the rubber film, as suggested above. It would also be interesting to repeat the experiment under vacuum conditions. For this case, half of the heat transfer resistance would arise from the thin rubber film while the other half comes from the area of real contact. This would make it easier to study the influence of the latter contribution.

To summarize, it was shown that the theory of Persson could be successfully applied to the problem of heat transfer between two elastic solids with randomly rough surfaces. The theory results agree very well with the experimental data. This gives additional support that the contact mechanics theory of Persson describes the contact formation correctly.

7 Rubber Friction

Different energy dissipation mechanisms relevant for rubber friction are discussed. A theoretical approach, based on the contact mechanics theory reported on above, is presented. A new instrument to measure the friction between a rubber block and a rough substrates is described and the theory predictions are compared with experimental results for filled and unfilled SB rubber sliding on concrete surfaces.

The friction of rubber sliding on a hard and randomly rough substrate is a matter of great interest and relevance for many practical applications [24, 29, 35, 36, 48, 62, 67, 71, 81, 82, 110]. For most technical systems the friction should be as small as possible in order to improve the efficiency of a technical system, e.g. for rubber seals, wiper blades or syringes. A rubber-counter surface combination that has not been optimized during the design process may lead to a bad energy efficiency and usually also to higher wear. In addition, stick-slip may occur which can perturb the primary function of the machine. However there are also several technical systems were rubber friction is required to be as high as possible. This is the case for a car tyre during braking or high speed cornering.

Despite of its importance, there did not exist any good, physical model to calculate rubber friction until recently. The design of a tyre for instance is still based mainly on experience and experimental information. To simulate vehicle dynamics, the tyre body is modeled in great detail using powerful finite element methods. However, following the very first idea of Amonton and Coulomb, friction is often modeled using only two parameters, namely a *static* coefficient of friction (μ_{static}) and a *kinetic* coefficient of friction (μ_{dynamic}). It is then assumed that static friction occurs between a rubber solid and a counter surface when there is no relative motion. To accelerate the rubber solid, the static friction needs to be overcome and, when the two solids are in relative motion to each other, the kinetic friction prevails. It is usually assumed that $\mu_{\text{static}} > \mu_{\text{dynamic}}$ and that μ_{dynamic} is independent from the sliding velocity.

However, it has been found that rubber friction is not independent of the sliding velocity. Grosch showed experimentally already in 1963 a strong velocity dependance of rubber friction [33]. Thus modeling the frictional interaction between the rubber and the counter surface by using only two simple parameters is not enough to describe, e.g., tyre dynamics, so that this simple approach has turned out to be the bottleneck for most state-of-the-art tyre models. Employing a physical model to calculate the rubber friction would be a major improvement for most simulations. The reason why there does not exist any reasonable model for rubber friction can be

lead back to contact mechanics. Understanding the friction between a rubber block and a hard and rough substrate requires a deep insight into the contact formation of the two solids. The different energy dissipation mechanisms discussed below need information about the **area of real contact**, the **size of the contact spots** and the **viscoelastic deformations**. Until recently there did not exist any good contact mechanics model, so that rubber friction remained an unsolved problem in physics.

In the first part of this thesis a new contact mechanics theory has been tested. Very good agreement has been found between the experimental data and the predictions of the contact mechanics theory of Persson. Within this last section an experimental analysis of the rubber friction approach by Persson based on his contact mechanics theory is presented.

7.1 Introduction to Rubber Friction

Measuring the friction of rubber-like materials, it is observed that the coefficient of friction increases with the sliding velocity until a maximum is reached, after which it decreases again. Generally speaking, friction is a function of the sliding velocity. There are at least four different contributions to rubber friction:

Adhesion: In the regions where the rubber is in contact with the substrate, the polymer chains bind to the atoms of the substrate due to, e.g. attractive van der Waals interactions. When the rubber is in relative motion to the substrate, these chains are elongated until the stress gets too large and the chain break off from the substrate. The elongated chains then rearrange to a state where its energy is minimized. The elastic energy stored in the chains is dissipated resulting in a shear force which is proportional to the real area of contact. It is believed that this mechanism is of importance for rubber sliding on clean and relatively smooth surfaces, e.g. glass.

Hysteresis: When rubber slides on a hard and rough surface, the asperities of the substrate exerts oscillating forces on the rubber surface leading to cyclic deformations of the rubber. Elastic energy is constantly stored and released resulting in a continuous rearrangement of the polymer chains. This is in fact a viscoelastic process and energy is lost due to internal damping in the rubber bulk. Hysteretic dissipation may be the dominant mechanism for rubber friction on rough surfaces, e.g. road surfaces [39, 74, 83].

Viscous damping: If there is a fluid in between the two solids, this fluid layer gets sheared and the viscosity of the fluid results in a friction force which is proportional to the sliding velocity (assuming constant film thickness and Newtonian viscosity). If surface roughness occurs and the velocity is small enough, the rubber comes into partial contact with the substrate. This is referred to as the "mixed lubrication" regime. The relation between friction force and velocity is known as the "Stribeck curve".

Cohesion: During sliding the rubber may wear and small rubber particles are formed by crack propagation. In this process energy is used to break rubber bonds and to form new interfaces resulting in a contribution to the friction force [19, 37, 59, 64, 84, 90, 99].

Grosch showed with his experiments in 1963 that rubber friction is in many cases directly related to the internal hysteresis of the rubber (bulk contribution) [33]. Thus, rubber samples sliding on silicon carbide paper and glass surfaces gave the same temperature dependance of the friction coefficient as that of the complex elastic modulus $E(\omega)$ of the rubber. It has therefore been concluded by Persson and others that rubber friction is mainly due to internal hysteresis in the rubber bulk.

The complex elastic modulus $E(\omega)$ is used to characterize the viscoelastic properties of polymers. It relates the stress ($\epsilon = \epsilon_0 \sin(\omega t)$) to the strain ($\sigma = \sigma_0 \sin(\omega t + \delta)$) of a material as a function of an excitation frequency ω. Viscoelastic materials usually have a phase difference δ between stress and strain resulting from internal energy dissipation. The complex elastic modulus is described as

$$E(\omega) = E' + iE'' \tag{7.1}$$

where the storage modulus $E' = (\sigma_0/\epsilon_0)\cos\delta$ and the loss modulus $E'' = (\sigma_0/\epsilon_0)\sin\delta$.

Persson has developed a theory to calculate rubber friction for a rubber block sliding on a hard and rough surface with roughness on many different length scales. This theory takes into account the energy dissipation due to hysteresis as well as the contribution due to crack opening. In the following sections this theory approach is briefly described and then compared with the results of a rubber friction experiment that has been performed in order to test this theory.

7.2 Rubber Friction on Surfaces with Isotropic Statistical Properties

7.2.1 Approach on Rubber Friction by Persson

In this section the basic equations used to calculate the contribution of the different energy dissipation mechanisms to rubber friction are presented and discussed.

Process (a) - Asperity-Induced Bulk Energy Dissipation

Here the energy dissipation from the viscoelastic deformations of the rubber surface by the roughness asperities of the substrate is considered. A rigid asperity sliding against a flat rubber surface gives rise to time dependent deformation of the rubber which is characterized by the frequency $\omega = v/d$, where d is the linear size of the contact region. The viscoelastic deformation, and also most of the energy dissipation, extends into the rubber by the typical distance d. It follows, that a large fraction of the energy dissipation occurs in a volume element of order d^3. If the perturbing frequency ω is close to the frequency ω^* where $\tan\delta = \mathrm{Im}E(\omega)/\mathrm{Re}E(\omega)$ is maximal,

the contribution of the asperity-induced friction is large, see ω_1 in Fig. 7.2. If ω is far away from ω^* the hysteresis due to bulk energy dissipation is small, see ω_0 in Fig. 7.2.

As already discussed before, the contact between the rubber and the substrate does not happen on only one length scale, but over many decades of length scales. Real surfaces have a wide distribution of asperity contact sizes which can be illustrated best as big asperities on top of which occur smaller asperities on top of which occur even smaller asperities and so on. This is illustrated in Fig. 7.1 for a system where roughness occurs on two length scales. To get the total energy dissipation one needs to take into account the time dependent deformations of the rubber on all relevant length scales. This leads to a wide range of perturbing frequencies, say from ω_0 to ω_1. In order to have high rubber friction, this interval is required to be as close as possible to ω^* where $\tan\delta$ is maximal. The contribution of each frequency has to be summed up to obtain the total contribution of the asperity-induced bulk energy dissipation.

It is important to include all length scales in the analysis because they may all be of equal importance. For example, a short wavelength roughness component with wavelength λ_1 and amplitude h_1 can give the same contribution as a long wavelength component with λ_0 and h_0 if the ratio $h_1/\lambda_1 = h_0/\lambda_0$, see [74].

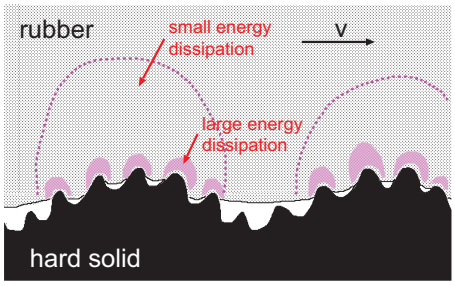

Abbildung 7.1: Viscoelastic deformation of the rubber due to surface roughness asperities of the substrate on two different length scales. The dissipated energy per unit volume is largest in the small asperity contact regions.

Temperature has a crucial influence on the viscoelastic modulus of the rubber material that has to be taken into account. Usually $\tan\delta$ is influenced strongly by temperature so that an increase of 10° C of the rubber may shift the whole $\tan\delta$ curve by one decade in frequency to higher frequencies. As illustrated in Fig. 7.2, increasing the temperature from T_0 to T_1, the $\tan\delta$ curve is much smaller for the frequency range from ω_0 to ω_1. Therefore the rubber friction due to bulk energy dissipation becomes smaller at higher temperatures.

The viscoelastic energy dissipation in the rubber bulk results in local heating of

the rubber in exactly that region where the dissipation occurs. This leads to a local temperature increase (in time and space) which becomes larger and larger when smaller and smaller asperity contact regions are considered. The effect has been described theoretically in [77] where it is referred to as the flash temperature. This effect is of huge importance because of the strong temperature dependance of the viscoelastic modulus. However, for sliding velocities $v < 0.001$ m/s the produced heat has enough time to diffuse away from the contact regions so that the frictional heating can be neglected. For sliding velocities above ≈ 0.001 m/s it has been shown that rubber friction depends on the history of the sliding motion, which is crucial for an accurate description [77]. This history dependance is mainly due to frictional heating in the rubber-substrate contact regions. Many experimental observations, e.g. an apparent dependence of the friction on the normal stress, can in fact be attributed to the impact of frictional heating.

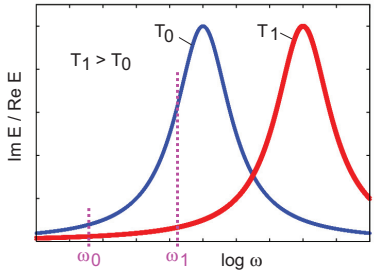

Abbildung 7.2: The tanδ curve for two different temperature $T_0 < T_1$. Increasing the temperature shifts the curve to higher frequencies. Also shown is the interval of perturbing frequencies on the rubber from ω_0 to ω_1. Increasing the temperature of the rubber usually leads to a decrease of the asperity-induced bulk energy dissipation.

Only the surface roughness components with wavevectors $q < q_1$ are included in the rubber friction theory of Persson. The reason for this is that on clean road surfaces, the stresses (and the local temperature) in the asperity contact regions for wavevectors larger than the cut-off wavevector q_1 gets so high that the rubber material starts to yield (rubber bonds break). This results in a thin modified layer of rubber at the surface regions with a thickness of order $1/q_1$. If the rough substrate is contaminated, e.g. because of sand particles, the cut-off q_1 may be determined by the nature of this contamination particles. The cut-off length $1/q_1$ depends in general on the rubber compound used as well as on the nature of the substrate roughness. Changing the substrate results in a run-in process of the rubber in order to form a new modified surface layer at the rubber interface corresponding to a new cut-off length.

Based on the idea presented above, Persson has derived a set of equations des-

cribing the friction acting on a rubber block squeezed with the stress σ_0 against a randomly rough surface. The equations to calculate the frictional shear stress $\mu\sigma_0$ can be summarized as follows

$$\mu = \frac{1}{2}\int_{q_L}^{q_1} \mathrm{d}q\ q^3 C(q) P(q) \int_0^{2\pi} \mathrm{d}\phi\ \cos\phi\ \mathrm{Im}\frac{E(qv\ \cos\phi)}{(1-\nu^2)\sigma_0} \tag{7.2}$$

The function $P(q)$ is defined as

$$P(q) = \frac{2}{\pi}\int_0^{\infty} \mathrm{d}x\ \frac{\sin x}{x}\ \exp(-x^2 G) = \mathrm{erf}\left(\frac{1}{2\sqrt{G}}\right) \tag{7.3}$$

where

$$G(q) = \frac{1}{8}\int_{q_L}^{q} \mathrm{d}q\ q^3\ C(q) \int_0^{2\pi} \mathrm{d}\phi\ \left|\frac{E(qv\ \cos\phi}{1-\nu^2\sigma_0}\right|^2 \tag{7.4}$$

The normalized contact area is given by $A/A_0 = P(q_1)$

Process (b) - Energy Dissipation at the Opening Crack

The strength of adhesion and cohesion of elastomers can be described by the amount of energy G needed to advance a crack tip by one unit area. It has been shown experimentally that G depends on the crack tip velocity v and on the temperature T [27, 28, 60] so that

$$G(v,T) = G_0[1 + f(v,T)] \tag{7.5}$$

For interfacial crack propagation the measured value of G at low crack velocities, neglecting viscous effects in the rubber, is of order ≈ 0.1 J/m^2. This is denoted as G_0, representing the energy to break the interfacial rubber-substrate bonds at the crack tip in the so called crack-tip process zone which are usually of van der Waals type. The temperature dependance of the energy dissipation for simple hydrocarbon elastomers can be completely accounted for by simply multiplying the crack velocity v with a factor a_T so that $f(v,T) = f(a_T v)$. This factor has in fact been found to be equal to the WLF function [111]. This proves that the large influence of the crack velocity and temperature on the crack propagation in rubber materials is due to viscoelastic processes, depending on $E(\omega)$, in the rubber bulk. This involves highly non-linear processes which are difficult to describe theoretically. Until recently G_0 could only be estimated directly from experimental data. In [84, 86] it has been shown how to calculate $f(v,T)$ which may enhance G by a factor of 10^3 or more for high crack tip velocities:

$$G(v) = G_0\left[1 - \frac{2}{\pi}E_0\int_0^{2\pi v/a} \mathrm{d}\omega\ \frac{F(\omega)}{\omega}\ \mathrm{Im}\frac{1}{E(\omega)}\right]^{-1} \tag{7.6}$$

where $E_0 = E(0)$ and where

$$F(\omega) = \left[1 - \left(\frac{\omega\alpha}{2\pi v}\right)^2\right]^{1/2} \tag{7.7}$$

Here a is the crack tip radius which also depends on the crack velocity v. How to calculate this quantity is described in [86].

The effective frictional stress acting in the area of real contact derived from the energy dissipation at the opening crack is called σ_f. With A being the real area of contact, the dissipated energy for sliding a distance $\mathrm{d}x$ is

$$\sigma_\mathrm{f} A \mathrm{d}x = G(v) N l \mathrm{d}x \tag{7.8}$$

where it is assumed that the contact area consists of N regions of linear size l. Thus $Nl\mathrm{d}x$ is the surface area covered by the crack during sliding a distance $\mathrm{d}x$. Since $A = Nl^2$ it can be deduced

$$\sigma_\mathrm{f} = G(v)/l \tag{7.9}$$

Process (c) - Energy Dissipation by Shearing of a Thin, Viscous Film

Many fluids undergo shear thinning at relative low shear rates. The viscosity is often well approximated by

$$\eta(u, v) \approx \frac{\eta_0}{1 + (\eta_0/B)\dot{\gamma}^n} \tag{7.10}$$

where η_0 is the viscosity at low shear rates, whereas $\dot{\gamma} = v/u$ is the shear rate and u the film thickness. At low shear rates, where the fluid viscosity is constant, the orientations of the fluid molecules are random. At higher shear rates, the molecules start to orientate along the flow direction. This effect is called shear thinning. A similar effect is the confinement of the molecules between two closely spaced walls. Here the molecules tend to form layers parallel to the solid walls. Eq. (7.10) is also valid if the thickness of the confined layers is of order nanometer but because of the large shear rate, Eq. (7.10) then takes the form

$$\eta(u, v) \approx B\dot{\gamma}^{-n} \tag{7.11}$$

giving the shear stress

$$\sigma_\mathrm{f} = \eta\dot{\gamma} \approx B\dot{\gamma}^{\alpha} \tag{7.12}$$

where the exponent $\alpha = 1 - n$ is $\alpha \approx 0.1$ while $B \approx 8.9 \cdot 10^4$ when σ_f and $\dot{\gamma}$ are in SI units [112].

7.3 Experimental Investigations on Rubber Friction

To test the rubber friction theory, a couple of experiments have been performed. The first experiment was kept as simple as possible to test if the considered experimental method is applicable and how good the repeatability of the experiment is. After this first approach, a novel instrument has been designed to measure rubber friction for different systems based on the know-how gained with this first experiment.

Because rubber friction is strongly dependent on many parameters, the experiment was designed to be as basic as possible. A too complex test would lead to a situation where the results are influenced by too many parameters. It is then very difficult to analyze the measured data and to validate any theoretical approach.

7.3.1 A Simple Experimental Approach to Rubber Friction

A rubber block with a smooth surface is attached to a steel plate and brought into contact with a hard and randomly rough counter surface (see Fig. 7.3). A normal force F_N is applied by adding a dead weight on top of the steel plate. Similar to the first classic "sliding sled" studies by Leonardo da Vinci, the rubber block is pulled over the rough substrate by a constant force F. This is done by coupling a dead weight with the steel plate using a thin cord and a deflection roller.

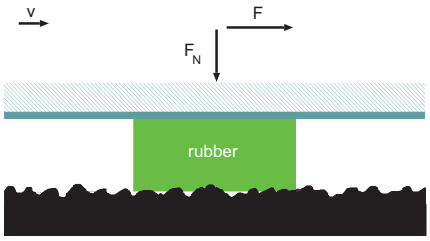

Abbildung 7.3: A rubber block squeezed into contact with a rough counter surface by the normal force F_N. The rubber block is attached to a steal plate that is pulled over the substrate by the force F. The velocity is measured for different pulling forces F and ambient temperatures T.

The whole experiment is placed in a water bath, submerged in distilled water, where the temperature T can be changed continuously from $\approx 0^\circ$ C (ice water) up to $> 90^\circ$ C (boiling water). Because of the low sliding velocities in this study, the influence of the water on the rubber friction can be neglected.

The coefficient of friction $\mu = F/F_\mathrm{N}$. In the following experiments F_N is kept constant so that the nominal pressure $\sigma_\mathrm{N} \approx 0.1$ MPa for all experiments while the pulling force F is varied. The sliding velocity is then obtained from the time the sled needs to travel a certain distance. To avoid the effect of the flash temperature on the rubber friction, the highest velocity is of order 1 mm/s while the lowest sliding

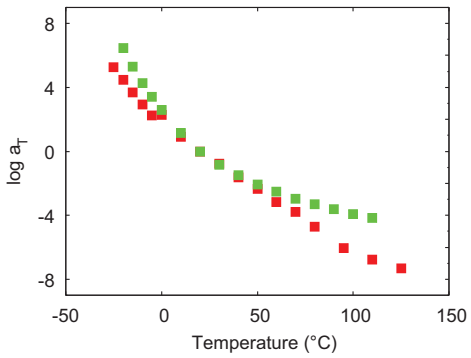

Abbildung 7.4: The logarithm of the shift factor a_T of the two rubber samples used in this experiment as a function of the temperature T. The red dots are for the tire tread rubber, the green dots for the unfilled SB rubber.

speed is of order 1 μm/s. In this experimental test F is changed so that the velocity varies from the highest possible to the lowest speed capable. The temperature T is then changed and the whole procedure repeated at different temperatures. It is possible to shift the curves, obtained at different temperatures, according to the time-temperature superposition of the Williams-Landel-Ferry equation [111] and to built up the broad (in velocity) master curve for a given reference temperature, see Fig. 7.5. It is assumed, that the rubber material does not suffer from ageing effects during the test time. For very long time spans effective time theory has to be utilized to make useful predictions [5, 106].

The rubber used in this study was a tyre tread rubber cut out of a tread block and an unfilled Styrene-Butadiene-Rubber (SBR). The temperature shift factors a_T for both compounds, as shown in Fig. 7.4, have been measured using dynamic mechanical analysis (DMA). A paving stone made of concrete was used as hard and randomly rough counter surface. The dependance of the rubber friction coefficient μ on the sliding velocity v is presented in Fig. 7.5 (a) for the tyre tread rubber and (b) for the unfilled SB rubber. As already observed in [94, 95], the friction increases with v. This is a good indication that this method to measure rubber friction is applicable. The data in Fig. 7.5 (a) is rather noisy and seems to be not as reproducible as in [33]. This may be related to the fact that in the present experiment the friction force is controlled while the velocity is measured as well as because of the complex nature of the rubber compounds measured. It has been found that the difference of the sliding velocity can be rather large when repeating the experiment and therefore it is advised to control v and measure the friction force F.

It has also been found in this first study, that the rubber sample needs to be run-in/prepared for the experiment in a proper way. During the run-in process, the interface of the rubber in contact with the substrate gets abraded and a small layer

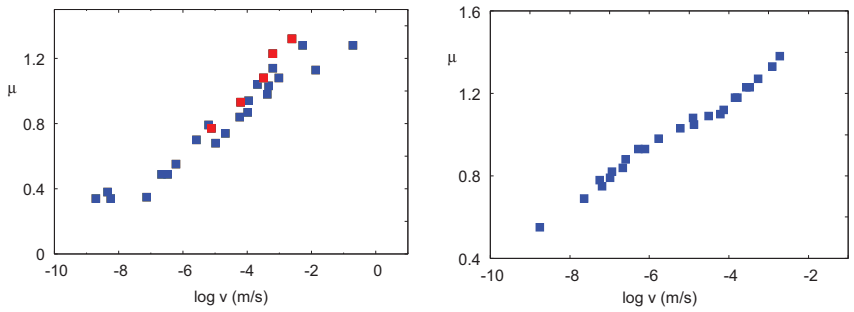

(a) Tire Tread Rubber (b) Unfilled SB rubber

Abbildung 7.5: The coefficient of friction for a rubber sample sliding on a hard and rough substrate in water (blue points). The experimental results have been shifted according to the shift factors shown in Fig. 7.4. The reference temperature is 20° C. Also shown in (a) is the friction coefficient under dry conditions at 20° C (red points).

of modified rubber is formed. The frictional properties can vary quiet a bit if the run-in process is not done in the same way for each experiment. This change in velocity as a function of number of repetition during run-in is shown in Fig. 7.6, for a constant pulling force F.

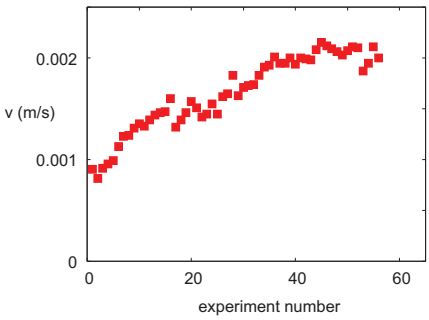

Abbildung 7.6: The measured sliding velocity as a function of the experiment number when repeating the experiment many times during the run-in phase. The driving force F is kept constant.

Summarizing this first and simple approach towards rubber friction, it can be concluded that the method is suitable to test the rubber friction theory of Persson. It is proposed to rather control the sliding velocity then the friction force. This would also allow the friction curves, as shown in Fig. 7.5, to be measured at higher veloci-

ties where the friction coefficient μ decreases with increasing v. At velocities higher then where $\mu = \mu_{\max}$ the simple experiment becomes unstable, and the sled starts to accelerate to very high sliding velocities.

7.3.2 Experimental Device and Procedure

A novel experiment, shown schematically in Fig. 7.7, has been developed. A rubber block is attached to the lower surface of an aluminium plate and brought into contact with a randomly rough substrate. The normal force F_{N} can be changed by adding plates with different weights on top of the aluminum plate. The rough surface is clamped to a steel sledge which is moved translational using a voice coil actuator. This actuator is capable to generate a constant force without force ripples, leading to a constant velocity even at very low velocities. The position of the sledge is measured to control the actuator and its velocity. As explained before, to avoid flash temperature effects, the sliding velocities are small. The highest possible velocity is of order 0.001 m/s while the lowest velocity used was $5 \cdot 10^{-7}$ m/s. To control the velocity, the position of the sledge is gauged using an analog magnetostrictive position encoder with an absolute resolution of < 10 μm. The stroke of the sledge is limited to 50 mm.

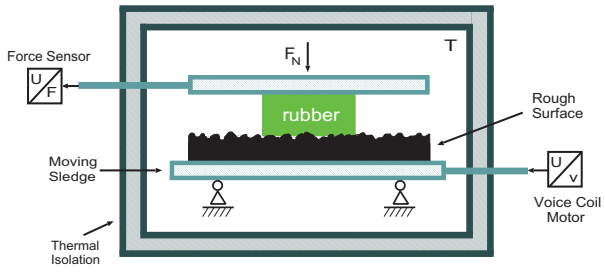

Abbildung 7.7: A rubber block is squeezed against a rough substrate. The rough surface is clamped on a sledge that is moved translational with a constant velocity v. The friction force acting on the rubber block is measured using a load cell. The instrument is located inside a box where the temperature T can be changed from -10° C to $> 120^\circ$ C. The friction forces are measured at different velocities and temperatures and then shifted according to the WLF equation to a master curve for a given reference temperature.

The friction force is measured using a tension and compression load cell that is mounted in line with the rubber-substrate interface to avoid torque. The friction forces in the linear ball bearing system are excluded from the results of the force measurements. The force cell can be replaced in order to change the effective range that can be measured. The resolution depends on the load cell used, but is always of

order 0.2 N or better. The experimental device is placed inside a temperature box where the temperature can be changed from $-10°$ C to above $120°$ C. The heating is built into the upper aluminium plate as well as in the ground plate of the linear guides to ensure a homogenous temperature distribution.

The experiment is performed as followed. A rubber test specimen is cut out off a rubber sheet and then clamped onto a sample holder. The rubber usually has a surface layer with different properties from its bulk material resulting from the production process and/or because of storing it for a long time. This layer is removed by abrading the rubber surface using sandpaper with small grain sizes. The specimen with the sample holder is then placed in the instrument, brought into contact with the rough counter surface and a constant normal force is applied. The sample is run-in at room temperature, with a sliding velocity of about 0.001 m/s, until the friction force reaches a steady state condition. Depending on the rubber material, the run-in time needed can vary quiet a bit. It is proposed to run in the specimen at high sliding velocities because of the modified layer the rubber develops at the interface. In order to have the same properties for the rubber during the whole experiment, the thickness of this layer should be large so that even if rubber particles are removed from the interface, e.g. because of wear, one has still the same layer with equal properties for the rest of the study.

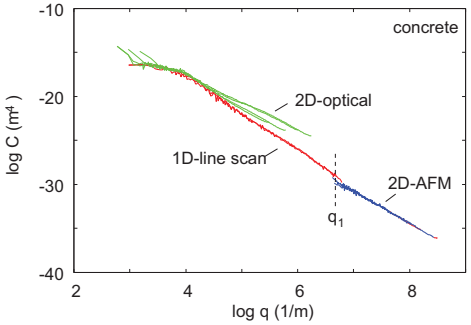

Abbildung 7.8: The surface roughness power spectrum obtained from 1D-stylus line scan (red line), 2D-optical (green line) and 2D-AFM measurements (blue line). The stylus line scan data joins smoothly with the AFM results in the overlapping wavevector range. The results from the optical data deviate in particular for large wavevectors. The large wavevector cut-off q_1 used in the calculations is indicated.

After this preparation procedure the sliding velocity is varied from high to low velocities and the friction force is measured. For each velocity, the rubber sample is slid in an oscillatory manner until a stable friction value is measured. When the experiment is completed for the full range of velocities, the temperature T is changed and the whole procedure is repeated. Finally, the experiment is repeated at room

temperature to check the results obtained in the beginning of the test. The different curves are then shifted to a master curve using the shifting factors a_T obtained from the DMA.

The surface roughness of the concrete surface used has been measured using different methods, namely 1D-stylus line scan, 2D-optical data using a white light interferometry sensor, and an infinite focus microscope, as well as atomic force microscopy (AFM). The surface roughness power spectra have been calculated from the measured surface height profiles, see Fig. 7.8. The power spectrum obtained from the data of the stylus line scan joins smoothly with that of the AFM measurements. The power spectra from the optical measurements, that have been obtained using two different sensors, deviate already at small wavevectors. In the calculations presented below, only the power spectra from the line scan and the AFM data are used. Also indicated in this figure is the large cut-off wavevector q_1 used in the analysis.

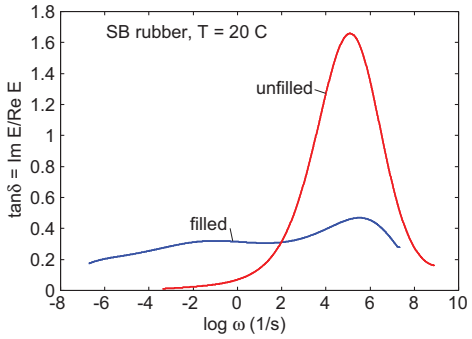

Abbildung 7.9: The $\tan\delta(\omega) = \mathrm{Im}E(\omega)/\mathrm{Re}E(\omega)$ curve as a function of the logarithm of the frequency ω for the unfilled (red line) and the filled (blue line) SB rubber used in the experiment. The modulus was measured in oscillatory shear at constant stress amplitude.

The viscoelastic moduli of the rubber compounds have been obtained using dynamic mechanical analysis (DMA). $E(\omega)$ is measured in oscillatory shear mode at a constant force amplitude of 25 N corresponding to a stress amplitude of ≈ 0.25 MPa. The rubber sample is fixed at both interfaces and then sheared at different frequencies. To obtain a broad master curve, this is repeated at several different temperatures. The data is then shifted along the frequency axis, similar to the friction results for different temperatures, and the shift factors a_T are obtained. In Fig. 7.9 the $\tan\delta$ curve is shown as a function of the logarithm of the frequency for both rubber samples.

An important issue for measuring the viscoelastic modulus of real rubber materials, in particular filled rubber, is that they exhibit non-linear rheological properties. As $E(\omega)$ enters in both dissipation mechanisms (a) and (b), it is of great import-

ance how this quantity is measured. Because of the very high strain (or stress) in the asperity contact regions, as well as in the vicinity of a crack tip, it is suggested that $E(\omega)$ is measured at as large strain (or stress) as possible, to include in an approximate way these non-linear properties, e.g. the Paine effect or the Mullins effect.

7.3.3 Comparison of Theory with Experiment

Fig. 7.10 shows the measured friction coefficient (red line) for the unfilled SB rubber as a function of the logarithm of the sliding velocity. The data is the result of experiments carried out as described in Sec. 7.3.2. Also shown in this figure is the calculated contribution from the asperity-induced viscoelastic contribution, denoted as process (a), to the rubber friction. It can be concluded that for velocities < 0.001 m/s the energy dissipation in the rubber bulk due to time dependent viscoelastic deformations is negligible in the present case. Reaching velocities > 0.01 m/s this effect actually becomes dominant. This is somehow surprising, because rubber friction was expected to be dominated by process (a) but as will be shown below, the discrepancy between the measured data and the theory predictions for $v < 0.0001$ m/s can be attributed to the shearing of a thin, confined contamination (or smear) film in the asperity contact regions [resulting from process (c)].

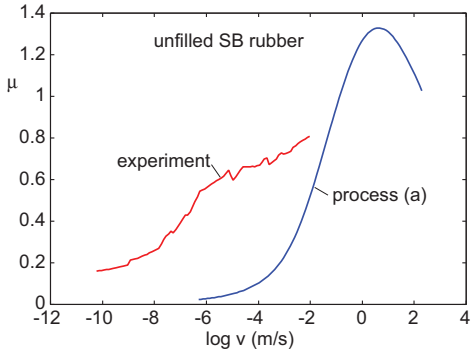

Abbildung 7.10: The measured friction coefficient as a function of the logarithm of the sliding velocity (red line) for the unfilled SBR. Also shown is the calculated asperity-induced viscoelastic contribution to the rubber friction denoted as process (a) (blue curve).

If one subtracts the theory predictions in Fig. 7.10 (blue line) from the experimental data (red line), and plot $[\mu_{\rm exp} - \mu_{\rm theory(a)}]\sigma_0/A$, where A is the area of real contact and $\sigma_0 = 0.065$ MPa the nominal pressure, one gets the frictional shear stress $\sigma_{\rm f}$ acting at the interface. This is shown in Fig. 7.11 as red line. The blue line is the predicted frictional shear stress from process (c) using $\sigma_{\rm f} = Cv^{\alpha}$ with (in SI-

units) $C = 7.45 \cdot 10^5$ and $\alpha = 0.0875$. Assuming that the thickness of the sheared film is of order $d = 3$ nm, since the shear rate $\dot{\gamma} = v/d$, one gets (in SI-units) $B = Cd^\alpha \approx 1.34 \cdot 10^5$. Thus the frictional shear stress is rather well described by Eq. (7.12), with the parameters B and α in close agreement with the values deduced from direct measurements, and from MD calculations of confined hydrocarbon films [104]. This is a strong indication that for the present case σ_f originates from shearing a thin confined contamination film.

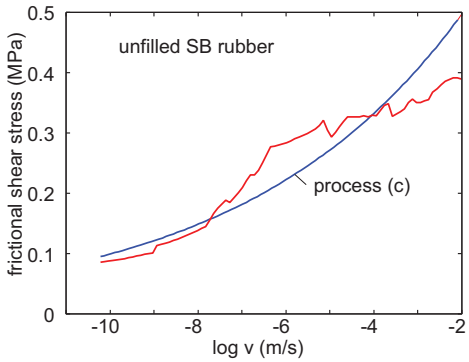

Abbildung 7.11: The calculated frictional shear stress in the area of real contact as a function of the logarithm of the sliding velocity (red line) for the unfilled SB rubber. This data is obtained by subtracting the blue curve from the red line in Fig. 7.10. The blue line is a fit to the frictional shear stress, arising from process (c), assuming $\sigma_f = Cv^\alpha$ where $C = 7.45 \cdot 10^5$ and $\alpha = 0.0875$.

This is also according to the observations made during the experiment where for unfilled SB rubber sliding on a concrete surface, a smear film could be observed on the substrate. Also, the run-in for this system involving the formation of a thin, high viscosity, liquid-like smear film, took much longer time than the run-in of the filled SB rubber, sliding on the same concrete surface (see below).

For velocities faster then $v = 0.0001$ m/s the contribution from process (c) decreases rapidly with increasing velocity. The reason for this is that increasing the sliding velocity results in a strictly monotonous decrease of the area of real contact. This reduces the contribution arising from process (c). The dependency of the area of real contact on v is illustrated in Fig. 7.12 below. At small sliding velocities A/A_0 is about 10 % of the nominal contact area. However increasing the sliding velocity results in a strong decrease to ≈ 0.1 % for velocities > 1 m/s.

The frictional shear stress from process (c) does not exhibit the same temperature dependence as the bulk viscoelastic contribution from process (a). The fact that the friction coefficient nevertheless, to a good approximation, obeys the WLF-type of temperature-velocity shifting is due to the fact that the area of real contact A

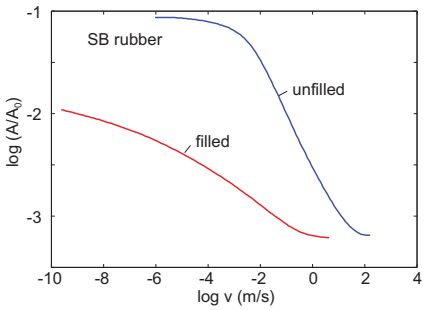

Abbildung 7.12: The logarithm of the area of real contact normalized by the apparent area of contact for the unfilled and the filled SB rubber as a function of the logarithm of the sliding velocity.

exhibits the WLF shifting.

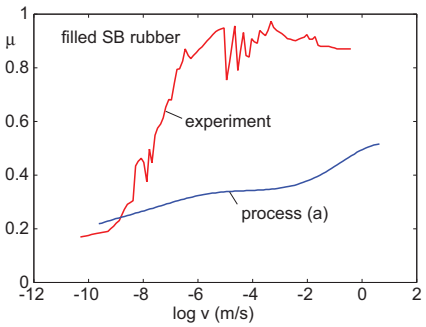

Abbildung 7.13: The measured friction coefficient as a function of the logarithm of the sliding velocity (red line) for the filled SB rubber. Also shown is the calculated asperity-induced viscoelastic contribution to the rubber friction denoted as process (a) (blue curve).

Fig. 7.13 shows the results of the friction coefficient measurements for the filled SB rubber as a function of the logarithm of the sliding velocity v (red line). As in Fig 7.10 the predicted coefficient of friction for process (a) is plotted in the same graph as blue line. Again, there is a clear discrepancy between the two curves so that it is clear that the friction cannot be explained only by accounting for the contribution of process (a). The difference can also not be explained as resulting from shearing of a thin contamination layer [process (c)] as done above for the unfilled SB rubber. The reason for this is that the area of real contact for the filled SB rubber at low sliding velocities is ~ 10 times smaller as compared with the unfilled compound, see

Fig. 7.12.

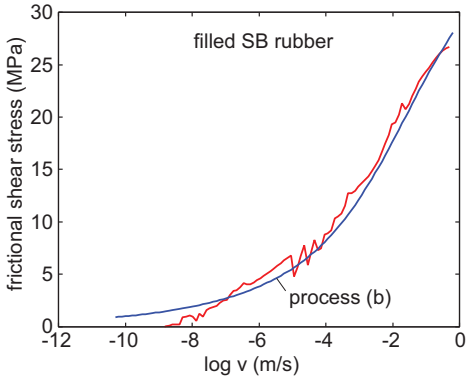

Abbildung 7.14: The calculated frictional shear stress in the area of real contact as a function of the logarithm of the sliding velocity (red line) for the filled SB rubber. This data is deduced by subtracting the blue curve from the red line in Fig. 7.13. The blue line here is a fit to the frictional shear stress arising from process (b), assuming $\sigma_{\rm f} = \sigma_1 G(v)/G_0$ where $\sigma_1 = 0.25$ MPa and $G(v)/G_0$ the viscoelastic crack propagation factor for filled SB rubber.

If one subtracts away the theory prediction of process (a), associated with the blue line in Fig. 7.13, from the measured data one gets the frictional shear stress at the interface. The result of this, $[\mu_{\rm exp} - \mu_{\rm theory(a)}]\sigma_0/A$, is shown in Fig. 7.14 as red line. The blue line in that figure is the predicted frictional shear stress from the crack opening mechanism explained in process (b). The stress arising from process (b) is found to be ~ 30 times bigger than what would result from process (c).

To check the assumption that the measured data can be explained as a superposition of the energy dissipation from both, process (a) and (b), an additional experiment has been performed where a very thin lubricant film is deposited on the interface of the filled SB rubber. If this film is thin enough, it will not affect the contribution from process (a) but it may remove (or reduce) the opening crack contribution to the rubber friction. The fluid used was a high viscosity silicon oil ($\eta = 1$ Pas). The result of this experiment can be seen in Fig. 7.15. The coefficient of friction can have negative values because of the fact that the rubber slides in both directions in a translatory motion resulting in a negative friction force for one direction. The experiment is first done without lubricant at a constant sliding velocity of 50 μm/s resulting in a constant friction coefficient of $\mu \approx 0.95$. At $t \approx 5000$ s the oil is deposited on the rubber and a drastic drop in the friction coefficient from ≈ 0.95 to ≈ 0.34 can be observed. This is in fact consistent with the contribution from process (a) at $v = 5 \cdot 10^{-5}$ m/s in Fig. 7.13 assuming that the oil film completely removes the

crack-opening contribution while the contribution from the asperity-induced viscoelastic deformations remains unchanged. A more detailed analysis can be found in [57].

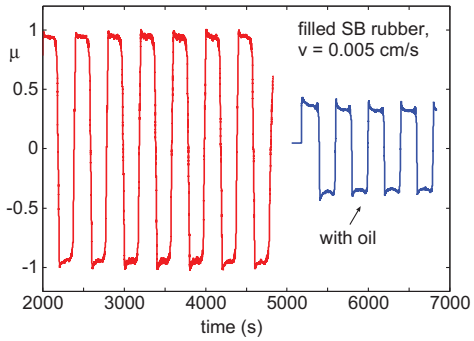

Abbildung 7.15: The measured friction coefficient $\mu = F_{\rm f}/F_{\rm N}$ of the filled SBR as a function of time for the constant sliding velocity $v = 0.05$ mm/s. At $t \approx 5000$ s a thin film of silicone oil is deposited on the rubber surface. This results in a drop of μ from ≈ 0.95 to ≈ 0.34.

Comparing the unfilled with the filled SB rubber, very different rubber wear processes have been found. This is in fact consistent with the frictional processes observed. For the unfilled SB rubber a smear film forms on the concrete surface which cannot be removed easily. In this case the wear-rate appears to slow down after some run-in time period and a constant contamination layer forms, resulting in additional energy dissipation due to shearing of this thin film. The thin and high viscosity film is in fact believed to be the reason why the crack-opening mechanism is absence for the unfilled SB rubber. The wear of the filled SB rubber instead results in micrometer-sized particles that accumulate as dry dust, and which can easily be removed by blowing air on the concrete surface. This wear process seems to occur at a steady state rate. The cut-off length, as discussed in the description of process (a), used in the present study is $q_1 = 5 \cdot 10^6$ m^{-1}m which is consistent with the linear size of the smallest wear particles observed. They are of order 10 μm when they get separated from the bulk material, see Fig. 7.16 (a). However, after the debris is removed from the rubber bulk, it sticks together and forms long wound-up clusters before it leaves the interface, see Fig. 7.16 (b) and (c).

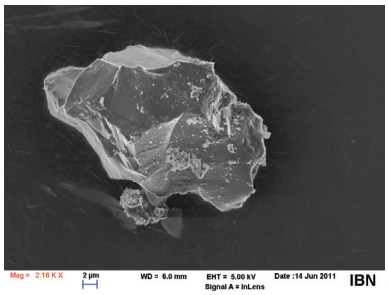

(a) A small compact wear particle with diameter ≈ 15 μm.

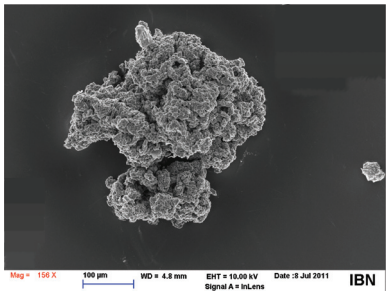

(b) A big rubber wear particle (diameter $\approx$ 300 μm) consisting of agglomerates of many small particles

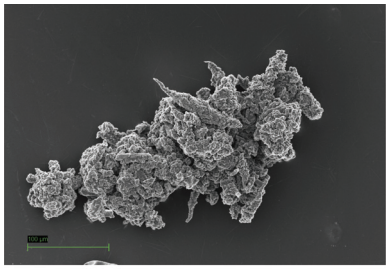

(c) Another big rubber wear particle (length $\approx$ 500 μm, width $\approx$ 150 μm) consisting of agglomerates of many small particles

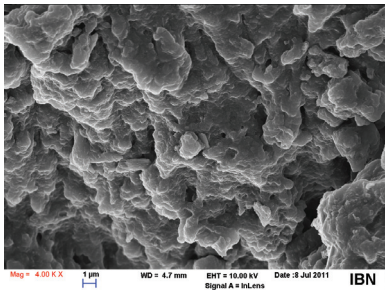

(d) Zoom-in on the wear particle in (b). Note the strong variations of the surface topography on the length scale of ~ 1 μm.

Abbildung 7.16: Pictures of the rubber wear particles of the filled SB rubber as collected after studying the friction of on a concrete surface. The pictures have been obtained using scanning electron microscopy. The smallest particles found are of order 10 μm as shown in (a). These small wear particles stick together and form large wound-up clusters before they leave the interface. Magnifying on these long clusters very rough structures can be observed as shown in (d).

7.4 Rubber Friction on Anisotropic Surfaces

Many surfaces of practical interest have surface roughness with statistical properties which are isotropic, e.g. asphalt surfaces or sand-blasted surfaces. However there exist also many surfaces that have isotropic surface roughness. For example, for technological applications many surfaces are polished unidirectional in order to obtain smooth surfaces. This results in wear tracks along the polishing direction so that the surface roughness power spectrum $C(\mathbf{q})$ depends not only on the magnitude of the wave vector $\mathbf{q}$, but also on its direction. These surfaces may have strongly anisotropic statistical properties and therefore should also exhibit frictional properties that depend on the direction of sliding.

In [18] the theory of Persson has been extended in such a way that in can also handle rubber friction on anisotropic surfaces. This is done by employing a 2D power spectrum $C(\mathbf{q})$, which can be obtained from a measured height profile $h(\mathbf{x}) = h(x, y)$ using 2D Fast Fourier Transform. To illustrate this theory, some theory predictions are presented in the following figures.

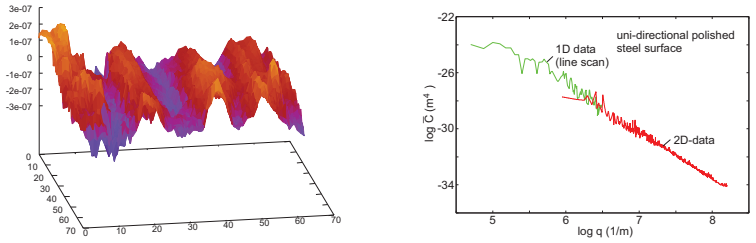

(a) (b)

Abbildung 7.17: (a) shows the surface topography (over 10 μm $\times$ 10 μm) of an uni-directional polished steel surface used to calculate the red curve in (b). In (b) the angular average of the 2D surface roughness power spectrum $\bar{C}_{2D}(q)$ from the 2D data (red curve) and from 1D data (line scan) obtained at lower resolution corresponding to smaller wave vectors is shown.

Consider a rubber block sliding on an uni-axial ground steel surface. The surface roughness topography is plotted in Fig. 7.17 (a) over an area of 10 μm x 10 μm so that one can see the grooves from the polishing process. The angular averaged surface roughness power spectrum can be calculated from this information as plotted in (b). Here the power spectra from the 2D-data and from 1D line scans are shown covering a larger wave vector range. Fig. 7.18 (a) shows the calculated coefficient of friction as a function of the logarithm of the sliding velocity for rubber. The friction has been calculated for different angles α between the sliding direction and the x-axis which lays in the direction of polishing. One can see that increasing the angle α results in a decrease in friction. This is also expected as one would assume

that sliding against the polishing grooves ($\alpha = 0$) gives the highest friction. Fig. 7.18 (b) shows the coefficient of friction as function of the sliding angle α for the same system as in Fig. 7.18 (a) and for a constant sliding velocity of 0.001 m/s. The kinetic friction for this configuration can vary up to 50 % depending on α.

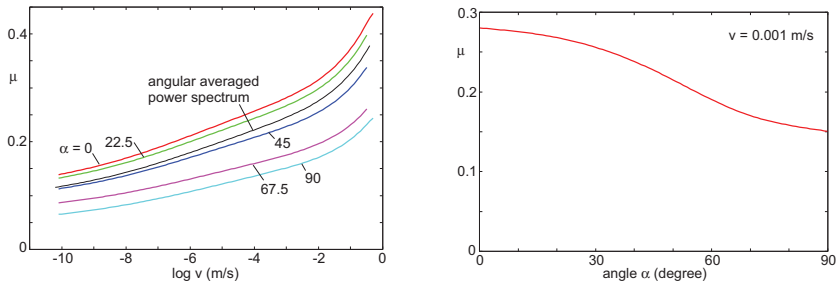

(a) (b)

Abbildung 7.18: (a) The calculated kinetic friction coefficient as a function of the logarithm of the sliding velocity for different sliding angles α between the sliding direction and the x-axis. The results are for a seal rubber compound sliding on an unidirectional polished steel surface. (b) The calculated kinetic friction coefficient as a function of the angle α. For the same system as in (a), with a constant sliding velocity of 0.001 m/s.

7.4.1 Experimental Observations

The predictions of the rubber friction theory for anisotropic surfaces has been tested qualitatively. A deeper analysis of the experimental data was not possible due to lacking information about the rubber. However, also a qualitative comparison to the predictions of the rubber friction model of Persson provides important information about its validity. For this purpose, a rubber block has been slid against a steel surface that was prepared as described above. The compound of the rubber block was a typical seal rubber but the exact composition was not known.

A well defined load has been put on the rubber using a dead weight, chosen so that in the present study the nominal squeezing force on the rubber is ≈ 0.1 MPa. The temperature was kept constant at 17° C during the experiment. A constant pulling force has then been applied to the dead weight resulting in a constant movement of the rubber sample. The sliding velocity v has been obtained from the time needed for the rubber sample to travel a certain distance. This assumes that v is constant over the distance measured. The sliding velocity is changed by variating the driving force F so that the coefficient of friction as a function of sliding velocity was measured by repeating the experiment for different sliding velocities. Dividing the pulling force

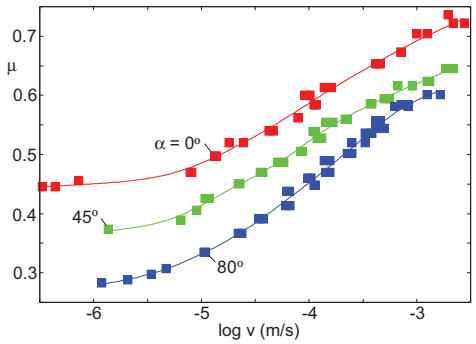

Abbildung 7.19: The friction coefficient as a function of the logarithm of the sliding velocity for three angles $\alpha = 0°$, 45° and 80° (square symbols). The rubber block was slid on a unidirectional polished steel surface at a nominal squeezing pressure of 0.1 MPa and temperature $T = 17°$ C.

with the normal force F_N gives the coefficient of friction as a function of v, α and F_N. Here only the dependance of the friction coefficient μ on the sliding velocity v and the relative angle α to the polishing groves was studied.

Before starting the experiment, it is crucial to first run in the rubber samples properly. As already discussed before, a thin skin-layer forms on the rubber surface during the run-in, and dirt particles and surface irregularities from the production process as well as from the normal atmosphere will be removed. The thin boundary layer formed on the rubber surface modify the surface properties. It is important to run in the rubber at the highest velocity and with the highest coefficient of friction. Thereby a boundary layer with rather high thickness can be formed. This layer hopefully is thick enough so that it does not change very much during the following tests at lower sliding speeds and normal forces. In between the experiments the steel surface has been cleaned using a mixture with 10 % acetylacetone in isopropanol.

Fig. 7.19 shows the measured friction coefficient as a function of the logarithm of the sliding speed for three different angles $\alpha = 0$, 45° and 80°. The theory predicts that the real area of contact for these three angles is nearly the same so that the dependance of the friction on α is likely due to hysteretic contribution alone. At high velocities the 80° curve increases stronger as expected. This is because of the shear forces tilting the slider into the direction of the wear tracks. The measurements presented are for a different rubber and a different (but similarly prepared) substrate than the compound used in the calculations plotted in Fig. 7.18 (a) and (b). Therefore the results in Fig. 7.18 (a) cannot be compared quantitatively to the calculations. But qualitatively the agreement between the experimental results and the theory prediction is good. The calculated friction for different α increases faster with increasing sliding velocities than in the experiment. This can have different

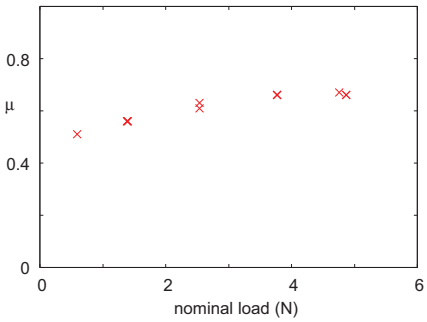

Abbildung 7.20: The friction coefficient μ as a function of the normal load when sliding orthogonal to the polishing direction ($\alpha = 0°$). The velocity of the tread rubber block was kept constant at ≈ 0.2 mm/s. A weak load dependence of the friction could be observed.

reasons, namely that the calculations only included surface roughness over slightly more than 2 decades in length scale, or there may be another non-negligible contribution to the friction, e.g., from energy dissipation during crack opening which exhibits a different velocity dependance.

An additional experiment shows that in this configuration studied, the friction coefficient μ has a very weak dependence on the applied normal load, as can be seen in Fig. 7.20. If adhesion manifested itself on a macroscopic scale as a finite pull-off force, the friction coefficient would in fact decrease with increasing load, whereas Fig. 7.20 shows that the opposite is the case. This indicates that adhesion is not so important in the experimental study presented above.

7.5 Conclusion on Rubber Friction

Rubber friction is a topic of huge importance for many technological applications. Understanding rubber friction involves a deep insight into the contact mechanics between the rubber solid and the rough substrate. Until recently, there did not exist a good theoretical approach towards contact mechanics so that rubber friction is still a not well understood phenomena. In this section a novel theory approach based on the contact mechanics theory of Persson has been introduced where rubber friction is modeled as superposition of different energy dissipation mechanisms. In order to test this theory, an experimental method to measure rubber friction, based on the simple sledge experiments by Leonardo da Vinci, has been discussed and tested with a simple experiment. This method has then been adopted to design an instrument to study rubber friction at different temperatures and very low sliding velocities. The experimental data has been shifted to a smooth master-curve, using the temperature-frequency shifting factors obtained from the measurements of the bulk viscoelastic

modulus of the compounds. It has then been compared with the theory predictions of Persson. The theory takes into account the contribution to the friction from the substrate asperity-induced viscoelastic deformations of the rubber and from shearing the area of real contact. The experimental data agrees very well with the calculated rubber friction for the two systems studied. Similar experimental results have also been found with different rubber on rough surfaces in [13]. It is concluded that for the present case of rubber sliding on rough and hard surfaces, the approach by Persson is capable to describe the different energy dissipation mechanisms.

An additional experiment has been performed to test the predictions of the theory for rubber friction on anisotropic surfaces qualitatively. This comparison between the experimental data, obtained by sliding a rubber sample on an uniaxial ground steel surface, to the theory predictions resulted in a good qualitative agreement.

8 Summary

This thesis presented an experimental study of contact mechanics and rubber friction. These are topics of huge importance in Nature and in technology. Despite its importance and the theoretical and experimental effort carried out, contact mechanics and rubber friction are still not well understood today. The motivation of this work has been to compare the approach of Persson to contact mechanics and rubber friction with state-of-the-art theories and to test its accuracy by comparing the predictions with experimental results. The experiments described here not only address the two topics contact mechanics and rubber friction but also different applications that are of great importance in many technological systems. It is the first time that experimental data has been used to test the approach of Persson in detail.

Very good agreement has been found with the Persson approach, while the predictions of the standard theories disagree even qualitatively. This is due to severe approximations made in the state-of-the-art theories, such as the neglect of long-range elastic deformations and the oversimplified description of surface roughness. Very good agreement has been found when the approach of Persson was applied to different problems involving contact mechanics, including the leak rate of seals or the squeeze-out of a fluid. There are no fitting parameters used in the analysis. Within the accuracy of the experiments, the theory on contact mechanics by Persson has been shown to work very well.

In the last section of the thesis, the predictions of a rubber friction theory based on the contact mechanics approach are tested using a novel instrument that has been designed. The experimental data could be explained well by the theory if different energy dissipation mechanisms are taken into account and the rubber friction theory of Persson explains the results within the accuracy of the measurements. It is the only physical model that can presently be applied to rubber friction on hard and rough substrates.

More work needs to be done in order to test the influence of temperature effects (flash temperature) on rubber friction during energy dissipation. This is crucial for technical problems, such as friction of a tyre or dynamic seals. Further study of rubber friction on different substrates, e.g. road surfaces and ground steel surfaces, is needed to test the theory in detail.

Literaturverzeichnis

[1] J.F. Archard. Elastic deformation and the laws of friction. *Proc. R. Soc. Lond. A.*, 243(1233):190 – 205, 1957.

[2] J.F. Archard. The temperature of rubbing surfaces. *WEAR*, 2(6):438 – 455, October 1959.

[3] M. Bahrami, J.R. Culham, M.M. Yananovich, and G.E. Schneider. Review of thermal joint resistance models for nonconforming rough surfaces. *APPL MECH REV*, 59(1 - 6):1 – 12, January 2006.

[4] J.R. Barber. Bounds on the electrical resistance between contacting elastic rough bodies. *Proc. R. Soc. Lond. A.*, 459(2029):53 – 66, January 2003.

[5] E.J. Barbero. *Creep and Fatigue in Polymer Matrix Composites*. CRC Press, Boca Raton, November 2010.

[6] M. Benz, K.J. Rosenberg, E.J. Kramer, and J.N. Israelachvili. The deformation and adhesion of randomly rough and patterned surfaces. *J PHYS CHEM B*, 110(24):11884 – 11893, June 2006.

[7] J.H.H. Bongaerts, K. Fourtouni, and J.R. Stokes. Soft-tribology: Lubrication in a compliant pdms-pdms contact. *TRIBOL INT*, 40(10 - 12):1531 – 1542, December 2007.

[8] M. Bori-Brunetto, B. Chiaia, and M. Ciavarella. Incipient sliding of rough surfaces in contact: a multiscale numerical analysis. *COMPUT METHOD APPL MECH ENG*, 190(46-47):6053 – 6073, September 2001.

[9] F.P. Bowden and D. Tabor. *Friction and Lubrication*. Methuen & Co., London, 1956.

[10] F. Brochard-Wyart, A. Buguin, P. Martin, and O. Sandre. Adhesion of soft objects on wet substrates. *J PHYS-CONDENS MATTER*, 12(8A):A239 – A244, February 2000.

[11] D.A.G. Bruggeman. Berechnung verschiedener physikalischer konstanten von heterogenen substanzen. *ANN PHYS-BERLIN*, 24(7):636 – 664, November 1935.

[12] A.W. Bush, R.D. Gibson, and T.R. Thomas. The elastic contact of a rough surface. *WEAR*, 35(1):87 – 111, November 1975.

[13] L. Busse, I. Boubakri, and M. Klüppel. Friction master curves for rubber on dry and wet granite. *KGK*, 64(5):35 – 39, May 2011.

[14] C. Campana and M.H. Müser. Contact mechanics of real vs. randomly rough surfaces: A green's function molecular dynamics study. *EPL*, 77:38005, 2007.

[15] C. Campana, M.H. Müser, and M.O. Robbins. Elastic contact between self-affine surfaces: comparison of numerical stress and contact correlation functions with analytic predictions. *J PHYS-CONDENS MATTER*, 20(35):354013, September 2008.

[16] G. Carbone. A slightly corrected greenwood and williamson model predicts asymptotic linearity between contact area and load. *J MECH PHYS SOLIDS*, 57(7):1093 – 1102, July 2009.

[17] G. Carbone and F. Bottiglione. Asperity contact theories: Do they predict linearity between contact area and load? *J MECH PHYS SOLIDS*, 56(8):2555 – 2572, August 2008.

[18] G. Carbone, B. Lorenz, B.N.J. Persson, and A. Wohlers. Contact mechanics and rubber friction for randomly rough surfaces with anisotropic statistical properties. *EUR PHYS J E*, 29(3):275 – 284, July 2009.

[19] G. Carbone and L. Mangialardi. Adhesion and friction of an elastic half-space in contact with a slightly wavy rigid surface. *J MECH PHYS SOLIDS*, 52(6):1267 – 1287, June 2004.

[20] G. Carbone, L. Mangialardi, and B.N.J. Persson. Adhesion between a thin elastic plate and a hard randomly rough substrate. *PHYS REV B*, 70(12):125407, September 2004.

[21] G. Carbone, M. Scaraggi, and U. Tartaglino. Adhesive contact of rough surfaces: Comparison between numerical calculations and analytical theories. *EUR PHYS J E*, 30(1):65 – 74, September 2009.

[22] R. K. Flitney. *Seals and Sealing Handbook*. Elsevier Science Ltd, 5 edition, September 2007.

[23] K.N.G. Fuller and D. Tabor. Effect of surface-roughness on adhesion of elastic solids. *Proc. R. Soc. Lond. A.*, 345(1642):327 – 342, September 1975.

[24] A. Le Gal, X. Yang, and M. Klüppel. Evaluation of sliding friction and contact mechanics of elastomers based on dynamic-mechanical analysis. *J CHEM PHYS*, 123(1):014704, July 2005.

[25] G. Gäbel, M. Kröger, and E.U. Saemann. Local contact between tyre and road in experiment and simulation. *Proceedings of Internoise*, 8(Istanbul):48 – 53, 2007.

[26] A.N. Gent. Compression of rubber blocks. *Rubber Chem. Technol.*, 67(3):549 – 558, July - August 1994.

[27] A.N. Gent. Adhesion and strength of viscoelastic solids. is there a relationship between adhesion and bulk properties? *LANGMUIR*, 12(19):4492 – 4496, September 1996.

[28] A.N. Gent and J. Schultz. Effect of wetting liquids on the strength of adhesion of viscoelastic materials. *J ADHESION*, 3(4):281 – 294, 1972.

[29] A.N. Gent and J.D. Walter, editors. *The Pneumatic Tire*. US Departement of Transportation, February 2006.

[30] J.A. Greenwood. Constriction resistance and the real area of contact. *British Journal of Applied Physics*, 17(12):1621 – 1632, 1966.

[31] J.A. Greenwood. A simplified elliptic model of rough surface contact. *WEAR*, 261(2):191 – 200, July 2006.

[32] J.A. Greenwood and J.B.P. Williamson. Contact of nominally flat surfaces. *Proc. R. Soc. Lond. A.*, 295(1442):300 – 319, December 1966.

[33] K.A. Grosch. Relation between friction and visco-elastic properties of rubber. *Proc. R. Soc. Lond. A.*, 274(1356):21 – 39, June 1963.

[34] J.S. Havinga and S. de Meij. Engineering with natural rubber. *Naturalrubber*, 13:2–3, February 1999.

[35] G. Heinrich and M. Klüppel. Rubber friction, tread deformation and tire traction. *WEAR*, 265(7 - 8):1052 – 1060, September 2008.

[36] G. Heinrich, M. Klüppel, and T.A. Vilgis. Evaluation of self-affine surfaces and their implication for frictional dynamics as illustrated with a rouse material. *COMPUT THEOR POLYM SCI*, 10(1 - 2):53 – 61, March 2000.

[37] G. Heinrich, J. Struve, and G. Gerber. Mesoscopic simulation of dynamic crack propagation in rubber materials. *Polymer*, 43(2):395 – 401, January 2002.

[38] H. R. Hertz. Ueber die berührung fester elastischer körper. *Journal für die reine und angewandte Mathematik*, 92:156 –171, 1882.

[39] C.Y. Hui, Y.Y. Lin, and J.M. Baney. The mechanics of tack: Viscoelastic contact on a rough surface. *J POLYM SCI B-POLYM PHYS*, 38(11):1485 – 1495, Juny 2000.

[40] S. Hyun, L. Pei, J.F. Molinari, and M.O. Robbins. Finite-element analysis of contact between elastic self-affine surfaces. *PHYS REV E*, 70(2):026117, August 2004.

[41] J. Israelachvili. *Intermolecular And Surface Forces*. Academic Press, London, 3 edition, November 2010.

[42] K.L. Johnson. *Contact Mechanics*. Cambridge University Press, 1966.

[43] K.L. Johnson, K. Kendall, and A.D. Roberts. Surface energy and contact of elastic solids. *Proc. R. Soc. Lond. A.*, 324(1558):301 – 313, 1971.

[44] P. Jost. Lubrication (tribology) - education and research. *A Report on the Present Position and Industry Needs*, Department of Education and Science, HM Stationary Office, London, 1966.

[45] K. Joulain, J.P. Mulet, F. Marquier, R. Carminati, and J.J. Greffet. Surface electromagnetic waves thermally excited: Radiative heat transfer, coherence properties and casimir forces revisited in the near field. *SURF SCI REP*, 57(3 - 4):59 – 112, May 2005.

[46] S. Kim, W. Jeong, Y. Parl, and S. Lee. Prediction method for tire air-pumping noise using a hybrid technique. *J ACOUST SOC AMER*, 119(6):3799 – 3812, 2006.

[47] S. Kirkpatrick. Percolation and conduction. *REV MOD PHYS*, 45(4):574 – 588, October 1973.

[48] M. Klüppel and G. Heinrich. Rubber friction on self-affine road tracks. *Rubber Chem. Technol.*, 73(4):578 – 606, September - October 2000.

[49] M.S. Longuet-Higgins. The statistical analysis of a random, moving surface. *Phil. Trans. R. Soc. Lond. A*, 249:321–387, 1957.

[50] B. Lorenz, G. Carbone, and C. Schulze. Average separation between a rough surface and a rubber block: Comparison between theories and experiments. *WEAR*, 268(7 - 8):98 – 990, March 2010.

[51] B. Lorenz and B.N.J. Persson. Interfacial separation between elastic solids with randomly rough surfaces: comparison of experiment with theory. *J PHYS-CONDENS MATTER*, 21:015003, January 2009.

[52] B. Lorenz and B.N.J. Persson. Leak rate of seals: Comparison of theory with experiment. *EPL*, 86:44006, May 2009.

[53] B. Lorenz and B.N.J. Persson. Leak rate of seals: Effective-medium theory and comparison with experiment. *EUR PHYS J E*, 31(2):159 – 167, February 2010.

[54] B. Lorenz and B.N.J. Persson. On the dependence of the leak rate of seals on the skewness of the surface height probability distribution. *EPL*, 90(38002):38002, May 2010.

[55] B. Lorenz and B.N.J. Persson. Time-dependent fluid squeeze-out between solids with rough surfaces. *EUR PHYS J E*, 32(3):281 – 290, July 2010.

[56] B. Lorenz and B.N.J. Persson. Fluid squeeze-out between rough surfaces: comparison of theory with experiment. *submitted to J PHYS-CONDENS MATTER*, 2011.

[57] B. Lorenz and B.N.J. Persson. Rubber friction: comparison of theory with experiment. *to be published*, 2011.

[58] W. Manners and J.A. Greenwood. Some observations on persson's diffusion theory of elastic contact. *WEAR*, 261(5 - 6):600 – 610, September 2006.

[59] D. Maugis. On the additivity of losses at propagating cracks in polymer adhesion and tearing. *J ADHES SCI TECHNOL*, 9(7):1005 – 1008, 1995.

[60] D. Maugis and M. Barquins. Fracture mechanics and adherence of viscoelastic bodies. *J PHYS-D-APPL PHYS*, 11(14):1989 – 2024, October 1978.

[61] Y.F. Mo, K.T. Turner, and I. Szlufarska. Friction laws at the nanoscale. *NATURE*, 457(7233):1116 – 1119, February 2009.

[62] M. Mofidi, B. Prakash, B.N.J. Persson, and O. Albohr. Rubber friction on (apparently) smooth lubricated surfaces. *J PHYS-CONDENS MATTER*, 20(8):085223, Februar 2008.

[63] M.H. Müser. Rigorous field-theoretical approach to the contact mechanics of rough elastic solids. *PHYS REV LETT*, 100(5):055504, Februar 2008.

[64] A.H. Muhr and A.D. Roberts. Rubber abrasion and wear. *WEAR*, 158(1 - 2):213 – 228, October 1992.

[65] H. Murrenhoff. Bericht über biologisch schnell abbaubare schmierstoffe und hydraulikflüssigkeiten. *Bundesministerium für Verbraucherschutz, Ernährung und Landwirtschaft*, 1:1 – 67, July 2002.

[66] P.R. Nayak. Random rocess model of rough surfaces. *J. Lubrication Technol.*, 93:398, 1971.

[67] H.B. Pacejka. *Tyre and Vehicle Dynamics*. Butterworth Heinemann, Oxford, 2nd edition, 2005.

[68] N. Patir and H.S. Cheng. Average flow model for determining effects of 3-dimensional roughness on partial hydrodynamic lubrication. *J LUBRIC TECH-T ASME*, 100(1):12 – 17, 1978.

[69] N. Patir and H.S. Cheng. Application of average flow model to lubrication between rough sliding surfaces. *J LUBRIC TECH-T ASME*, 101(2):220 – 230, 1979.

[70] L. Pei, S. Hyun, J.F. Molinari, and M.O. Robbins. Finite element modeling of elasto-plastic contact between rough surfaces. *J MECH PHYS SOLIDS*, 53(11):2385 – 2409, November 2005.

[71] B.N.J. Persson. On the theory of rubber friction. *SURFACE SCI*, 401(3):445 – 454, April 1998.

[72] B.N.J. Persson. *Sliding Friction: Physical Principles and Applications*. Springer, Berlin, 2nd edition edition, July 2000.

[73] B.N.J. Persson. Elastoplastic contact between randomly rough surfaces. *PHYS REV LETT*, 87:116101, September 2001.

[74] B.N.J. Persson. Theory of rubber friction and contact mechanics. *J CHEM PHYS*, 115(8):3840 – 3861, August 2001.

[75] B.N.J. Persson. Adhesion between an elastic body and a randomly rough hard surface. *EUR PHYS J E*, 8(4):385 – 401, July 2002.

[76] B.N.J. Persson. Contact mechanics for randomly rough surfaces. *SURF SCI REP*, 61(4):201 – 227, June 2006.

[77] B.N.J. Persson. Rubber friction: role of the flash temperature. *J PHYS-CONDENS MATTER*, 18(32):7789 – 7823, August 2006.

[78] B.N.J. Persson. Relation between interfacial separation and load: A general theory of contact mechanics. *PHYS REV LETT*, 99(125502):125502, September 2007.

[79] B.N.J. Persson. On the elastic energy and stress correlation in the contact between elastic solids with randomly rough surfaces. *J PHYS-CONDENS MATTER*, 20(31):312001, August 2008.

[80] B.N.J. Persson. Fluid dynamics at the interface between contacting elastic solids with randomly rough surfaces. *J PHYS-CONDENS MATTER*, 22(26):265004, July 2010.

[81] B.N.J. Persson. Rolling friction for hard cylinder and sphere on viscoelastic solid. *EUR PHYS J E*, 33(4):327 – 333, December 2010.

[82] B.N.J. Persson. Rubber friction and tire dynamics. *J PHYS-CONDENS MATTER*, 23(1):015003, Januar 2011.

[83] B.N.J. Persson, O. Albohr, C. Creton, and V. Peveri. Contact area between a viscoelastic solid and a hard, randomly rough, substrate. *J CHEM PHYS*, 120(18):8779 – 8793, May 2004.

[84] B.N.J. Persson, O. Albohr, G. Heinrich, and H. Ueba. Crack propagation in rubber-like materials. *J PHYS-CONDENS MATTER*, 17(44):R1071 – 1142, November 2005.

[85] B.N.J. Persson, O. Albohr, U. Tartaglino, A.I. Volokitin, and E. Tosatti. On the nature of surface roughness with application to contact mechanics, sealing, rubber friction and adhesion. *J PHYS-CONDENS MATTER*, 17(1):R1 – R62, January 2005.

[86] B.N.J. Persson and E.A. Brener. Crack propagation in viscoelastic solids. *PHYS REV E*, 71(3):036123, March 2005.

[87] B.N.J. Persson, F. Bucher, and B. Chiaia. Elastic contact between randomly rough surfaces: Comparison of theory with numerical results. *PHYS REV B*, 65:184106, May 2002.

[88] B.N.J. Persson, B. Lorenz, and A.I. Volokitin. Heat transfer between elastic solids with randomly rough surfaces. *EUR PHYS J E*, 31(1):3 – 24, January 2010.

[89] B.N.J. Persson, I.M. Sivebaek, V.N. Samoilov, K. Zhao, A. Volokitin, and Z. Zhang. On the origin of amonton's friction law. *J PHYS-CONDENS MATTER*, 20(39):395006, October 2008.

[90] B.N.J. Persson and A.I. Volokitin. Rubber friction on smooth surfaces. *EUR PHYS J E*, 21(1):69 – 80, September 2006.

[91] B.N.J. Persson, A.I. Volokitin, and E. Tosatti. Role of the external pressure on the dewetting of soft interfaces. *EUR PHYS J E*, 11(4):409 – 413, August 2003.

[92] B.N.J. Persson and C. Yang. Theory of the leak-rate of seals. *J PHYS-CONDENS MATTER*, 20:315011, August 2008.

[93] V.L. Popov. *Contact Mechanics and Friction: Physical Principles and Applications*, volume 1. Springer, Berlin, February 2010.

[94] F.L. Roth, R.L. Driscoll, and W.L. Holt. Frictional properties of rubber. *J RES NATL INST STAN*, 28(4):439 – 462, April 1942.

[95] F.L. Roth, R.L. Driscoll, and W.L. Roth. Frictional properties of rubber. *Rubber Chem. Technol.*, 16(1):155 – 178, 1943.

[96] F. Sahlin, R. Larsson, and P. Lugt. Simulating leakage between rough seal surfaces. *Paper F in: Lubrication, contact mechanics and leakage between rough surfaces*, 1:191 – 215, 2008.

[97] E.A. Sakai. Measurement and visualization of the contact pressure distribution of rubber disks and tires. *Tire Science and Technology*, 23(4):238, 1995.

[98] M. Scaraggi, G. Carbone, B.N.J. Persson, and D. Dini. Lubrication in soft rough contacts: A novel homogenized approach. part i - theory. *submitted to Soft matter*, 2011.

[99] A. Schallamach. A theory of dynamic rubber friction. *WEAR*, 6(5):375 – 382, September - October 1963.

[100] J. Scheibert, A. Prevost, J. Frelat, P. Rey, and G. Debregeas. Experimental evidence of non-amontons behaviour at a multi-contact interface. *EPL*, 83:34003, August 2008.

[101] D. Segal and A. Nitzan. Steady-state quantum mechanics of thermally relaxing systems. *CHEM PHYS*, 268(1 - 3):315 – 335, June 2001.

[102] D. Segal and A. Nitzan. Conduction in molecular junctions: inelastic effects. *CHEM PHYS*, 281(2 - 3):235 – 256, August 2002.

[103] Y. Selzer, M.A. Cabassi, T.S. Mayer, and D.L. Allara. Temperature effects on conduction through a molecular junction. *NANOTECHNOLOGY*, 15(7):S483 – S488, July 2004.

[104] I.M. Sivebaek, V.N. Samoilov, and B.N.J. Persson. *to be published*, 2011.

[105] D. Stauffer and A. Aharony. *Introduction To Percolation Theory*. CRC Press, July 1994.

[106] L.C.E. Struik. *Physical aging in amorphous polymers and other materials*. Elsevier Science Ltd, Februar 1978.

[107] J.B. Suh. *Stress analysis of rubber blocks under vertical and shear loading*. PhD thesis, University of Akron, August 2007.

[108] J.H. Tripp. Surface-roughness effects in hydrodynamic lubrication - the flow factor method. *J LUBRIC TECH-T ASME*, 105(3):458 – 465, October 1983.

[109] A.I. Volokitin and B.N.J. Persson. Near-field radiative heat transfer and noncontact friction. *REV MOD PHYS*, 79(4):1291 – 1329, October - December 2007.

[110] S. Westermann, F. Petry, R. Boes, and G. Thielen. Experimental investigations into the predictive capabilities of current physical rubber friction theories. *KGK*, 57:645 – 650, December 2004.

[111] M.L. Williams, R.F. Landel, and J.D. Ferry. The temperature dependence of relaxation mechanisms in amorphous polymers and other glass-forming liquids. *J AM CHEM SOC*, 77(14):3701 – 3707, July 1955.

[112] S. Yamada. General shear-thinning dynamics of confined fluids. *TRIBOL LETT*, 13(3):167 – 171, October 2002.

[113] C. Yang and B.N.J. Persson. Contact mechanics: contact area and interfacial separation from small contact to full contact. *J PHYS-CONDENS MATTER*, 20(21):215214, May 2008.

[114] C. Yang, U. Tartaglino, and B.N.J. Persson. A multiscale molecular dynamics approach to contact mechanics. *EUR PHYS J E*, 19(1):47 – 58, January 2006.

Acknowledgements

This dissertation was conducted at the Institut für Festkörperforschung (*IFF*) at the Forschungszentrum Jülich in cooperation with the Institut für fluidtechnische Antriebe und Steuerungen (*IFAS*) at the RWTH Aachen University.

Foremost I want to express my gratitude towards my supervisors Univ.-Prof. Dr.-Ing. Hubertus Murrenhoff and Univ.-Prof. Dr. rer. nat. Stefan Blügel for giving me the opportunity to work on this dissertation and for mentoring the work related hereto. I also thank Univ.-Prof. Dr.-Ing. Christoph Broeckmann for being the examination chairman.

It would have been next to impossible to write this thesis without the help and guidance of my advisor Dr. Bo N. J. Persson. He motivated this work and supported me every day and on all challenges conquered during this time.

I thank Novo Nordisk A/S and Pirelli & C. SpA for financial support. I further thank Prof. Dr. Ion M. Sivebaek and Dr. Ugo Tartaglino for all their support.

Last but not least I thank everybody who helped me, both professional and private.

1. **Soft Matter**
   From Synthetic to Biological Materials
   Lecture manuscripts of the 39th IFF Spring School March 3 – 14, 2008
   Jülich, Germany
   edited by J.K.G. Dhont, G. Gompper, G. Nägele, D. Richter, R.G. Winkler (2008),
   c. 1000 pages
   ISBN: 978-3-89336-517-3

2. **Structural analysis of diblock copolymer nanotemplates using grazing incidence scattering**
   by D. Korolkov (2008), III, 167 pages
   ISBN: 978-3-89336-522-7

3. **Thermal Nonequilibrium**
   Thermal forces in fluid mixtures
   Lecture Notes of the 8th International Meeting on Thermodiffusion,
   9 – 13 June 2008, Bonn, Germany
   edited by S. Wiegand, W. Köhler (2008), 300 pages
   ISBN: 978-3-89336-523-4

4. **Synthesis of CMR manganites and ordering phenomena in complex transition metal oxides**
   by H. Li (2008), IV, 176 pages
   ISBN: 978-3-89336-527-2

5. **Neutron Scattering**
   Lectures of the JCNS Laboratory Course held at the Forschungszentrum Jülich and the research reactor FRM II of TU Munich
   edited by R. Zorn, Th. Brückel, D. Richter (2008), ca. 500 pages
   ISBN: 978-3-89336-532-6

6. **Ultrafast Magnetization Dynamics**
   by S. Woodford (2008), 130 pages
   ISBN: 978-3-89336-536-4

7. **Role of Surface Roughness inTribology: from Atomic to Macroscopic Scale**
   by C. Yang (2008), VII, 166 pages
   ISBN: 978-3-89336-537-1

8. **Strahl- und Spindynamik von Hadronenstrahlen in Mittelenergie-Ringbeschleunigern**
   von A. Lehrach (2008), II, 171 Seiten
   ISBN: 978-3-89336-548-7

9. **Phase Behaviour of Proteins and Colloid-Polymer Mixtures**
   by C. Gögelein (2008), II, 147 pages
   ISBN: 978-3-89336-555-5

10. **Spintronics – From GMR to Quantum Information**
    Lecture Notes of the 40th IFF Spring School March 9 – 20, 2009
    Jülich, Germany
    edited by St. Blügel, D. Bürgler, M. Morgenstern, C. M. Schneider,
    R. Waser (2009), c. 1000 pages
    ISBN: 978-3-89336-559-3

11. **ANKE / PAX Workshop on SPIN Physics**
    JINR, Dubna, Russia / June 22. – 26, 2009
    Org. Committee: A. Kacharava, V. Komarov, A. Kulikov, P. Lenisa, R. Rathmann,
    H. Ströher (2009), CD-ROM
    ISBN: 978-3-89336-586-9

12. **Entwicklung einer Nanotechnologie-Plattform für die Herstellung Crossbar-basierter Speicherarchitekturen**
    von M. Meier (2009), 135 Seiten
    ISBN: 978-3-89336-598-2

13. **Electronic Oxides –**
    Correlation Phenomena, Exotic Phases and Novel Functionalities
    Lecture Notes of the 41st IFF Spring School March 8 – 19, 2010
    Jülich, Germany
    edited by St. Blügel, T. Brückel, R. Waser, C.M. Schneider (2010), ca. 1000 pages
    ISBN: 978-3-89336-609-5

14. **4th Georgian-German School and Workshop in Basic Science**
    Tbilisi, Georgia / May 3 – 7, 2010
    Org. Committee: E. Abrosimova, R. Botchorishvili, A. Kacharava, M. Nioradze,
    A. Prangishvili, H. Ströher (2010); CD-ROM
    ISBN: 978-3-89336-629-3

15. **Neutron Scattering**
    Lectures of the JCNS Laboratory Course held at Forschungszentrum Jülich and the research reactor FRM II of TU Munich
    edited by Th. Brückel, G. Heger, D. Richter, G. Roth and R. Zorn (2010),
    ca 350 pages
    ISBN: 978-3-89336-635-4

16. **Ab *initio* investigations of magnetic properties of ultrathin transition-metal films on *4d* substrates**
    by A. Al-Zubi (2010), II, 143 pages
    ISBN: 978-3-89336-641-5

17. **Investigation of a metal-organic interface realization and understanding of a molecular switch**
    by O. Neucheva (2010), 134 pages
    ISBN: 978-3-89336-650-7

18. **Reine Spinströme in lateralen Spinventilen, *in situ* Erzeugung und Nachweis**
von J. Mennig (2010), V, 95 Seiten
ISBN: 978-3-89336-684-2

19. **Nanoimprint Lithographie als Methode zur chemischen Oberflächenstrukturierung für Anwendungen in der Bioelektronik**
von S. Gilles (2010), II, 169 Seiten
ISBN: 978-3-89336-686-6

20. **Macromolecular Systems in Soft- and Living-Matter**
Lecture Notes of the 42nd IFF Spring School 2011 February 14 – 25, 2011 Jülich, Germany
edited by J. K.G. Dhont, G. Gompper, P. R.Lang, D. Richter, M. Ripoll, D. Willbold, R. Zorn (2011), ca. 1000 pages
ISBN: 978-3-89336-688-0

21. **The spin structure of magnetic nanoparticles and in magnetic nanostructures**
by S. Disch (2011), V, 342 pages
ISBN: 978-3-89336-704-7

22. **Element-selective and time-resolved magnetic investigations in the extreme ultraviolet range**
by P. Grychtol (2011), xii, 144 pages
ISBN: 978-3-89336-706-1

23. **Spin-Transfer Torque Induced Dynamics of Magnetic Vortices in Nanopillars**
by V. Sluka (2011), 121 pages
ISBN: 978-3-89336-717-7

24. **Adsorption von Phthalocyaninen auf Edelmetalloberflächen**
von I. Kröger (2011), vi, 206 Seiten
ISBN: 978-3-89336-720-7

25. **Time-Resolved Single Molecule FRET Studies on Folding/Unfolding Transitions and on Functional Conformational Changes of Phosphoglycerate Kinase**
by T. Rosenkranz (2011), III, 139 pages
ISBN: 978-3-89336-721-4

26. **NMR solution structures of the MIoK1 cyclic nucleotide-gated ion channel binding domain**
by S. Schünke (2011), VI, (getr. pag.)
ISBN: 978-3-89336-722-1

27. **Neutron Scattering**
Lectures of the JCNS Laboratory Course held at Forschungszentrum Jülich and the research reactor FRM II of TU Munich
edited by Th. Brückel, G. Heger, D. Richter, G. Roth and R. Zorn (2011), ca 350 pages
ISBN: 978-3-89336-725-2

28. **Neutron Scattering**
Experiment Manuals of the JCNS Laborator Course held at Forschungszentrum Jülich and the research reactorFRM II of TU Munich
edited by Th. Brückel, G. Heger, D. Richter, G. Roth and R. Zorn (2011), ca. 180 pages
ISBN: 978-3-89336-726-9

29. **Silicon nanowire transistor arrays for biomolecular detection**
by X.T.Vu (2011), vii, 174 pages
ISBN: 978-3-89336-739-9

30. **Interactions between parallel carbon nanotube quantum dots**
by K. Goß (2011), viii, 139 pages
ISBN: 978-3-89336-740-5

31. **Effect of spin-orbit scattering on transport properties of low-dimensional dilute alloys**
by S. Heers (2011), viii, 216 pages
ISBN: 978-3-89336-747-4

32. **Charged colloids and proteins: Structure, diffusion, and rheology**
by M. Heinen (2011), xii, 186 pages
ISBN: 978-3-89336-751-1

33. **Scattering Methods for Condensed Matter Research: Towards Novel Applications at Future Sources**
Lecture Notes of the 43rd IFF Spring School 2012
March 5 – 16, 2012 Jülich, Germany
edited by M. Angst, T. Brückel, D. Richter, R. Zorn ca. 1000 pages
ISBN: 978-3-89336-759-7

34. **Single-Site Green Function of the Dirac Equation for Full-Potential Electron Scattering**
by P. Kordt (2012), 138 pages
ISBN: 978-3-89336-760-3

35. **Time Resolved Single Molecule Fluorescence Spectroscopy on Surface Tethered and Freely Diffusing Proteins**
by D. Atta (2012), iv, 126 pages
ISBN: 978-3-89336-763-4

Schlüsseltechnologien / Key Technologies
Band / Volume 37
ISBN 978-3-89336-779-5

JÜLICH
FORSCHUNGSZENTRUM